2016

# Intracontinental Neotectonics: Case Studies from the Tian Shan Orogen and Kuqa Fold-Thrust Belt

Cindy M. Colón
*Louisiana State University and Agricultural and Mechanical College*

# INTRACONTINENTAL NEOTECTONICS: CASE STUDIES FROM THE TIAN SHAN OROGEN AND KUQA FOLD-THRUST BELT

A Dissertation

Submitted to the Graduate Faculty of the
Louisiana State University and
Agricultural and Mechanical College
in partial fulfillment of the
requirements for the degree of
Doctor of Philosophy

in

The Department of Geology and Geophysics

by
Cindy M. Colón
B.S., Rutgers University, 2011
May 2016

*To my family*

# ACKNOWLEDGEMENTS

I wish to thank foremost my advisor, Dr. Alexander G. Webb for his continual instruction, encouragement, and always challenging me to be a better scientist. I wish to also extend my gratitude to my advisory committee: Dr. Jeffrey Hanor, Dr. Gary Byerly, Dr. Peter Clift and Dr. Cécile Lasserre. Dr. Rowena Lohman and Dr. Marie-Pierre Doin provided invaluable guidance as well.

I deeply appreciate the financial help from the Louis Stokes Alliance for Minority Participation – Bridge to Doctorate program and the GeoDE program funded by Marathon Oil. I also thank the Instutite des Sciences de la Terre (ISTerre) of the University of Joseph Fourier for their support.

Lastly, I thank my best friend and fiancé, Philip G. Bergeron for his unconditional support and endless encouragement.

# TABLE OF CONTENTS

# ABSTRACT

This dissertation focuses on the kinematic properties of intracontinental deformation during short geologic time scales. Using three case studies this work characterizes active deformation at varying spatial scales within the continental interior of Eurasia.

The far-field effect of the Cenozoic Indo-Asia collision is considered the driving force behind active deformation with the Eurasian continental interior. The active deformation across the intracontinental Tian Shan range challenges the plate tectonic model that proposes crustal deformation is concentrated along plate boundaries. This work helps to further constrain the active kinematics of intracontinental motion that is necessary to understand the dynamics of the Eurasian intracontinental system. The two standing hypothesis that explain intracontinental deformation include the (A) discrete or (B) diffuse deformation models. While the discrete model suggests deformation occurs primarily along major faults between crustal blocks, the diffuse model suggests motion is distributed throughout the continental interior.

On a smaller scale, this dissertation examines active deformation of sub-aerial salt bodies. Ephemeral subaerial salt exposure during the evolution of a salt structure can greatly impact the subsequent development and deformation of its tectonic setting. InSAR time series analysis and inspection of individual interferograms confirm that the majority of the salt bodies in western Kuqa are active, with significant InSAR observable displacements at 3 of 4 structures studied in the region.

Decoupling between surface salt motion and climatic conditions suggests that the regional tectonic regime controls surface salt displacement rates.

Lastly, on a more local scale, this work examines the characteristics of anthropogenic deformation. Unnatural, rapid rates of subsidence and/or uplift have extreme hazard potential because it may lead to infrastructure damage and increased flood potential. Surface subsidence resulting from hydrocarbon extraction has been widely observed across the globe. However, the occurrence of surface uplift caused by fluid injection has only recently been noted and is less documented. An unusual surface displacement distribution at the Dawanqi oil field in the Kuqa fold-thrust belt of northwestern China suggests that fluid extraction may not only cause widespread, irreversible subsidence but also facilitate local uplift.

# CHAPTER 1
# INTRODUCTION

## 1.1 Neotectonics

Neotectonics is a term that has been debated since its introduction by W.A. Obrutschow (cf. Murawski, 1972), who defined it as a tectonic period from early Neogene to the present time. Other workers restricted neotectonics to a specific time interval like the Pliocene and Quaternary epoch only (Bates and Johnson, 1980; Gary et al., 1972) or the Quaternary alone (Diebold and Müller, 1985). These definitions can be applied globally. However, they do not take into consideration regional variations of tectonic evolution.

A different approach was taken when a neotectonic period was defined as the time that elapsed since the last major tectonic reorganization in a region of interest (Sengör et al., 1985). Similarly, it was proposed by Hancock that the start of a neotectonic period should be defined by when the present-day configuration of relevant plate boundaries and motions were established (Hancock and Williams, 1986). T.G. Blenkinsop modified Hancock's proposal by defining the neotectonic phase as having commenced when the contemporary stress field of a region was established (in Hancock and Williams, 1986). A later refinement of the term suggested that 'a neotectonic period may be regarded as having begun when characteristic changes in the tectonic evolution have occurred (Becker 1993). However, this refinement is complicated by the introduction of 'transitional time intervals' during which there are overlaps between the previous tectonic period and the present (neotectonic) period. While defining the beginning of a neotectonic period has been debated, it is agreed that a neotectonic period includes the present tectonic regime. The

research presented herein defines the present, neotectonic characteristics of the Tian Shan and the Kuqa fold-thrust belt.

## 1.2 Intracontinental deformation

Deformation across the Tian Shan mountain range occurs as a far-field effect of the Cenozoic Indo-Asia collision; challenging the plate tectonic assumption that crustal deformation is concentrated along plate boundaries (Molnar and Tapponnier, 1975). Lateral and vertical motion within continental interiors play important roles in the development and evolution of continental geology but it is not adequately explained by plate tectonic theory. Constraining the geometries and kinematics of intracontinental motion is necessary to understand the dynamics of intracontinental deformation. This work provides new perspective by relating the established structural interpretations to our geodetically measured kinematics and deciphers between contrasting deformation models. This section (Chapter 2) will be submitted for publication.

## 1.3 Salt tectonics

The unique and controlling influence that the presence of salt has within a basin warrants the term ‘salt tectonics’ to describe geometries and deformation specifically associated with significant salt deposits. From its impact on hydrocarbon systems to its direct use for consumption and food preservation, salt has proven to be a critical resource. Salt tectonics is especially significant to the oil and gas industry because the majority of the worlds’ large hydrocarbon reserves are associated with the presence of rock salt. In addition to the direct use of salt and its implications for hydrocarbon systems, usage of salt caverns for storage has become a viable option within the last ~60 years (Thoms and Gehle, 2000). Further understanding of salt motion directly affects models used for mining

strategies and predictions about the kinematic and mechanical behavior of salt caverns. Subaerial salt bodies are also important to understand because the surface history of salt is critical for long-term structural evolution of salt-dominated tectonic systems. Direct observations of salt structures are necessary to better understand salt kinematics. Our proposed remote sensing analysis of active kinematic patterns of surface salt structures in northwestern China, Kuqa fold-thrust belt provide a unique case study for salt kinematic behavior. This section (Chapter 3) has been submitted for publication to Earth and Planetary Science Letters.

## 1.4 Anthropogenic deformation

The significant and rapid changes to the Earth's atmosphere, land, oceans, and biosphere can be traced back to the discovery and exploitation of hydrocarbons that ultimately lead to the Industrial Revolution, which is proposed to be the beginning of the Anthropocene (Zalasiewicz et al., 2011; Steffen et al., 2011). Anthropogenic deformation describes deformation that is the result of human activity or influence. Hydrocarbons were an essential component of the Industrial Revolution and continue to be one of the most important commodities of in our modern world. The accelerated use of hydrocarbons over the past two centuries has lead to significant anthropogenic disturbances to Earth's natural environment including surface deformation. The severe safety hazards potential that can result from unnaturally rapid rates of subsidence and/or uplift make anthropogenic deformation critical to understand (Fielding et al., 1998). Using a case study in the Dawanqi oil field within the Baicheng synclinal basin of the Kuqa fold-thrust belt, northwest China, this work addresses the pattern and magnitude of direct and indirect anthropogenic deformation. This section (Chapter 4) will be submitted for publication.

# CHAPTER 2
# INTRACONTINENTAL DEFORMATION CONSTRAINED BY INSAR

## 2.1 Introduction

The Tian Shan Mountain range is one of the most actively deforming intracontinental mountain belts on Earth (Daëron et al., 2007). The plate tectonic assumption that crustal deformation is concentrated along plate boundaries is challenged by the Tian Shan, where deformation occurs as a far-field affect of the Cenozoic Indo-Asia collision *(*Molnar and Tapponnier, 1975). The paradigm shift brought by plate tectonic theory allowed for many seemingly unrelated first-order observations of the Earth to be effectively explained. However, it fails to adequately elucidate occurrences of deformation within continental interiors like that observed across the Tian Shan. Lateral and vertical motion within continental interiors play important roles in the development and evolution of continental geology. Constraining the geometries and kinematics of intracontinental motion is necessary to understand the dynamics of intracontinental deformation. Our work provides new perspective by relating the established structural interpretations to our geodetically measured kinematics.

Explanation of Eurasian intracontinental deformation continues to be debated today. The principal two contrasting views regard either (A) discrete or (B) diffuse deformation as the controlling deformation mechanism across the continental interior. The discrete deformation model proposes that major faults primarily accommodate motion between crustal blocks, whereas the diffuse model suggests motion across the continental interior is more distributed (e.g., Peltzer and Tapponnier, 1988; Wright et al., 2004).

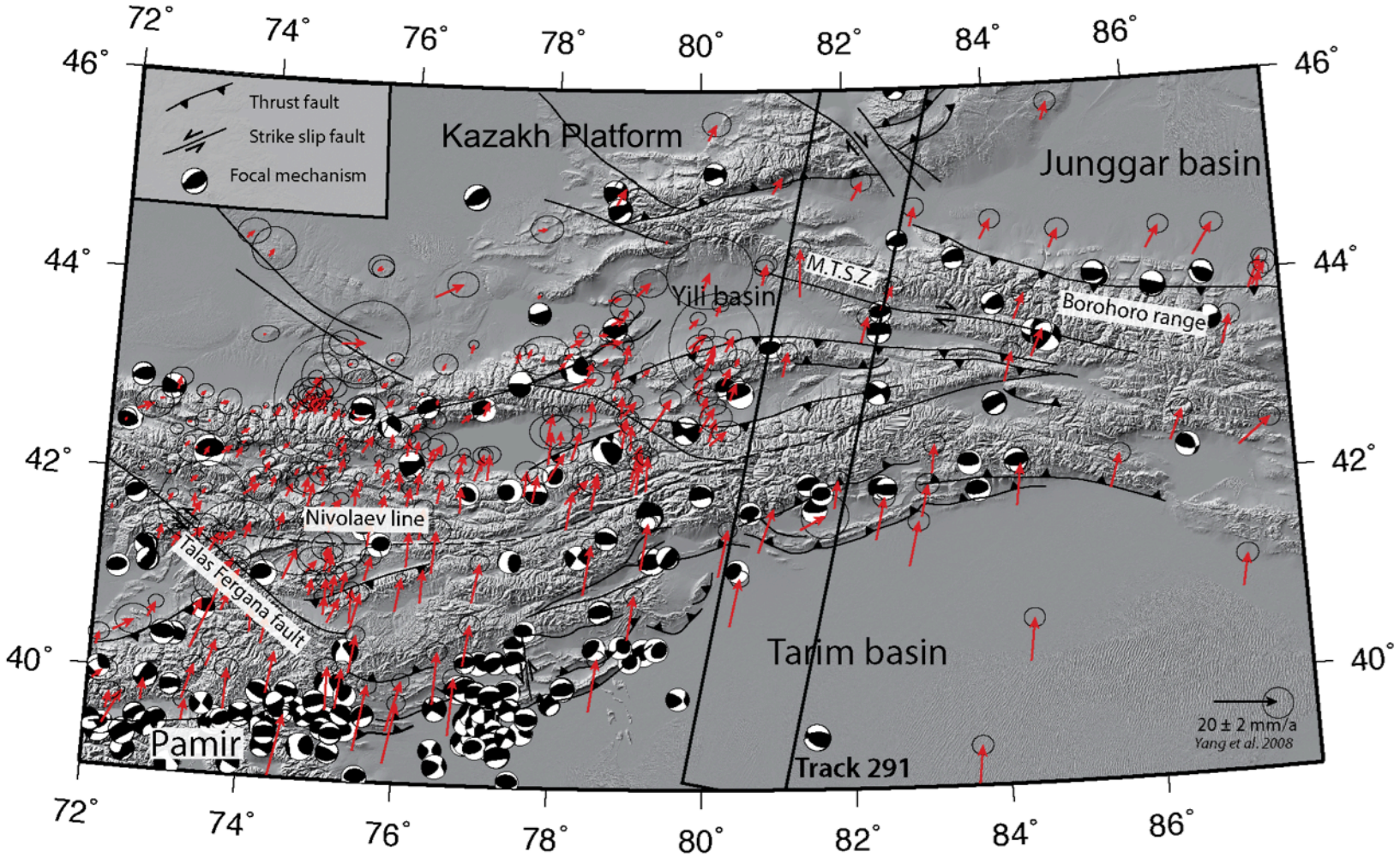


Figure 2.1 Regional topographic (SRTM DEM) and tectonic map across the Tian Shan. Major tectonic structures are drawn from Jolivet et al., 2010. M.T.S.Z. = Main Tian Shan Shear Zone. Red arrows designate GPS velocity vectors across the region from Yang et al., 2008. The area encompassed by the elongated, black rectangle corresponds to the spatial coverage of Envisat Track 291.

Neotectonic surface vectors across the Tian Shan is toward the north- northeast (Yang et al., 2008; Jolivet et al., 2010). Geodetic studies of the Tian Shan using a global-positioning system (GPS) have constrained the lateral velocity field across the region (Figure 2.1) (Zubovick et al., 2010; Yang et al., 2008). From this work I have learned that the Tian Shan actively accommodates convergence between the Tarim Basin and Kazakh Platform, with localized zones of shortening at rates of ~2 mm/yr to 6 mm/yr (Zubovick et al., 2010). The velocity field indicates that the Tarim Basin is thrusting beneath the Tian Shan at ~4-7 mm/yr (Zubovick et al., 2010). The majority, approximately 80–90%, of the North-South shortening measured with GPS is absorbed along the southern and northern edges with apparently little deformation accommodated within the interior supporting the discrete deformation model (Yang et al., 2008). However, more spatially dense sampling of active displacement would be necessary to rule out the diffuse deformation model.

While GPS observations provide critical information about the lateral orientation and magnitude of crustal deformation, it is not a complete picture. The pattern of vertical motion is also necessary to assess because it can shed light on how intra-continental deformation is distributed north of the Tarim basin within the mountain range. Discrete deformation is likely to be accommodated by localized vertical surface motion along major fault zones. Whereas diffuse deformation is more likely to result in vertical motion that is distributed across the region along small fault systems. By determining the distribution of vertical motion across the region, I can better interpret whether the intracontinental deformation here is discrete or diffuse. Therefore our approach to decipher which deformation model is most applicable involves using a technique that measures vertical surface motion, interferometry of synthetic aperture radar (InSAR). InSAR is a satellite

remote sensing technique able to circumvent the limitations of sparse spatial sampling across rugged terrains, as experienced by GPS surveys. With InSAR I are able to produce maps of surface displacements with spatial resolutions that reach tens of meters, detect motion on the range of millimeters and cover large regions of up to hundreds of squared kilometers.

## 2.2 Background

### 2.2.1 Geologic setting

The Tian Shan mountain range occupies parts of western China, Kazakhstan and Kyrgyzstan with peaks reaching 7,400 m in height (Figure 2.1). The Kuqa basin and fold-thrust belt in between the Tarim Basin and Tian Shan was likely part of the Paleozoic north Tarim continental margin (Jia et al., 1998). The Borohoro Range separates the Yili Basin from the north Tian Shan piedmont and the Junggar Basin. During the Late Paleozoic, the northern boundary of the Yili basin was an active continental margin related to the southward subduction of the north Tian Shan oceanic basin (Allen et al., 1991). The Yili basin is located in between the Main Tian Shan Shear Zone (MTSZ) to the north and a south-dipping thrust fault to the south. Further north, Dzungarian Basin and Dzungarian Alatau are separated by a north-dipping thrust fault with a major right lateral strike slip fault toward the east (Allen et al., 1994).

During the Paleozoic, the northern passive margin of the Tarim block collided with a north-dipping ocean-continent subduction zone (i.e., Windley et al., 1990). The subsequent continent-continent collision to the north of the Tarim block produced the southern part of the Tian Shan (i.e., Windley et al., 1990). A suture that separates a Carboniferous island arc from an active continental margin developed over a south-dipping

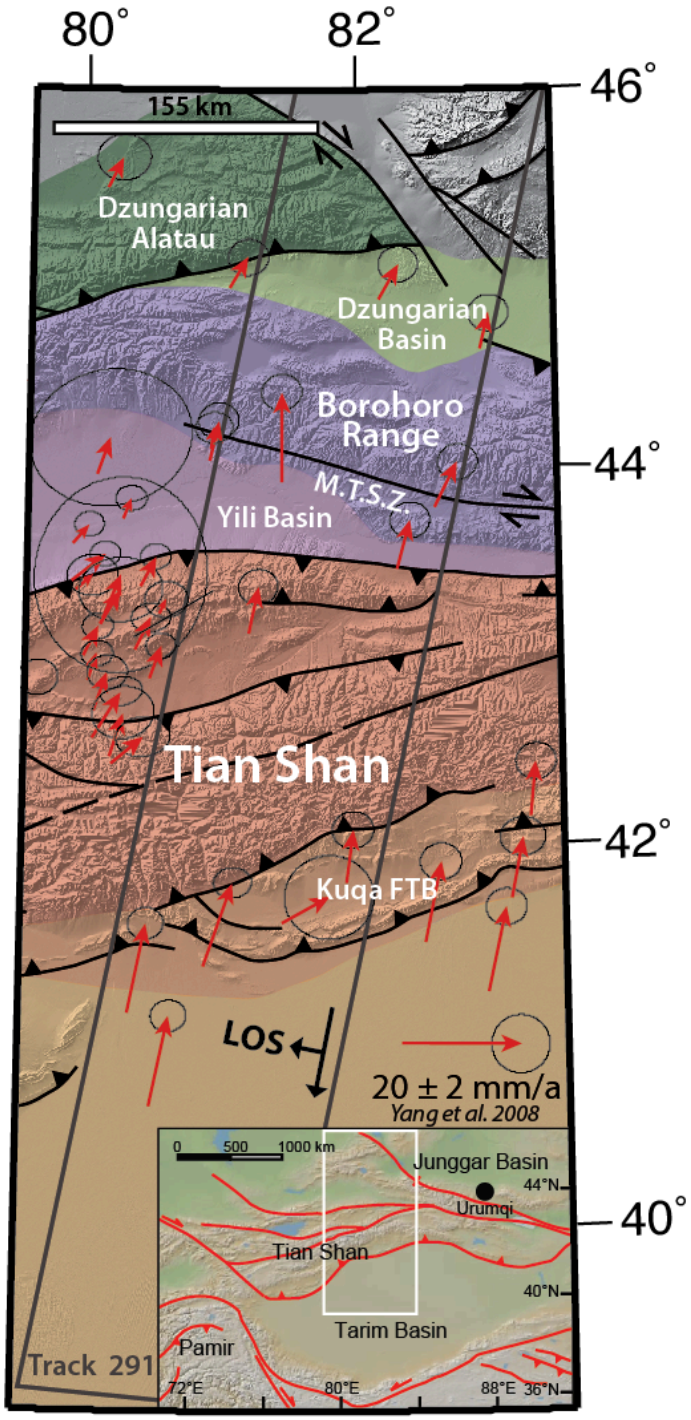


Figure 2.2 General topographic (SRTM DEM: Shuttle Radar Topography Mission digital elevation model) and tectonic map across the eastern portion of the Tian Shan range. Major tectonic structures are drawn from Jolivet et al., 2010. M.T.S.Z. represents the Main Tian Shan Shear Zone. Varying colors separates the general tectonic regions. Red arrows designate GPS velocity vectors across the region from Yang et al., 2008.

subduction zone characterizes the northern Tian Shan (i.e., Windley et al., 1990). Mesozoic deformation north and south of the Tarim block in the Tian Shan and Kunlun Shan, respectively, resulted from collision between island arcs with Asia's southern margin (i.e., Allen et al., 1994). Cenozoic deformation across the Tian Shan is the result of far-field compressional stress from the collision between the Indo-Australian and Eurasian plates (Molnar and Tapponnier, 1975). Up to 200 km of cumulative shortening has been accommodated across the Tian Shan during the Cenozoic (e.g., Avouac et al., 1993).

### 2.2.2 Intracontinental deformation models

For decades, Eurasian intracontinental deformation models have focused on the explanation of the Tibetan Plateau uplift and the accretion of continental lithosphere (e.g., Tapponnier and Molnar, 1976; Tapponnier et al., 1982). Today, two houses of thought remains; one that proposes a discrete form of deformation via movement between continental blocks and another that proposes diffuse deformation by way of continuous mechanics (e.g., Peltzer and Tapponnier, 1988; Thatcher, 2007; Meade, 2007). Eurasian intracontinental formation studies often focus on Tibet and neglect the Tian Shan range. However, I use these models to interpret deformation observed across the Tian Shan because its Cenozoic growth is a far field effect of the India-Asia collision that is also responsible for the growth of the Tibetan Plateau.

Discrete intracontinental deformation is described by motion between crustal blocks and elastic strain accumulation. The pervasiveness of strain softening during experimental deformation suggests that the geometry of large faults that rapidly propagate with increasing strain may control the continental deformation (Peltzer and Tapponnier, 1988). Faulting sequences during an analog study were compared to collision-induced strike-slip

faulting in Asia and the distinct phases of strike-slip extrusion was interpreted to have resulted from strain localization representing the temporally discontinuous, non-steady-state deformation of the continental lithosphere (Peltzer and Tapponnier, 1988). Alternatively, numerical experiments testing a thin viscous sheet model are interpreted to show diffuse crustal thickening is the principal mechanism of accommodation of continental convergence (England and Houseman, 1986). The experiments of England and Houseman, (1986) consisted of a simple indenting boundary condition applied to initially laterally homogeneous sheets obeying a power law rheology and found the formation of a plateau by crustal thickening in front of the indenter primarily accommodated convergence (England and Houseman, 1986). Unlike discrete deformation models, England and Houseman, (1986) regard strike slip deformation as a relatively recent result of this thickening and not as a dominant mode of accommodation of convergence throughout the Tertiary.

Global positioning system measurements across Asia have facilitated neotectonic modeling and have been used to support both deformation models. (e.g., Zhang et al., 2004; Thatcher, 2007). Meade, 2007 proposed that elastic strain accumulation across rigid crustal blocks that cause velocity gradients to be smooth, rather than stepped as is expected over geologic time scales, are due to interseismic locking of the fault zone. Assuming that GPS velocity fields represent crustal deformation over geologically short temporal (100-1000 years) scales, the relatively low geodetically measured fault slip rates are interpreted to represent rigid block discrete deformation (Thatcher, 2007; Meade, 2007). However, the same geodetic datasets have been used to support continuous or diffuse deformation models (e.g., Wang et al., 2001; Zhang et al., 2004; Yin and Taylor, 2011).

Varying rigid block configurations that fit GPS observations will verify that block boundaries are non-unique (McKenzie and Jackson, 1986; Flesch and Bendick, 2007). Additionally, the scale of rigid blocks in a discrete approximation of a diffuse (continuous) velocity field, not exact block geometry, determines the goodness of fit (Flesch and Bendick, 2007). Flesch and Bendick, 2007 comment that the same observations made by Meade, 2007 and Thatcher, 2007 may alternatively infer deformation of a highly viscous material can best explain Tibetan kinematics at large length scales. If the bulk mean rheology of Tibetan lithosphere behaves viscously then Tibet may represent a body with a continuously varying strain function that may or may not have lateral strength variations (Flesch and Bendick, 2007). Furthermore, general shear flow and distributed deformation is used to explain the formation of a late Cenozoic V-shaped conjugate strike-slip fault system in central Tibet (Yin and Taylor, 2007). This interpretation is based on the correlation between GPS observations and fault patterns (two east-trending shear zones) that suggests the central Tibet conjugate faults initiated as two sets of Riedel shears in the parallel but separate shear zones by gravitational spreading of Tibetan lithosphere or horizontal shear at the mantle lithosphere (Yin and Taylor, 2007).

## 2.3 Methods

### 2.3.1 Overview of satellite remote sensing

Active satellite remote sensing systems, like synthetic aperture radar (SAR), illuminate the ground surface with energy and record the backscatter. SAR systems, like the Envisat ASAR used for this work, utilize microwaves that are able to penetrate clouds and allow day and night operation. SAR systems are able to acquire relatively high-resolution imagery with relatively small radar antennas by using the motion of the radar

along a flight path to form a 'synthetic antenna' that is larger than its real aperture. The synthetic aperture improved resolution in the azimuth direction (parallel to satellite track) but not in range direction (across track). Higher resolution in the range direction is achieved by the use of a frequency modulated waveform and pulse compression to simulate very short pulses producing high-resolution echoes. The radar images from SAR systems are complex images because each pixel contains two pieces of information about the ground reflectors: wave phase and magnitude of the backscatter. Interferometric SAR (InSAR) measures the difference in phase, pixel by pixel, between two radar images acquired at different times to infer ground surface motion with millimeter precision. This precision is obtained only when using time series analysis of multiple interferograms.

This work utilized data from the European Space Agency's Envisat satellite. Envisat was launched in 2002 and was the largest Earth Observation spacecraft ever built at that time (Ferretti, 2007). Envisat has a sun-synchronous circular orbit (98.55°) at a mean altitude of 800 km altitude, with a 35-day repeat cycle (ESA, 2016). The Envisat payload included optical (MERIS spectrometer) and radar instruments to provide continuous observation and monitoring of the Earth's land, atmosphere, oceans and ice caps (Ferretti, 2007). The largest instrument aboard Envisat is the Advanced Synthetic Aperture Radar (ASAR), operating at C-band frequency. Contact was officially lost with Envisat in May 2012 (ESA, 2016).

### 2.3.2 Initial InSAR processing methods

The European Space Agency (ESA) Envisat Advanced Synthetic Aperture Radar (ASAR) C-band radar images of northwest China that were processed and analyzed were acquired between September 2003 and October 2010. Our initial InSAR processing utilized

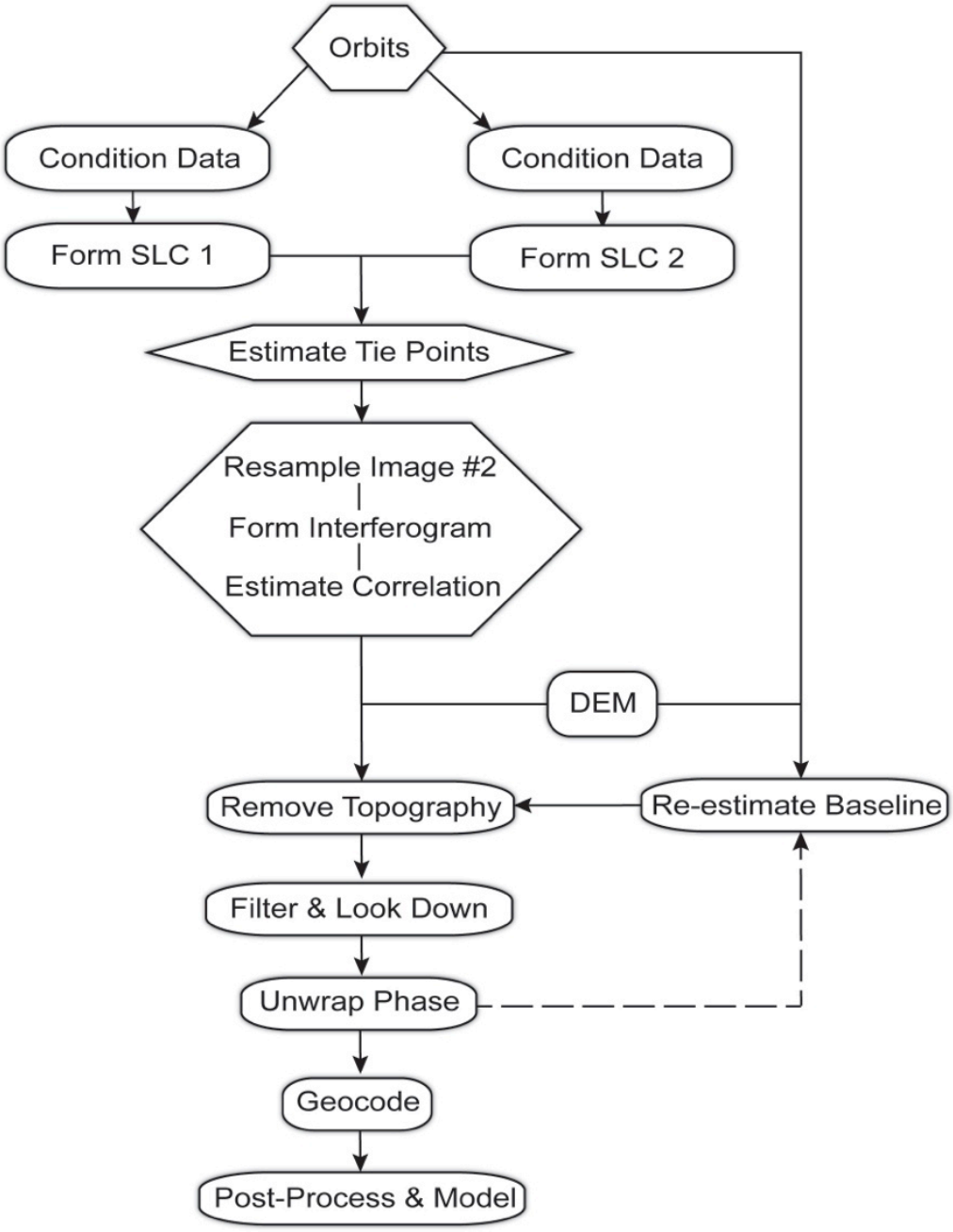


Figure 2.3 Generalized InSAR processing workflow of the Caltech/JPL ROI_PAC software. Modified from Fielding, 2012.

a subset of images along the descending Track 291. Many combinations of Envisat image pairs were used to produce approximately 130 individual interferograms with the Caltech/JPL Repeat Orbit Interferometry Package (ROI_PAC) software (Rosen et al.,

2004). Perl scripts control the processing stream implemented by the ROI_PAC software with a few algorithmic functions carried out by Fortran or C programs (Buckley 2000). The ROI_PAC processing sequence is an iterative process that is roughly outlined by the workflow in Figure 2.3. Buckley, 2000 describes the detailed procedure of ROI_PAC's processing chain.

Interferometric processing of synthetic aperture radar (InSAR) began with data conditioning, where the data was converted from the ESA format to a raw version that could be read by ROI_PAC. Pairs (one reference image and one slave image) of raw radar images were chosen to generate interferograms; these images were used more than once. The first step was to generate the SAR images for the reference and slave image followed by image coregistration. Each complex pixel of the reference image was multiplied by the complex conjugate of each slave pixel to form the initial interferogram. At this point the interferogram had all phase components included, such as orbit geometry, topography, deformation, and atmosphere (Fielding, 2012).

The following steps in the processing chain were used to modify and improve the initial interferogram. Flattening of the interferogram corrected for the Earth's ellipsoid. This was followed by the calculation of the spatial correlation of the phase as an estimate of the interferometric coherence. Coherence is an indicator of how much the backscatter has changed between the reference and the slave image (Fielding, 2012). Then the interferogram was corrected for topography. This was done by creating a simulation from the SRTM Global 90m DEM and the orbit of the master scene and calculating the topographic phase then subtracting it from the original interferogram (Fielding, 2012). The statistical-cost, network-flow algorithm for phase unwrapping (SNAPHU) was applied to

the filtered and masked interferogram. The baseline was re-estimated using the unwrapped phase and the topography in the radar coordinates and then it was re-applied (Hooper et al., 2004). Geocoding was the final step in the interferogram generation. This entire process was applied for each interferogram individually before they were all stacked to perform a time series calculation.

Post-processing was applied to all interferograms using Barnhart's InSAR Time Series for Matlab (ITS) package (Barnhart and Lohman, 2012). Approximately 77 interferograms of the 130 produced were selected based on spatial coherence and used for the time series stack. Pixels with a coherence of less than .75 were not used in the stack. This package coregistered the unwrapped interferograms in the radar coordinates to a single master then removed a ramp from all of the interferograms to account for satellite orbital errors. Lastly, the time displacement history was inverted, pixel-by-pixel, and a linear rate map was generated in radar coordinates. This standard processing technique was not adequate for our research interests because data coherence was lost in the mountainous areas of the Tian Shan. Because of this I decided to reprocess the data applying a new technique called a small baseline approach that showed it could better maintain phase coherence across steep topography.

### 2.3.3 Small baseline InSAR processing approach

Interferometry of synthetic aperture radar (InSAR) is a powerful remote sensing tool that allows the detection of surface motion across spatially extensive areas with millimeter to centimeter precision (e.g., Zebker et al., 1994; Massonnet and Feigl, 1998; Barnhart and Lohman, 2012). The European Space Agency (ESA) Envisat Advanced Synthetic Aperture Radar (ASAR) C-band radar images I processed and analyzed were

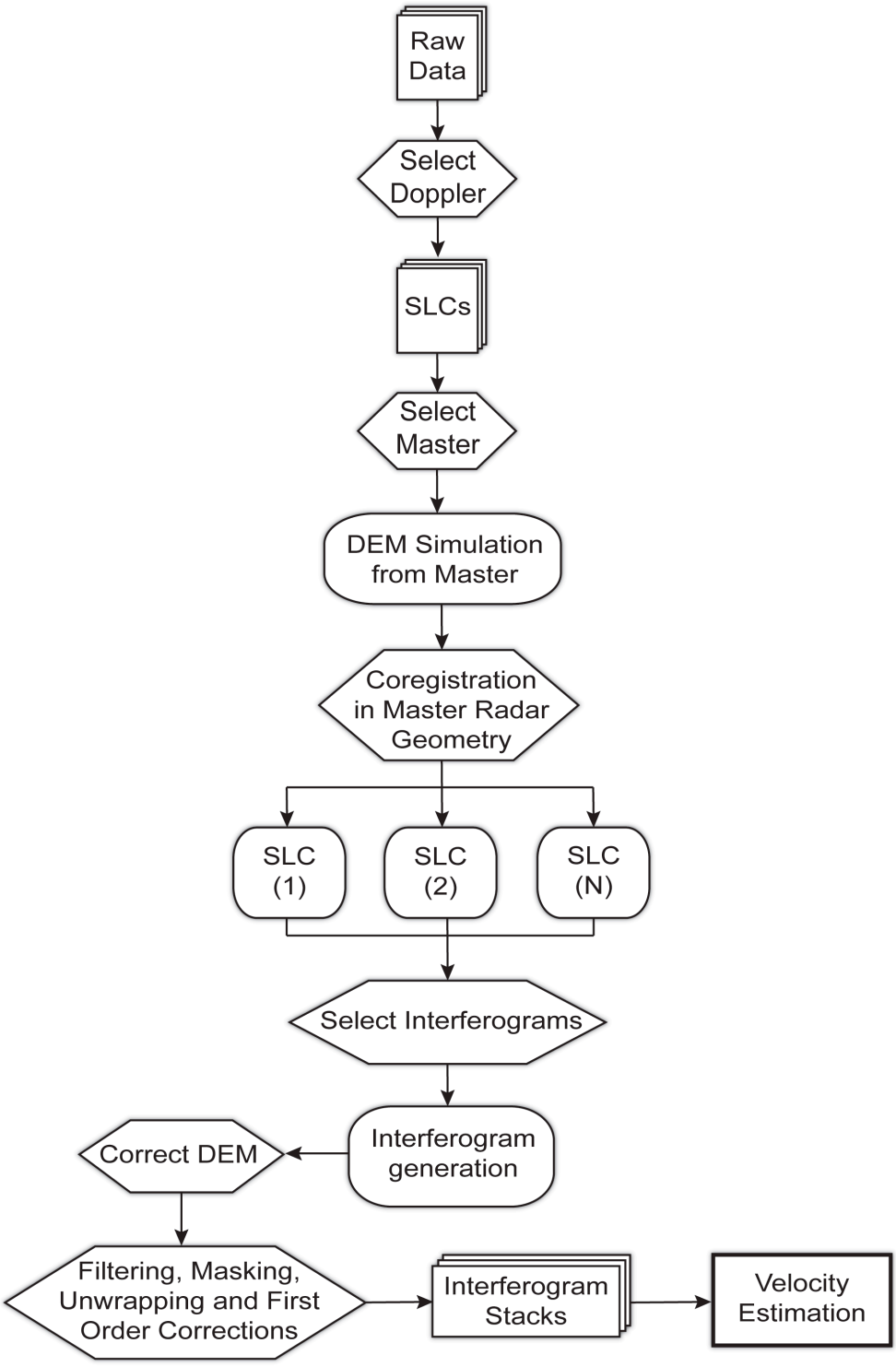


Figure 2.4 Block diagram to illustrate the InSAR processing workflow utilized by the NSBAS (New Small Baseline Algorithm Subset. Adapted from Guillaso et al., 2011.

acquired between June 2003 and October 2010. The radar tracks used for this analysis were 800-1000 km long; the 37 images from Track 291 cross the Tian Shan and cover the northern region of the Tarim Basin. Multiple SAR images are used to generate sets of interferograms to infer time-variable displacements (e.g., Berardino et al., 2002). Interferometric processing was completed using the New Small Baseline Algorithm Subset (NSBAS) chain as described by Doin et al., 2009.

To begin the interferometric processing of synthetic aperture radar (InSAR), the raw data was converted form the Envisat format into a format that could be read by ROI_PAC. SLCs (Single Look Complex images) were then generated in a common Doppler centroid geometry (Doin et al., 2011). Unlike the ROI_PAC processing chain (Chapter 2), NSBAS registers all of the radar images to one super master image before interferograms are generated. Image 20050418 was the master image for Track 291 to which every other radar image would be co-registered. The selection of a small baseline network of interferograms was automatized by NSBAS and it depended on interferogram redundancy and specified constraints for perpendicular (Bp) and temporal baseline (Bt) (Doin et al., 2011). The interferograms generated were constrained to the following parameters: Bp <500 m and Bt <1.5 years; B <300 m and Bt <3 years; Bp <50 m and Bt <5 years. The initial differential interferograms were generated once the network of interferograms was selected.

The second part of the interferometric processing involved applying corrections before filtering, unwrapping, and time series analysis. In an area of high topographic relief, such as the Tian Shan, it was important to apply stratified atmospheric and DEM error corrections prior to filtering and unwrapping (Doin et al., 2011). Doin et al., (2009)

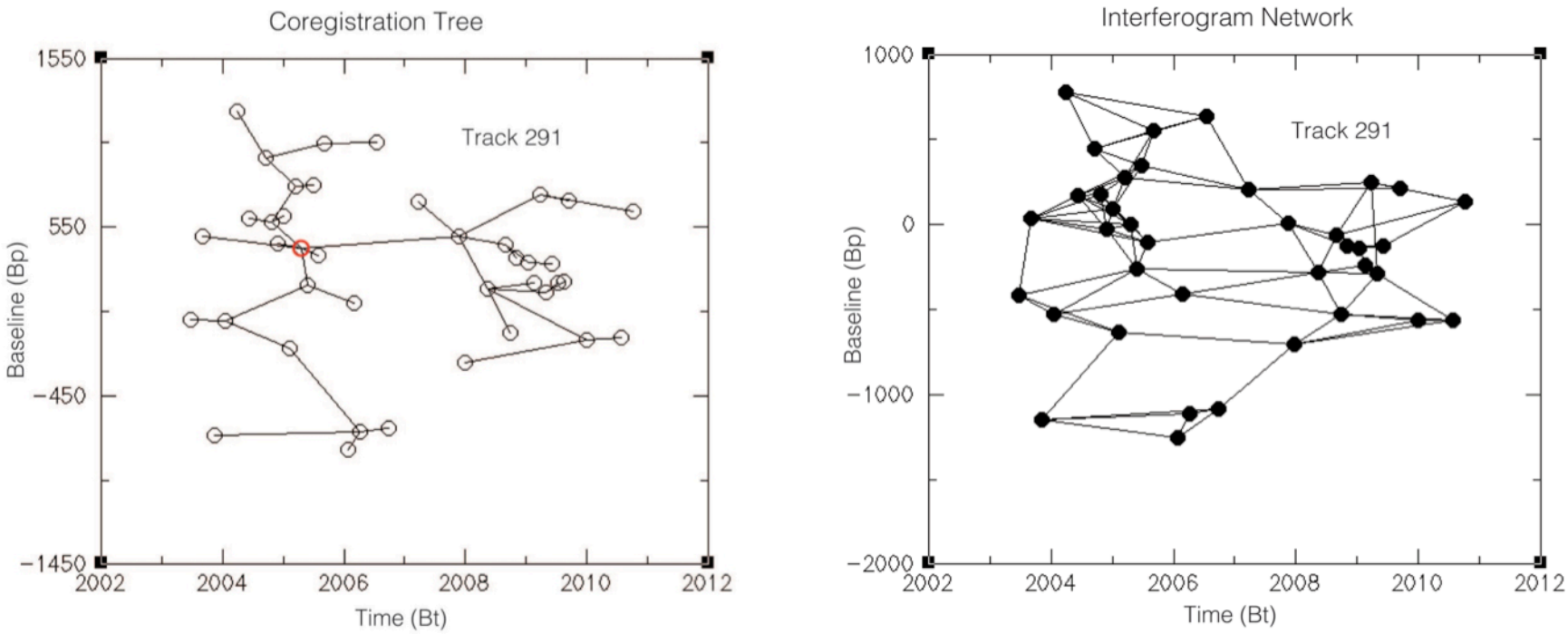


Figure 2.5 Coregistration tree for Track 291, each image must be coregistered to the same geometry before interferograms can be generated. Each circle represents an image acquisition from Track 291 plotted as a function of perpendicular baseline relative to the first image versus time. The red circle highlights the master image to which all SAR acquisitions were coregistered to; there were several sub-masters used in the coregistration process. (Right) The network of interferograms generated for Track 291 and used in the time series analysis. Each dot represents an image acquisition plotted as a function of perpendicular baseline relative to the master image versus time. Each line represents an interferogram that was generated between the 2 dates that the line connects.

describe the details of the atmospheric correction applied. The DEM correction procedure used in NSBAS is described by Ducret et al., (2014). Both steps showed their importance in a previous interseismic study across Himalaya (Grandin et al., 2012). The unwrapping algorithm used varies moderately from the branch-cut algorithm employed by ROI_PAC. The unwrapper used is better suited for areas of low coherence, like the Tian Shan, because multiple iterations of phase unwrapping occur as the coherence threshold decreases (Doin et al., 2011, Grandin et al., 2012). Filtering and unramping were reapplied after phase unwrapping as well to correct for residual orbital errors. In the final step, the phase delays of unwrapped interferograms were inverted pixel by pixel for the total phase delay of each date relative to the first date (whose delay was set to zero) (Doin et al., 2011; Jolivet et al., 2011).

The average displacement rate maps are displayed in the satellite line of sight (LOS) with positive and negative values corresponding to movement toward and away from the sensor. The look angle and direction of the Envisat ASAR images allow our calculated dataset to be predominantly sensitive to vertical motion therefore I interpret positive and negative measurements to indicate uplift and subsidence, respectively.

**2.4 Results**

Our InSAR track extends over 800 km from northern Tarim Basin to Dzungarian Alatau across eastern Tian Shan. Gaps in the data represent areas along the track where coherence was poor. Across the track, isolated and abrupt patches of reds and blues are characteristic of phase unwrapping errors. These errors occur where the phase signal incorrectly jumps a phase cycle with respect to surrounding pixels causing an abrupt phase change. Although the InSAR results are presented in the satellite's line of sight, the dataset

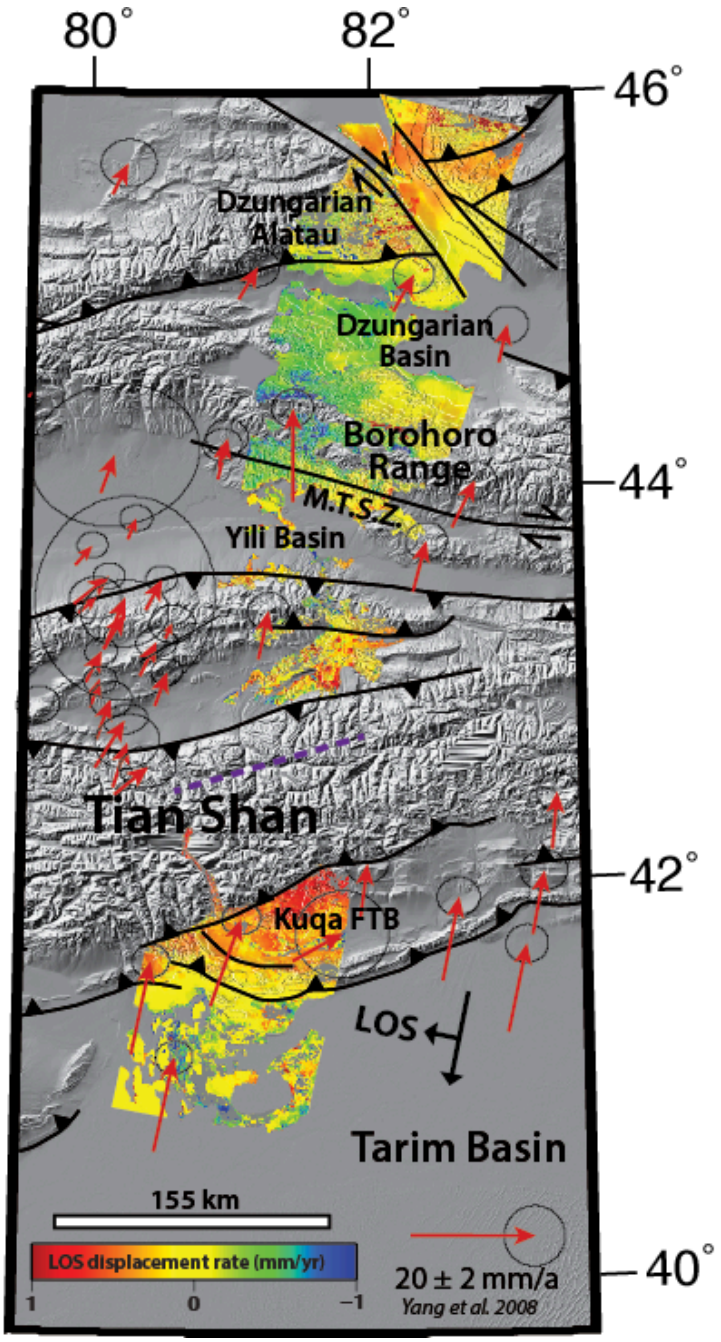


Figure 2.6 Linear average InSAR velocity map overlays the topographic map. The InSAR results using descending Envisat imagery from 2003 to 2010 and displayed in the satellite's line of sight (LOS). The displacement rate results are saturated to the color scale from -1 to 1 mm/yr. Warm (red) and cool (blue) colors correspond to motion toward and away from the satellite, respectively. The purple dashed line represents a division in the data; north of the purple dashed line the data was processed with respect to a northern reference area and south of the purple dashed line the track was processed with a southern reference area. This was done to optimize coherence across the study area.

is predominately sensitive to vertical motion therefore I consider positive and negative motion to represent uplift and subsidence, respectively. However, care must be used when interpreting motion across strike slip faults. Given the satellite descending flight direction (north to south) and the view direction (west-northwest), measured surface displacement along a right lateral strike-slip fault will results in positive measurement (toward the satellite).

The rapidly changing surfaces of the sand dunes in northern Tarim Basin are most likely the cause for the unwrapping errors and areas of coherence loss in that region. However, the overall signal suggests vertical motion is minimal at northern Tarim Basin just south of the Kuqa fold-thrust belt. Across the Kuqa fold-thrust belt I detect motion toward the satellite in the LOS direction between 0.5 to 1 mm/yr. Positive motion at the Kuqa fold-thrust belt is concentrated immediately south of the Tian Shan frontal fault.

Like northern Tarim Basin, the central portion of our track is plagued by low coherence and unwrapping errors. For much of the Tian Shan region covered by Track 291, there is no evidence for vertical motion exists on the temporal scale of my observation. Across the Borohoro Range motion away from the satellite increase from east to west, approaching -0.9 mm/yr. The Dzungarian Basin is dominated by motion away from the satellite approaching 0.5 mm/yr. The InSAR data across the eastern edge of the Dzungarian Alatau is very noisy, however, the background signal predominately shows no significant surface displacement. Dzungarian Alatau is bounded on the east by a major right lateral strike-slip fault; across from which positive LOS displacement rates are measured.

## 2.5 Discussion

This chapter has presented here the first InSAR analysis done across the Tian Shan range and bordering regions. The debate over the type of mechanism that controls Eurasian intracontinental deformation has predominantly focused on the Tibetan Plateau. This work takes a look further into the Eurasian continental interior beyond the scope of the existing studies and uncovers new information about deformation within the continental interior. InSAR analysis of Eurasian intracontinental deformation supplements existing geodetic studies.

Strong uplift concentrated south of the Tian Shan frontal thrust at the Kuqa fold-thrust belt, between 0.5 to 1 mm/yr, suggests that as the Tarim crustal block moves further north, all of the vertical motion is taken up by the Kuqa fold-thrust belt. The Tian Shan does not appear to be uplifted despite the expected crustal thickening resulting from the subduction of the Tarim block below the Tian Shan. Claims that the Tian Shan absorbs the deformation as the Tarim basin moves northward is challenged by our results because instead I see that the northern most part of the Tarim Basin, the Kuqa fold-thrust belt is deforming a rate much greater than the Tian Shan, where I observe no signal of vertical motion. The uplift across the Kuqa fold-thrust belt suggests that the Tian Shan is propagating toward the south. The area of uplift at Kuqa fold-thrust belt covers an area about 62 km long and about 94 km wide south of the Tian Shan frontal thrust fault. The discrete deformation model, that predicts localized deformation along a major fault, does not coincide with the large area over which the uplift occurs. Instead, the widespread uplift in Kuqa fold-thrust belt supports the distributed deformation model that accommodates displacements across a number of smaller faults.

InSAR coverage between the southern Tian Shan and the Main Tian Shan Shear Zone (M.T.S.Z.) is poor, making definitive interpretation impossible. Further north, there is some indication of subsidence across the Borohoro Range and into the western part of the Dzungarian Basin, approaching -0.9 and -0.5 mm/yr respectively. GPS vectors suggest northwestern compression between Dzungarian Alatau and Dzungarian Basin. Subsidence across the Dzungarian Basin is likely due to continual flexural loading of the basin as the Dzungarian Alatau thrusts onto the Dzungarian Basin.

The large right lateral strike slip fault bounding Dzungarian Alatau is interpreted to be actively accommodating strain despite a lack of earthquakes in the vicinity. InSAR detects the vertical component of motion but because of the roughly perpendicular orientation of the satellite line-of-sight to the strike slip fault, some of the motion recorded can be explained by horizontal strike slip motion as the crust north of the fault moves toward the satellite. North of the strike slip fault, surface displacements approach 0.5 mm/yr over a widespread area, not localized and confined to the fault. The widespread area of surface displacements may appear to suggest that diffuse deformation is in place. However, this type of signal is expected during interseismic periods, when the shallow parts of the fault are locked, across a strike-slip fault.

## 2.6 Conclusions

This work represents the first InSAR analysis to characterize the kinematic distribution of vertical displacements across from the Tian Shan range to the Dzungarian Alatau range. The results are interpreted through the lens of neotectonic, intracontinental studies of the Tibetan Plateau. The widespread area over which the Kuqa fold-thrust belt absorbs compression suggests a distributed form of deformation is predominant in the area.

Similarly, the widespread area of surface displacements north of the large strike slip fault, bounding Dzungarian Alatau, to the north suggests that the diffuse deformation model more adequately describes the deformation pattern here. The lack of coherence between the Tian Shan and the Borohoro Range limit more thorough interpretations as to the overall dominant deformation style. My observations span a brief portion of the interseismic cycle, which typically occurs on a scale of 10-100 years. While it is possible that the kinematics observed on shorter time-scales, as I do here, reflect the long-term kinematics the opposite must also be considered. Broad areas of deformations can occur during interseismic periods when the shallower portions of active faults are locked. Improved temporal coverage and continued advances in InSAR processing promise it is only a matter of time before these details become clearer.

# CHAPTER 3
# THE VARIETY OF SUBAERIAL ACTIVE SALT DEFORMATION IN THE KUQA FOLD-THRUST BELT (CHINA) CONSTRAINED BY INSAR

## 3.1 Introduction

Analysis of subaerial salt behavior is limited because allochthonous salt outcrops are rarely preserved on the Earth's surface, making subsurface imaging the primary technique for observing salt deposits (Talbot and Pohjola, 2009). Only a few examples of salt bodies outcrop at the surface today, not including submarine salt exposures. Interpretations of many subsurface salt bodies throughout the world have indicated subaerial exposure during structural evolution (e.g., Canerot et al., 2005; Callot et al., 2012). Understanding how subaerial salt bodies behave is important because the surface history of salt is remarkably critical for long-term structural evolution of salt-dominated tectonic systems, some being commonly associated with commercial oil and gas reservoirs. The distinctive mechanical properties of salt also make it one of the few solid Earth materials able to flow at the surface. Furthermore, surface salt structures are Earth-surface deformation systems that can be highly responsive to climatic.

Much of our current understanding of surface salt kinematics stems from namakier (extrusive salt "glaciers", also called "salt fountains") studies predominantly in the Alborz and Zagros Mountains in northern and southern Iran, respectively (e.g., Kent, 1979). Over one hundred Hormuz salt diapirs, fed from pipe-like conduits (point-sourced), are known to exist in the Zagros Mountains (Kent, 1979). Of these salt bodies, surface motion has been observed on twenty diapirs using a satellite-based remote sensing technique called interferometry of synthetic aperture radar (InSAR) capable of measuring millimeter-scale vertical displacements (Barnhart and Lohman, 2012). The sheet-like Garmsar salt nappe of

the Alborz Mountains extruded along a frontal thrust before undergoing open-toed advance and is presently inactive; the motion detected by InSAR is attributed to wasting (Baikpour et al., 2010). Furthermore, InSAR has also been used to detect continuous vertical, upward flow rates between 5.5-8.3 mm/yr across the line-sourced Sedom diapir in the Dead Sea basin (Weinberger et al., 2006).

Recently recognized namakiers in the western Kuqa fold-thrust belt in northwestern China provide a new natural laboratory to observe and constrain subaerial salt kinematics (Li et al., 2014). Four active point-sourced namakiers exist in western Kuqa fold-thrust belt (Figure 3.1). An active line-sourced diapir, the Tuzimazha salt wall, is comparable to the Sedom diapir with vertical, upward flow. The Quele namakier, exposed in western Kuqa fold-thrust belt is, to our knowledge, the only active open-toed, line-sourced subaerial salt structure extruded from a surface-breaching thrust fault on Earth's surface. Therefore, Kuqa fold-thrust belt provides an invaluable opportunity to study the behavior of a variety of subaerial salt bodies within the same geologic setting.

Existing work concludes that the presence of meteoric water and fluctuating temperatures are the principal factors enabling salt recrystallization and/or dissolution after surface extrusion (Talbot and Rogers, 1980; Urai et al., 1986; Desbois et al., 2010). In the present study, I use InSAR to measure the spatial and temporal deformation patterns of namakiers in Kuqa fold-thrust belt. I compare these observations to rainfall and temperature measurements in order to explore potential relationships between the active surface salt kinematics and local climatic conditions.

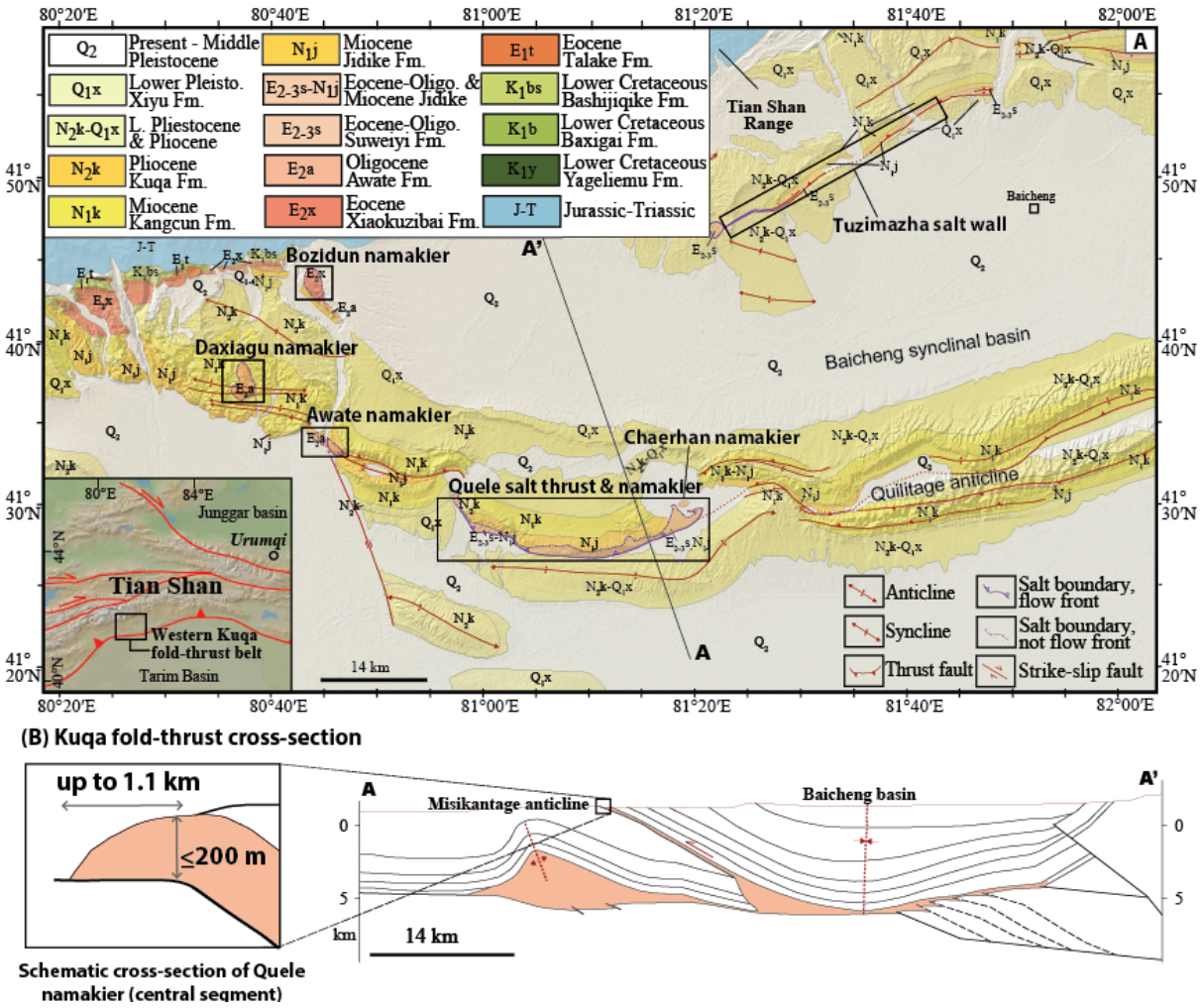


Figure 3.1 (A) Geologic map of the western Kuqa fold-thrust belt, adapted from Li et al., 2014, located south of Tian Shan Mountain Range and northern Tarim Basin. Blue and green units toward the north represent Tian Shan bedrock. Yellow and orange units represent Cenozoic basin deposits. (B) Cross section (adapted from Li et al., 2012) from the southern Tian Shan through the Kuqa fold-thrust belt, toward the Tarim basin and dissects the Quele salt nappe and the Misikantage anticline. The schematic cross section of Quele namakier is more representative of the central portion of Quele namakier.

## 3.2 Background

### 3.2.1 Geologic setting

The Kuqa foreland fold-thrust belt actively accommodates ~4-7 mm/yr of north-south tectonic shortening between the Tian Shan to the north and the Tarim basin to the south across a ~400 km long, ~20-65 km wide region (e.g., Allen et al., 1991; Zhong and

Xia, 1998; Yang et al., 2010; Zubovich et al., 2010). Contractional tectonics has formed structural hydrocarbon traps across Kuqa fold-thrust belt where the deformational style is controlled by the presence and varying thickness of salt layers (e.g. Tang et al., 2004; Chen et al., 2004; Wu et al., 2014). The subsalt sequence (Upper Permian-Cretaceous) includes Triassic-Jurassic coal and lacustrine mudstones that matured into regional hydrocarbon source rocks (Hendrix et al., 1992; Tang et al., 2004; Chen et al., 2004). Two salt dominated units control deformation across Kuqa (Li et al., 2012): the Miocene Jidike Formation and Paleocene-Eocene Kumugeliemu Group concentrated in eastern and western Kuqa, respectively. Kumugeliemu Group consists of 110-3000 m thick halite and gypsum interbedded with mudstone, sandstone, conglomerate and marl (Hendrix et al., 1992; Chen et al., 2004; Li et al., 2014). As the salt units thicken toward the south, deformation is concentrated in the suprasalt sequence. From west to east, salt décollements in Kuqa fold-thrust belt have developed into salt nappes exposed at the surface, triangle zones and pop-up structures (Chen et al., 2004; Wang et al., 2011, Li et al., 2012). The suprasalt sequence (Oligocene-Quaternary) reaches a thickness of ~7 km (Tang et al., 2004; Li et al., 2014). The salt-dominated Kumugeliemu Group in western Kuqa fold-thrust belt (Figure 3.1) outcrops at line-sourced and point-sourced salt structures. These surface salt structures display structural and stratigraphic records of active vertical motion, exhumation and surface flow (Li et al., 2014).

Point-sourced salt structures, like Awate namakier, Bozidun namakier and an unspecified structure referred to hereafter as Daxiagu namakier, are fed from an autochthonous salt body via pipe-like salt feeders called stems (e.g., Jackson and Talbot, 1986; Hudec and Jackson, 2007). Awate namakier is located at the western extent of the

Quilitage anticline system, which is divided by a south-flowing river. The portion of Awate namakier, east of the river, is approximately 2.5 km long and 1.5 km wide. The portion west of the river appears to have the same salt source (Li et al., 2014). Salt mining at the southern edge of Awate exposes freshly cut outcrop surfaces and reveals a mud-rich, 1-3 m thick carapace above the namakier. Bozidun namakier is located ~17 km north of Awate with a length of ~2.2 km and 1.4 km width. Lastly, Daxiagu namakier is the westernmost surface salt structure in Kuqa, located ~12 km west-northwest of Awate. Daxiagu is ~4.5 km long and 3.4 km wide, and I interpret it to be a point-sourced based on its circumscribed surface geometry.

Line-sourced salt structures such as Quele namakier and the Tuzimazha salt wall have relatively thin, elongated salt feeders (e.g., Jackson and Talbot, 1986; Hudec and Jackson, 2007). The Quele salt thrust propagates southward, and the salt décollement is exhumed where the thrust fault intersects the surface, forming the Quele namakier. Quele namakier is exposed across ~32 km E-W with a vertical thickness generally ranging from ~50-200 m. The namakier thins and locally pinches out toward the west and the salt thrust extends to a north-trending, salt-lubricated strike-slip fault that appears to transfer slip to another E-W trending thrust fault further north (Zhong and Xia, 1998a; Li et al., 2014). Quele namakier broadens at its eastern extent and covers an area ~5 km wide, called the Chaerhan namakier, which also features an isolated salt dome (Li et al., 2014). Large, siliciclastic rock bodies, of varying sizes reaching up to 2.5 km length, occur across Quele namakier. These rock bodies may be considered rafts if that have been dislodged from surrounding sedimentary units and incorporated into the namakier as it flows. These sedimentary bodies may also be the more brittle, siliciclastic rocks that make up the

Kumugeliemu Group. Toward the north in the hinterland of Kuqa, the subvertical Tuzimazha salt wall trends east-southeast and maintains an ~50 m thickness along its ~10 km long surface exposure.

### 3.2.2 Subaerial salt deformation and climatic impact

Relatively low viscosity and density as well as a strong resistance to compression allows rock salt to flow as a non-Newtonian fluid that can pierce through surrounding sedimentary layers in the Earth's upper crust (e.g., Weijermars et al., 1993). Microstructural analysis of salt shows that salt flow converges and accelerates as it moves from a buried source layer into a diapiric feeder or stem (Desbois et al., 2010). The principal deformation mechanisms observed at the stem of the diapir are grain-boundary migration (GBM) and sub-grain rotation (SGR) caused by increased differential stress (Desbois et al., 2010). Exhumation of salt initially forms salt domes that later develop into salt fountains as circumferential lateral spreading propagates away from the orifice (e.g., Kehle, 1988; Hudec and Jackson, 2007). Dominant deformation mechanisms shift from GBM and SGR to pressure-solution accommodated grain-boundary sliding (GBS) from the top to the distal part of the salt fountain (Desbois et al., 2010). This shift can be explained by the influx of meteoric water and the decreased differential stress as salt flow diverges radially away from the orifice (i.e., Jackson, 1985; Desbois et al., 2010). A ground-based geodetic study by Talbot and Rogers, (1980), with hourly to daily sampling, of the Kuh-e-Namak namakier in southern Iran proposed that the presence of meteoric water causes plastic deformation of the salt while daily temperature variations cause elastic deformation. Temporary surface salt flow rate of ~500 mm/day was observed at Kuh-e-Namak namakier during the annual rainy season of this semi-arid region (~330 mm average rainfall from

October to February) (Talbot and Rogers, 1980). Furthermore, it was observed that during dry periods the surface salt shrunk, retreating and losing some of lateral extent attained during the wet period (Talbot and Rogers, 1980).

Given the typical low-pressure stress conditions of subaerial salt bodies, the namakier porosity is generated by joints formed as a result of diurnal/seasonal thermal expansion and contraction (Merriam et al., 1962; Talbot and Aftabi, 2004; Desbois et al., 2010). Vertical joints in subaerial salt bodies dilate as the salt carapace spreads in response to continual growth of the viscous salt fountain, which permits infiltration of meteoric water (Desbois et al., 2010). The carapace of a namakier is typically composed of granular clastic material left behind after the shallower layers of salt have dissolved (e.g., Walker 1973). An annual temperature range of -0.5°C to 37.8°C was enough to facilitate the plastic deformation observed at Kuh-e-Namak (Talbot and Rogers, 1980; Tutiempo Network database). However, surface motion during dry periods not only depends on temperature but also the thermal gradient in the salt, which is dependent on the wetness of the salt (Talbot and Rogers, 1980). Like Iran, the semi-arid climate of the Kuqa fold-thrust belt allows the preservation of subaerial salt exposures. Here, annual rainfall averages ~74 mm (April-October) and average temperatures can range from -13.3°C to 31.2°C (Tutiempo Network, 2015).

### 3.2.3 Models, predictions, and tests

The almost immediate kinematic response of surface salt structures to temporary stimuli requires that subaerial salt evolution be not only considered in terms of long-term (centuries to millenniums) deformation but also short-term (hours to years) deformation

**Factors impacting subaerial salt structure motion**

| Variable | Temporal range | Spatial flow range | Kinematic response to external condition |
|---|---|---|---|
| Hot (surface temp.) | hourly, daily, seasonal | <mm to cm | 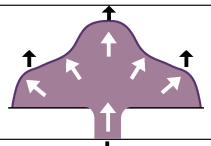 Thermal expansion may cause inflation and overall relative surface uplift of the namakiers when surface temperatures are high |
| Cold (surface temp.) | hourly, daily, seasonal | <mm to cm | 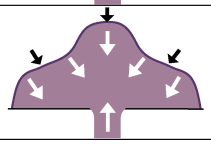 Thermal contraction may cause deflation and overall relative surface subsidence of the namakier when temperatures are low |
| Wetness | daily, seasonal | <mm to meters | 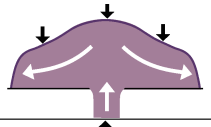 Meteoric waters facilitates pressure-solution GBS which accelerates salt flow. As salt spreads faster and further laterally, the namakiers' surface appears to subside |
| Dryness (*a*) | seasonal | <mm to cm | 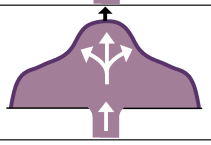 Dry-inflation scenario suggests the carapace, developed during dry periods, inhibits lateral spreading and facilitates swelling above the orifice resulting in relative surfac uplift above the orifice |
| Dryness (*b*) | seasonal | <mm to cm | 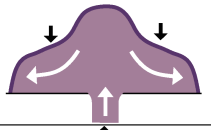 Dry-deflation scenario suggests the carapace, developed during dry periods, hinders uplift of the central dome and promotes lateral spreading resulting in surface subsidence of the namakier as it spreads laterally |
| Thin Overburden | seasonal, annually | <mm to cm | 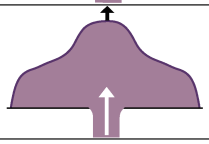 If enough material is removed from the top of a namakier, thereby reducing the overburden above the orifice, and causing an increase salt extrusion rate which results in surface uplift above the orifice |
| Thick Overburden | >annually | <mm to cm | 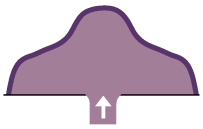 If a namakier carapace thickens significantly then the additional load from may cause enough resistance to decrease the salt extrusion rate resulting in reduced namakier growth |


Figure 3.2 Chart highlights variables that may control subaerial salt motion, their temporal and spatial ranges, and an illustration and description of the predicted kinematic impact. The purple areas represent aerial salt structures and the dark purple represents the salt structures' carapace. White arrows represent dominant salt flow direction. Black arrows represent surface displacement direction. Swelling of the salt in hot weather due to thermal expansion and deflation during cold weather because of thermal contraction may occur however the range of motion may be very small. During and shortly after rainfall events surface salt flow is predicted to accelerate significantly albeit short lived. During dry periods, 2 opposing models explain surface salt behavior: Dryness (a) predicts the strong carapace that develops during dry periods inhibits lateral spreading and facilitates swelling at the dome (above the orifice) as the salt extrudes from the feeder. Dryness (b) predicts that the thick carapace hinders uplift of the central dome and instead promotes lateral spreading. The presence of a thin weak overburden/carapace can potentially reduce overburden stress and accelerate salt extrusion. A thick, strong overburden/carapace may apply enough overburden stress to reduce salt extrusion rates.

kinematics (Figure 3.2). The long-term evolution of a namakier is dependent upon surrounding factors like the local tectonic regime and the structures' salt supply source (e.g., Hudec and Jackson 2007). Compressional tectonic settings can pressurize existing subsurface salt structures and facilitate salt migration (Hudec and Jackson, 2006). While extensional settings can provide near vertical conduits (normal faults) through which salt can passively rise (e.g., Hudec and Jackson 2007). The length of time a salt feeder extrudes salt to the surface is also dependent upon the supply source. If the supply source is drained or communication between the surface salt and the source layer is obstructed, diverted or otherwise cut off, that would mark the onset of the end of the namakiers' life.

Extreme daily temperature variations in semi-arid climates, like Kuqa fold-thrust belt, lead to oscillating inflation and deflation of a subaerial salt body on a sub-hourly to daily scale (Talbot and Rogers 1980). Referenced to the Earth's geoid, I would expect the entire surface of the namakiers to uplift during daylight hours, when surface temperatures can be very high, under the influence of thermal expansion (Merriam et al., 1962). Similarly, I expect subsidence across the namakier surfaces, as a result of thermal contraction, when temperatures drop well below freezing. Hourly sampling, at minimum, of temperature and surface motion would be necessary to detect the rate and degree of daily oscillations across the namakier surfaces at Kuqa fold-thrust belt. Similar inflation and deflation cycles in response to seasonal variations may also be detectable. However all these variations due to the thermal expansion or contraction of the salt body are small because the coefficient of the very low thermal expansion of NaCl, in the range of $5.10^{-6}$ $°C^{-1}$ (White, 1965). For example, assuming a homogeneous variation of 40°C on a 1 meter

thick salt layer, these thermal effects would result in a vertical displacement of the order of 200 micrometers.

The short-term deformation patterns of namakiers must consider the moisture at the surface, especially meteoric water. When sufficient quantities of meteoric water make contact with/infiltrate namakiers, pressure-solution and grain boundary sliding allow accelerated salt flow. I expect namakiers at Kuqa fold-thrust belt to flow faster within days after storm and rain events. As salt flow accelerates the leading edge of the surface salt bodies should extend further laterally. As lateral spreading of the namakiers occurs the surface of the namakier should appear to subside, relative to the Earth's geoid. This can be visualized by considering how a drop of molasses would behave on a tabletop. As the drop spreads slowly in every direction, the surface of the molasses will flatten and subside, bringing the top of the molasses closer to the table.

Two different models suggest conflicting roles of the carapace in surface salt kinematics during dry periods. One scenario is the dry-inflation model that suggests the carapace that develops on a surface salt body inhibits lateral spreading and facilitates swelling at the dome (above the orifice) as the salt extrudes from the feeder (Talbot and Pohjola, 2009). If this model holds for Kuqa fold-thrust belt then I should see a relative surface uplift above the orifice during dry periods. The other possibility, dry-deflation model suggests that the carapace hinders uplift of the central dome and instead promotes lateral spreading (Aftabi et al., 2010). If this model applies to Kuqa fold-thrust belt then I should see continual surface subsidence of the namakier as it spreads laterally, however this relative subsidence will be at a slower rate of lesser magnitude than the subsidence following wet periods. To test these models I must record time-lapse surface motions of the

Kuqa fold-thrust belt namakiers during wet and dry periods as well as document the occurrences of rain events and how much water is deposited on the surface.

The resistance supplied by a load overlying the orifice of a namakier is another factor that can potentially impact subaerial salt. Emergent, surface breaching, diapirs rise faster than pre-emergent diapirs because of the reduced confinement and load when the overburden is removed (e.g., Weinberg, 1993). Strain rates from microstructural analysis for pre-emergent diapirs range from $10^{-15}$ to $10^{-13}$ $s^{-1}$ while higher strain rates from $10^{-11}$ to $10^{-9}$ $s^{-1}$ have been observed for emergent diapirs (Talbot and Jackson, 1987). This aligns with flow velocities estimates that show pre-emergent diapirs in Germany rise ~0.3 mm/yr while rates of emergent diapirs in Iran can exceed 10 mm/yr (e.g., Trusheim, 1960; Talbot and Aftabi, 2004). Strain and velocity rates of pre-emergent and emergent diapirs reasonably suggest that the rate of salt extrusion can increase if enough material above the orifice of a namakier is remove.

Removal of material above the orifice can occur via erosion and salt dissolution. During periodic large storm events, the shallow, relatively uncompact layers of the namakier carapace can erode considerably (Wenkert, 1979). Furthermore, significant salt dissolution can occur during storm events if the carapace thickness allows sufficient meteoric water to infiltrate the namakier. In the event that the removal of material above the orifice is large enough, I expect acceleration of salt extrusion resulting in an overall rise of the namakier surface, relative to the Earth's geoid. Testing whether the surface uplift of the namakiers is due to long-term extrusion rates or accelerated extrusion due to load removal requires an extended temporal period of observation. Conversely, if the load above the namakier orifice controls the salt extrusion rate then a thickening carapace would cause

a deceleration of salt extrusion and result in a stagnant or subsiding namakier surface. The thickening of a carapace is likely to occur over much longer time periods, as it would take longer for material to accumulate above the namakier than it would for material to be removed.

## 3.3 Methods

Surface salt deformation is accessed using a remote sensing technique called interferometry of synthetic aperture radar across the subaerial salt bodies of interest. To perform the InSAR analysis I utilize Envisat ASAR (Advanced Synthetic Aperture Radar) imagery acquired between June 2003 and October 2010. To access the relationship between subaerial salt motions and climatic conditions I use climatic data from the Tropical Rainfall Measuring Mission (TRMM) as well as the nearest weather station during the same period, for which I have radar imagery across the structures. The maximum resolution of a dataset represents the smallest amount of detail that can be identified. If I consider the example of an optical image, the pixel size must be smaller than a given target in order for it to be detected; otherwise the pixel will be an average of the target and its surrounding area. Similarly, spatial and temporal resolution, or "pixel" of the present study is controlled by our data sources (Figure 3.3).

The temporal resolution of the Envisat imagery available must be less than the temporal range of surface salt motion to detect the salts' kinematic responses to climatic variations. Because of this it is unlikely that our Envisat dataset could resolve the impact of individual storm events as our best temporal resolution is 36 days. However, it is possible to detect the impact of seasonal climatic variations.

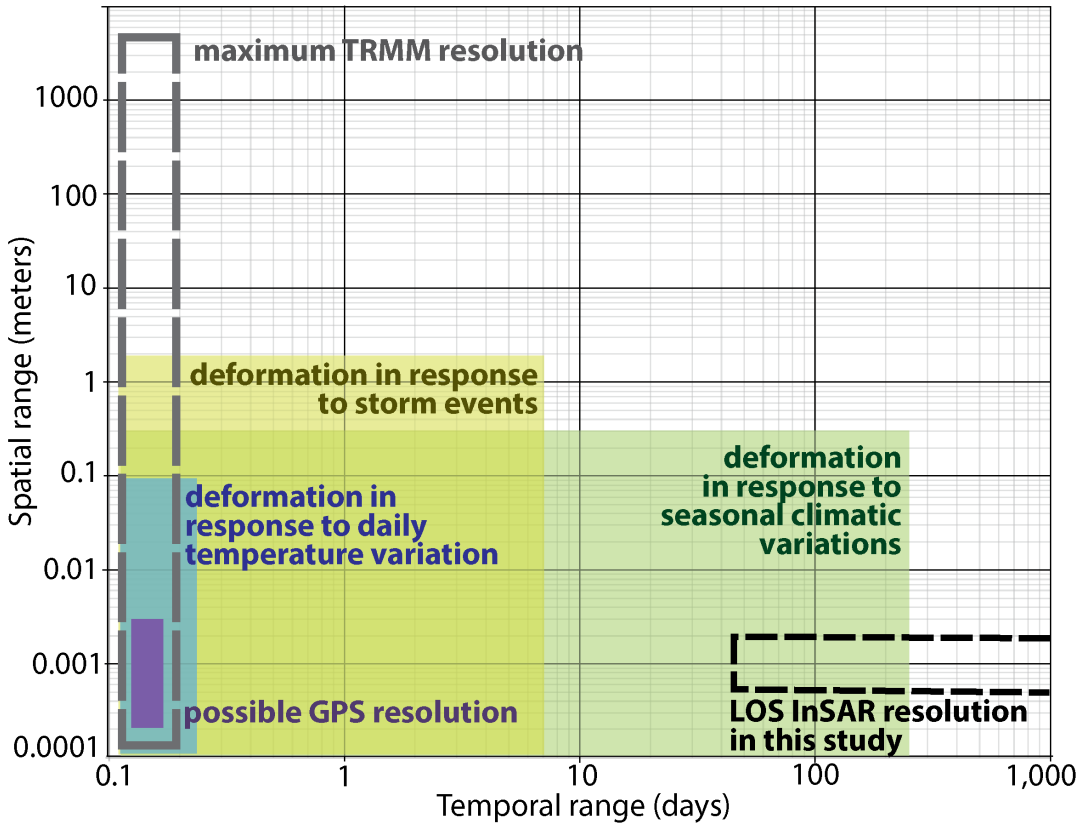


Figure 3.3 Logarithmic plot with spatial range in meters over temporal range in days. The yellow, green and blue regions represent the range of temporal and spatial scales that deformation in response to respective variables could be observed. The purple highlights possible GPS sampling resolution. The dashed black rectangle represents the maximum range of spatial and temporal sample of our Envisat dataset. Satellites like the Sentinel 1A and 1B have potential to reach temporal resolution of up to 5 days. The dashed gray rectangle represents the maximum Tropical Rainfall Measuring Mission (TRMM) resolution used in this study.

### 3.3.1 Climatic estimates

The TRMM satellite houses several precipitation-relevant instruments, including the Precipitation Radar (PR), TRMM Microwave Image (TMI), and Visible and Infrared Scanner (VIRS). The satellite has provided data since late 1997 and its spatial coverage is between latitude 50°S to 50° (Huffman, 2011). The Daily TRMM Rainfall Estimate (3B42 v7) used for our analysis is a product derived from rain gauge and multiple TRMM satellite measurements. First, independent precipitation estimates from various microwave

instruments (the TMI, Advanced Microwave Scanning Radiometer for Earth Observing Systems (AMSR-E), Special Sensor Microwave Imager (SSMI), Special Sensor Microwave Imager/Sounder (SSMIS), Advanced Microwave Sounding Unit (AMSU), Microwave Humidity Sounder (MHS)) are calibrated to TRMM Combined Instrument (TCI) precipitation estimates (Huffman, 2011). The 3-hourly multi-satellite measurements are combined with the accumulated monthly Global Precipitation Climatology Centre (GPCC) rain gauge analysis using inverse-error-variance weighting to form a monthly best-estimate precipitation rate (Huffman, 2011). Lastly, the 3-hourly estimates are scaled for the month then summed to the monthly value for each individual grid box (Huffman, 2011). The final data set has precipitation estimates with a 3-hourly temporal resolution and a 0.25°x0.25° spatial resolution (Huffman, 2011). This temporal resolution is sufficient to observe storms that can occur in the span of a few hours across the surface salt structures in Kuqa fold-thrust belt.

Another climatic dataset I have used includes daily humidity, temperature, and rainfall measurements from a meteorological weather station in Kuqa, Xinjiang Province, China (Tutiempo Network database). Although the weather station is far from our study area (over 150 km away) I utilize the available data because it is the closest ground truth. When I compare the rainfall estimates from the weather station and the TRMM dataset I look at the cumulative measurements for the time periods between each Envisat image acquisition. Similarly, I compared the average surface temperature and humidity during each time period between image acquisitions. The length of time between each image varies from 36 to 246 days with an average of ~75 days.

### 3.3.2 Interferometry of synthetic aperture radar (InSAR)

I constructed an InSAR time series to constrain the surface displacements of active extruded salt structures in western Kuqa fold-thrust belt as well as several surface displacements associated with hydrocarbon withdrawal and subsurface fluid injection. InSAR is a remote sensing technique that uses radar imagery to provide spatially dense measurements of surface displacements in the satellite line of sight (LOS) with millimeter to centimeter accuracy (e.g., Zebker et al., 1994; Massonnet and Feigl, 1998; Bürgmann et al., 2000). Multiple SAR images are used to generate sets of interferograms to form a time series after a joint inversion (e.g., Berardino et al., 2002; Schmidt and Bürgmann, 2003; Barnhart and Lohman, 2012). InSAR time series analysis helps reduce the impact of several noise sources (decorrelation, orbital and DEM errors, atmospheric delays, phase unwrapping errors) on displacement rates estimates during the time period spanned by the full dataset (e.g., Grandin et al., 2012) with an accuracy for surface displacement velocity at the mm/yr scale. The time series analysis also allows identification of time variable deformation including seasonal signals and response to earthquakes or anthropogenic activity (e.g., Lanari and Lundgren, 2004).

I used 40 ESA ASAR C-band radar images acquired by the Envisat satellite between June 2003 and October 2010 from Track 291 (along descending orbits). A small-baseline approach (e.g., Berardino et al., 2002) was used to process interferograms and invert for average displacement rates and evolution through time with the New Small Baseline Algorithm Subset chain, as described in detail by Doin et al. (2011) and Jolivet et al. (2013). All of the radar images were co-registered to a single master image and the interferogram network created was constrained by small perpendicular baselines. 85

individual interferograms were generated using a modified version of the Caltech/JPL Repeat Orbit Interferometry Package (ROI_PAC, Rosen et al, 2004) and inverted.

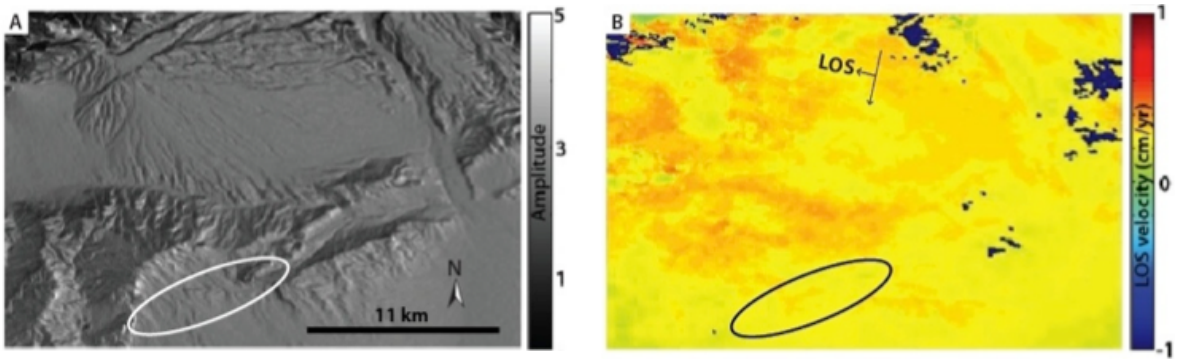


Figure 3.4 The ellipsoids highlight the general location of Tuzimazha salt wall in the amplitude (A) and displacement image (B). A. The amplitude SAR image of a region in northern Kuqa fold-thrust belt. B. Average surface displacement rate map in satellite line of sight (LOS), saturated to color scale -1 to 1 cm/yr. The Tuzimazha salt wall could not be resolved by the Envisat dataset.

Interferograms were corrected from DEM errors (Ducret et al., 2013) and stratified tropospheric delays (based on the ERA-Interim global atmospheric model, Doin et al., 2009; Jolivet et al., 2011), multi-looked by a factor of 4 in the range direction and 20 in the azimuth direction, flattened and filtered before unwrapping. The coherence was used to determine the optimal unwrapping path for each interferograms. The phase unwrapping was achieved iteratively, beginning in areas of high coherence then incrementally reducing the coherence threshold for each iteration (Grandin et al., 2012). Radar amplitude images were used to interpret the namakiers' boundaries, outlined on the velocity maps. The ~50 m thick Tuzimazha salt wall is the only known salt structure in western Kuqa that I are unable to spatially resolve with InSAR (Figure 3.4).

I present average velocity (mm to cm/yr) maps (Figure 3.5) displayed in line of sight (LOS) with positive (red) and negative (blue) values corresponding to movement

toward and away from the sensor. Differential incremental displacement maps and time series are used to track the temporal phase evolution. To isolate relative displacements, I generated these differential maps and time series computing the difference between time series from points within deforming areas and times series from local reference points. This helps minimizing the effect of spatially coherent noise. The remaining, relative, correlated temporal fluctuations observed and comparisons to climatic conditions are discussed in the following section.

The present study used three datasets that were processed to obtain a time-series that cover the period June 2003 to October 2010 where InSAR data provide estimates of surface displacement at a pixel size of ~30 m and time resolution of 36 to 210 days, with an average of 75 days. From the nearest weather station, average temperatures and precipitations are obtained. Finally, the TRMM data provide the same time-lapse series as the weather station, at a pixel size resolution of 4 km and for the same periods at the InSAR data. These three data sets are then processed to 1) analyze the surface deformation of salt bodies, 2) correlate these deformations with climatic variables.

## 3.4 Results

### 3.4.1 Kinematic observations

The overall distribution of LOS velocity at Bozidun namakier is relatively uniform. From the average velocity map, minor subsidence is observed on the western margin and localized uplift near the north and east (Figure 3.7A). The velocity distribution across Bozidun namakier is nearly indistinguishable from its immediate surroundings supporting field observations that suggest Bozidun namakier is not actively extruding material to the surface, as shown in the time series of the Figure 3.7.

The distribution of positive and negative LOS velocities at Daxiagu is asymmetrical and ranges from -4.5 to 5 mm/yr (Figure 3.7B). An area of uplift is observed on the eastern side of the structure, oriented toward the northwest. Areas of overall subsidence occur predominately on the western side of the structure as well as the northwestern. The incremental displacements maps highlight deformation patterns that do not reflect the long-term deformation patterns measured by the average displacement velocity maps (Figure 3.8). Each incremental displacement map of Daxiagu displays relatively uniform deformation across the namakier with fluctuations between surface uplift and subsidence at different time intervals. Time series analysis of east and west Daxiagu namakier inversely mirror each other; the east is uplifting at approximately the same rate (~4.5 mm/yr) as the west is subsiding. The ribbed pattern that appears in both the average velocity map and the incremental displacements maps do not correlate to topographical variations but instead may reflect noisiness in the data likely due to the namakiers' rugged surface.

Displacement velocities at Awate namakier are distributed asymmetrically (Figure 3.5C). Awate namakier is divided in two by a major river with stronger subsidence observed on the eastern segment, slight subsidence on the west, and uplift at the river channel in between. On the eastern Awate namakier the displacement velocities decrease radially away from the center and the maximum rate of displacement approaches -5 mm/yr. Incremental displacement maps show that the east Awate namakier has experienced periods of uplift despite overall subsidence suggesting it is an active structure. The areas of displacement at east Awate namakier have consistent shapes in the incremental displacement maps for periods of a year to three, but gradually shift from a central block to

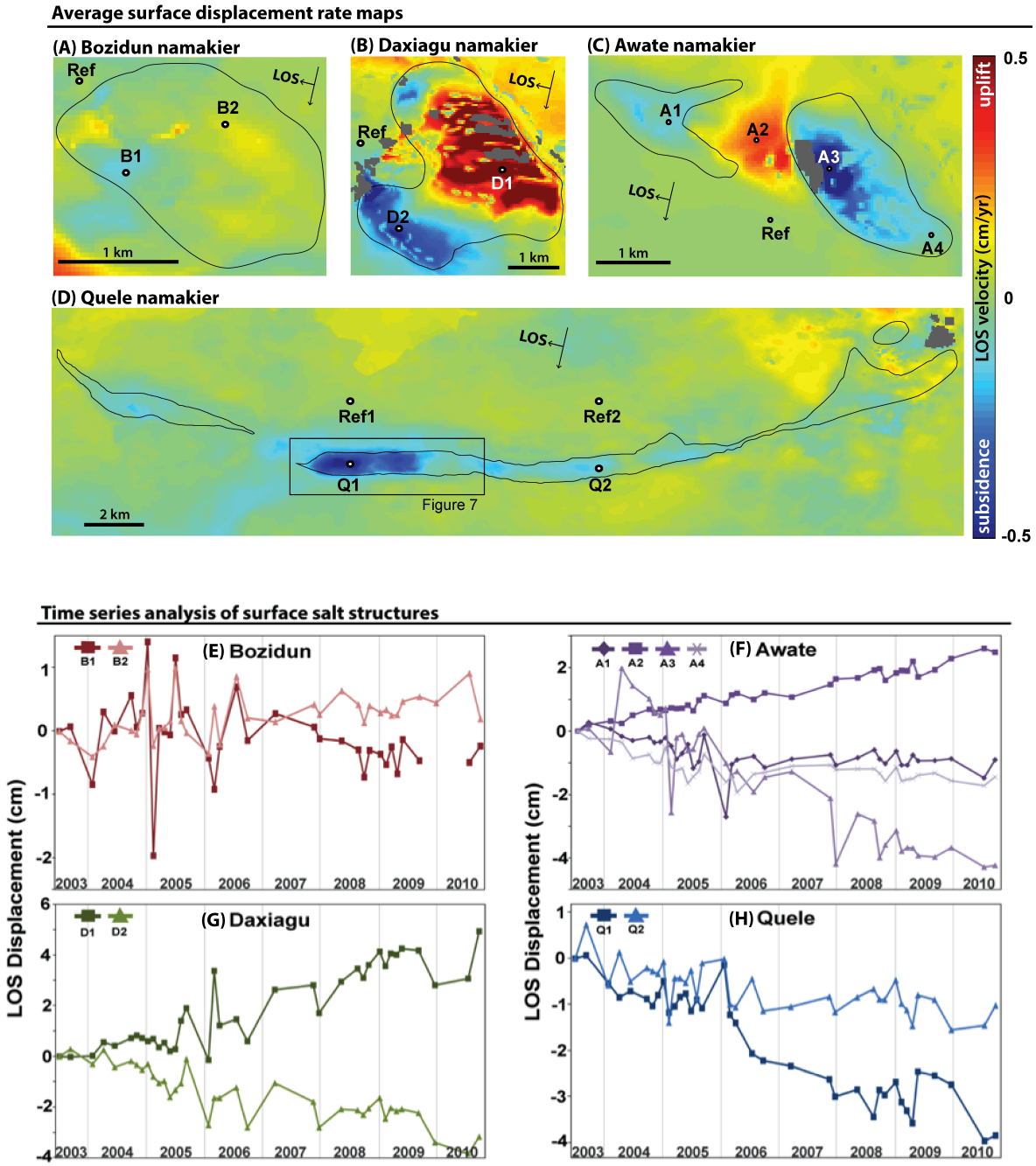


Figure 3.5 (Top) Average surface velocity maps for Bozidun namakier (A), Daxiagu namakier (B), Awate namakier (C), and Quele namakier (D) displayed in satellite line of sight (LOS) and saturated to the color scale 0.5 to -0.5 cm/yr. Surface movement toward (uplift) and away (subsidence) from the satellite is represented by warm and cool colors, respectively. (Bottom) Differential time series analysis of select points on Bozidun, Daxiagu, Awate, and Quele namakiers (locations are highlighted by black circles on the velocity maps above) is displayed in LOS displacement (cm) across time (from June 2003 to October 2010). The displacement measurements are relative to local references represented by the label "Ref".

Figure 3.6 Line-of-sight (LOS) differential incremental displacement maps of Daxiagu (1A-33A), Awate (1B-33B), and Quele namakiers (1C-33C), saturated to the color scale 5 to -5 cm. Displacement values of the local reference points (labeled in Figure 4.5) were removed from each incremental displacement map (Ref1 was used for Quele namakier) to reduce spatially coherent noise and highlight relative motion. Each incremental map spans the time between 2 successive acquisitions, the temporal coverage is represented by the shaded red area on each timeline.

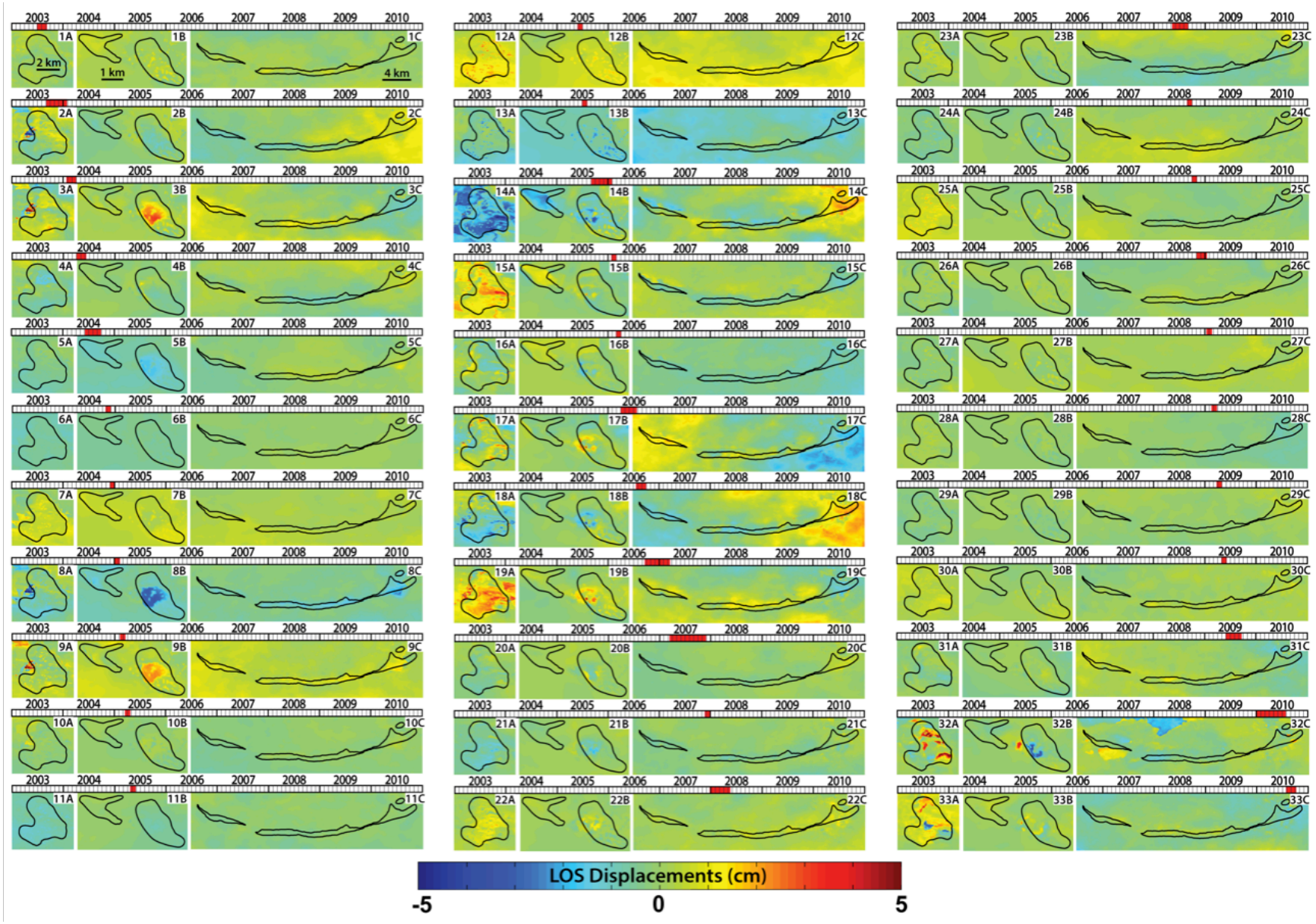
2003 2004 2005 2006 2007 2008 2009 2010
1A 1B 1C
2 km
1 km
4 km
2A 2B 2C
3A 3B 3C
4A 4B 4C
5A 5B 5C
6A 6B 6C
7A 7B 7C
8A 8B 8C
9A 9B 9C
10A 10B 10C
11A 11B 11C
12A 12B 12C
13A 13B 13C
14A 14B 14C
15A 15B 15C
16A 16B 16C
17A 17B 17C
18A 18B 18C
19A 19B 19C
20A 20B 20C
21A 21B 21C
22A 22B 22C
23A 23B 23C
24A 24B 24C
25A 25B 25C
26A 26B 26C
27A 27B 27C
28A 28B 28C
29A 29B 29C
30A 30B 30C
31A 31B 31C
32A 32B 32C
33A 33B 33C
LOS Displacements (cm)
-5
0
5

a more variegated area. These areas all subside and uplift more dramatically than the surroundings. Minor subsidence and unvarying incremental displacements are observed at west Awate namakier. Localized uplift at the river channel approaches 4 mm/yr. Incremental displacement maps show that the area of uplift, at the riverbed between the Awate namakier segments, initiated toward the western riverbank then propagated toward the center. The time series analysis at the river channel is notably less noisy and fluctuating than the time series from areas across the namakier, especially for east Awate namakier (Figure 3.5). This observation indicates that uplift at the river channel is relatively regular and constant while displacement of the namakier is relatively irregular.

The distribution of average displacement velocities across Quele namakier is predominately uniform (Figure 3.5D). Relative subsidence is measured along the exhumed thrust sheet, strong, localized subsidence is observed at the central segment of Quele namakier where the average displacement velocity approaches ~4 mm/yr. Velocities measured at Chaerhan namakier and the isolated salt dome at the eastern extent of Quele are within the noise level of background velocity measurements. A few periods of minor uplift are observed in the incremental displacement maps at the central segment despite the overall subsidence suggesting an actively extruding structure. Time series analysis shows the displacement trends of two areas in the central segment partially mirror each other, from 2003 to 2006. After 2006, higher rates of subsidence are concentrated toward the east suggesting heterogeneities along the salt thrust.

### 3.4.2 Kinematic and climatic correlations

To test the relationship between climatic conditions and surface displacements of namakiers in Kuqa fold-thrust belt I compare the incremental displacements between each

image acquisition to the average humidity, average temperature, and cumulative rainfall during the respective time intervals (Figure 3.7). There is no clear correlation between average humidity estimates and surface displacements for any of the studied namakiers. Similarly, no correlation is observed between displacements and average temperature for Quele namakier. Furthermore, correlation coefficients between surface displacement measurements on across the 4 namakiers studied and average temperature and humidity estimates yield a maximum correlation of 0.2. However, at Awate, Bozidun and Daxiagu namakiers I see temperature extremes are associated with more surface salt motion than intermediate temperatures. When I compare the displacements observed at the namakiers to the cumulative rainfall values estimated by TRMM as well as the distantly located weather station, I find a positive correlation. There is an increased occurrence of surface salt displacements during time intervals that experienced lower rainfall estimates suggesting that with less rainfall there is more surface motion. The correlation observed is not simply an artifact of having more data during periods of lower rainfall events because there are equal amounts of temporal coverage during the rainy (April-October) and dry seasons (October-April).

Another way to test the correlation between observed surface displacements and rainfall is to look at how the displacement residuals correlate to rainfall estimates. The residuals of a dataset are the observed values minus the predicted (or average) values. Residuals highlight the data points' deviation from the linear average, which are used to test the correlation between rainfall and surface salt displacement response. When I calculate the correlation coefficient between the residual time series displacements, showing the deviation of each displacement data point from the average, at the

Figure 3.7 Comparison between surface displacements at Kuqa fold-thrust belt and climatic conditions. I evaluate the dependence of incremental LOS displacement rates (cm) from each structure (Bozidun, Daxiagu, Awate, and Quele namakiers) to daily humidity (left), temperature (center left), and rainfall/snowmelt measurements (center right) at a meteorological weather station in Kuqa (Xinjiang Province, China) from Tutiempo Network and daily cumulative rainfall estimates from the Tropical Rainfall Measuring Mission (right).

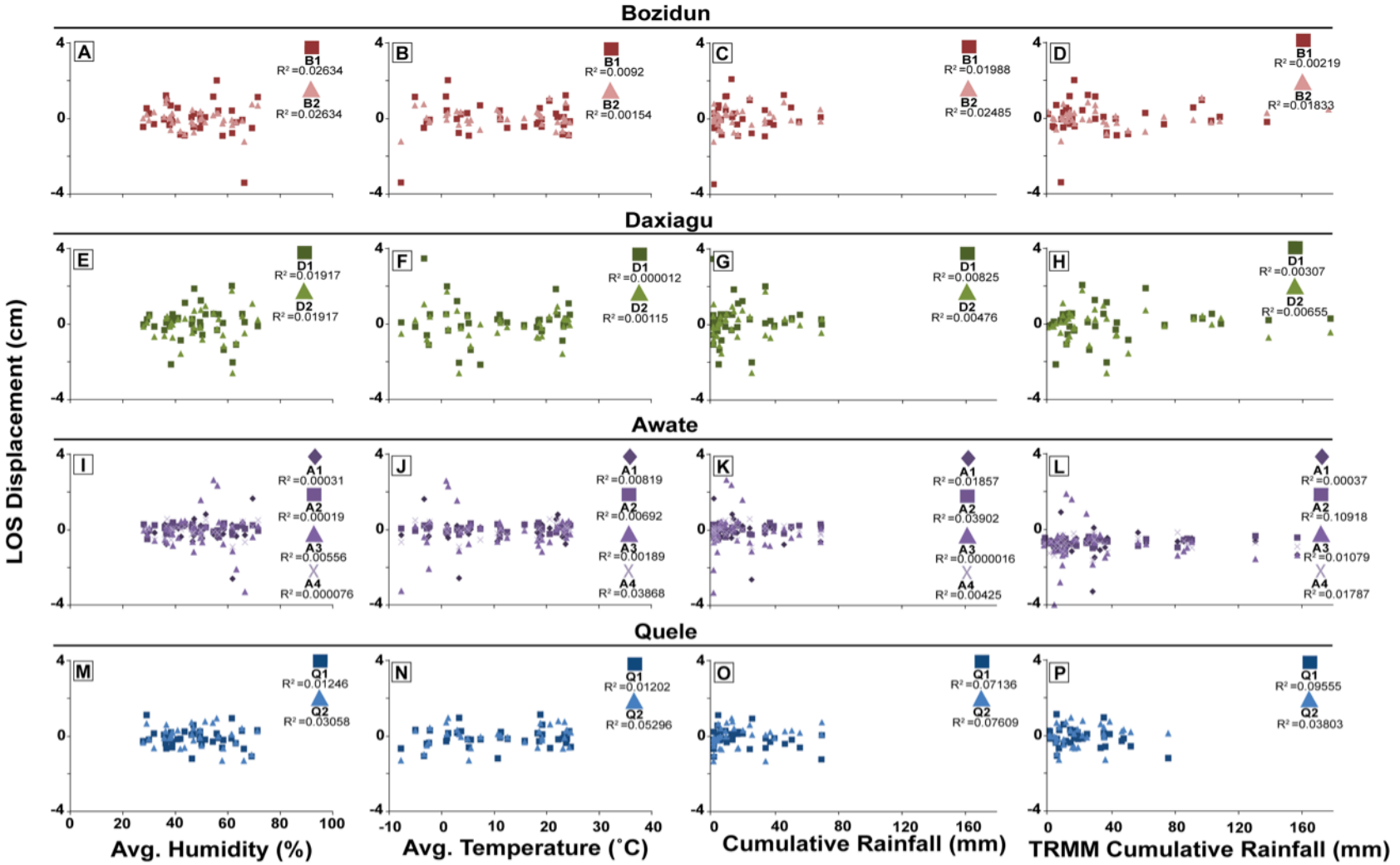
Bozidun
Daxiagu
Awate
Quele
LOS Displacement (cm)
A
B1 R² =0.02634
B2 R² =0.02634
B
B1 R² =0.0092
B2 R² =0.00154
C
B1 R² =0.01988
B2 R² =0.02485
D
B1 R² =0.00219
B2 R² =0.01833
E
D1 R² =0.01917
D2 R² =0.01917
F
D1 R² =0.000012
D2 R² =0.00115
G
D1 R² =0.00825
D2 R² =0.00476
H
D1 R² =0.00307
D2 R² =0.00655
I
A1 R² =0.00031
A2 R² =0.00019
A3 R² =0.00556
A4 R² =0.000076
J
A1 R² =0.00819
A2 R² =0.00692
A3 R² =0.00189
A4 R² =0.03868
K
A1 R² =0.01857
A2 R² =0.03902
A3 R² =0.0000016
A4 R² =0.00425
L
A1 R² =0.00037
A2 R² =0.10918
A3 R² =0.01079
A4 R² =0.01787
M
Q1 R² =0.01246
Q2 R² =0.03058
N
Q1 R² =0.01202
Q2 R² =0.05296
O
Q1 R² =0.07136
Q2 R² =0.07609
P
Q1 R² =0.09555
Q2 R² =0.03803
Avg. Humidity (%)
Avg. Temperature (˚C)
Cumulative Rainfall (mm)
TRMM Cumulative Rainfall (mm)

namakiers of interest and TRMM rainfall I find no correlation greater than 0.1. The low correlation coefficient is likely due to the occurrence of both positive and negative motion with hot and cold temperatures.

## 3.5. Discussion

InSAR analysis uncovers a variety of ground motions across the subaerial salt structures of the Kuqa fold-thrust belt. While the majority of the namakiers studied show surface motion, InSAR estimates of surface motion at Bozidun and Chaerhan namakiers are relatively indistinct from the surrounding area. Additionally, surface deformation at the Tuzimazha salt wall could not be confirmed due to the lack of spatial resolution (Figure 3.4). The namakiers exhibit asymmetrical spatial displacement patterns with fluctuating deformation rates over varying temporal scales (weeks to months). Average velocity estimates in addition to the incremental displacement steps allow us to explore the seasonality of subaerial salt deformation and its link to climatic conditions.

### 3.5.1 Daxiagu namakier

The asymmetric displacement pattern observed at Daxiagu namakier (Figure 3.8A) does not conform to the expected radial flow pattern of a salt fountain. The irregular shape and flow kinematics of Daxiagu is likely controlled by the surrounding topography and sub-salt morphology beyond the feeder, beneath the namakier. A river east of Daxiagu has eroded steep channel walls, and likely rapidly dissolves salt that flows toward the east.

Because surface uplift is expected directly above the feeder (orifice) of a point-source namakier, I interpret the area of overall uplift, on the eastern side of the namakier, corresponds to the location of the salt feeder. Long-term average uplift also suggests that the rate of salt extrusion into the namakier exceeds the rate of salt dissolution/erosion. The

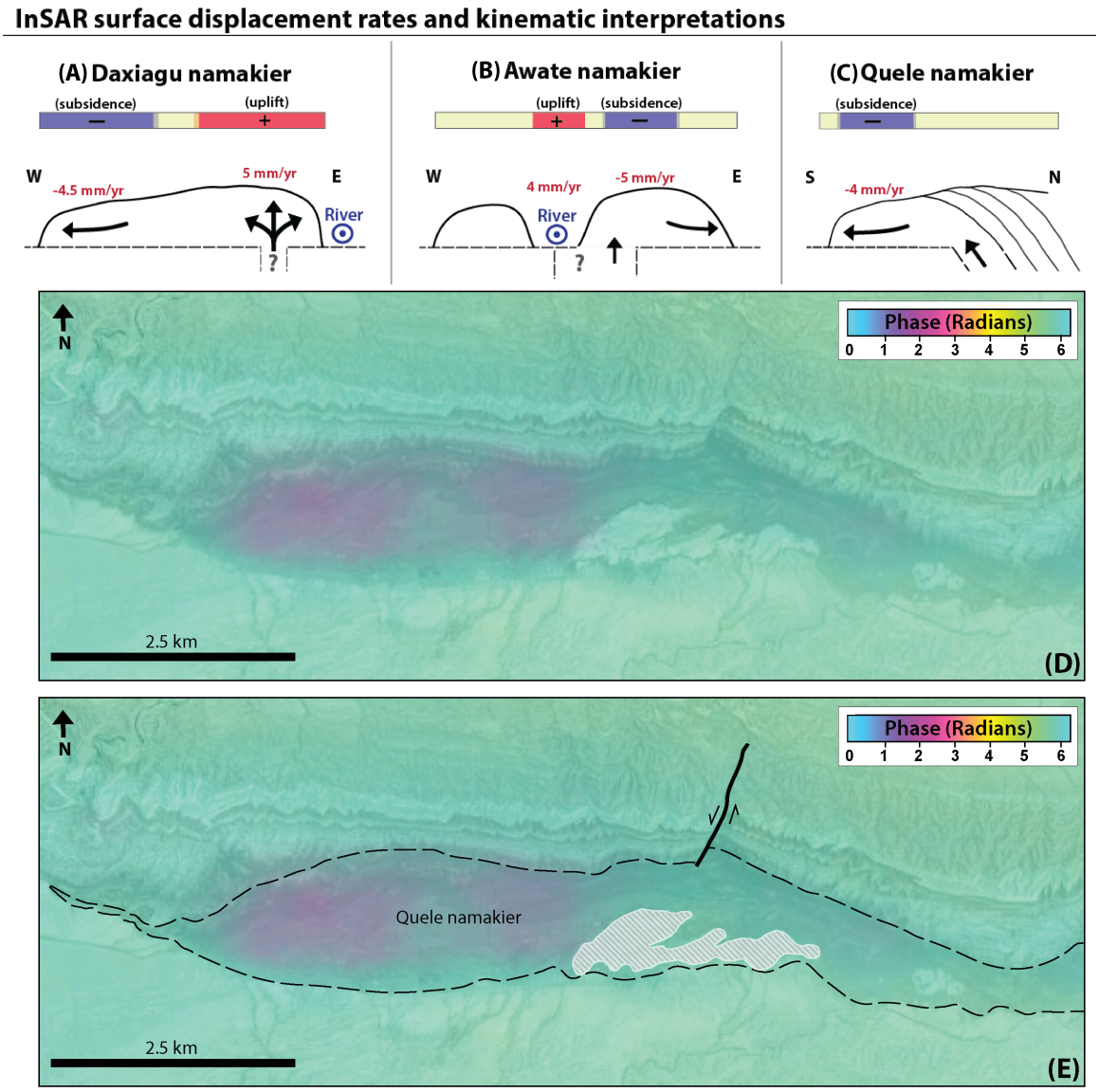


Figure 3.8 (A-C) Schematic cross-section and overview of displacement patterns across Daxiagu, Awate and Quele namakiers and kinematic interpretations. Daxiagu is interpreted to have an inflating dome that actively extrudes from salt feeder on the eastern side. Similarly, Awate is interpreted to flow predominantly toward the east to southeast. Awate is interpreted to have a salt feeder on the eastern segment that may be partially buried by the adjacent river channel causing the localized uplift. Unlike Awate and Bozidun namakiers, Quele namakier does not have a central dome because it is an exhumed salt thrust décollement. I interpret the dominant flow direction of Quele namakier to be toward the south. (D-E) The average displacement map (displayed in radians) overlain on top of a Google Earth image. The concentrated area subsidence at Quele corresponds precisely to a large raft immediately to the east of the area of deformation. The local left-lateral tear fault may also have created a structure barrier between this part and the rest of the namakier.

similarity in magnitude of surface displacement on the east and west may indicate the two sides of the namakier are not mutually exclusive. Diminutive subsidence at the northwestern margin could also indicate partial flow toward the northwest from the namakiers' dome (on the eastern side). The dominant direction of flow is interpreted to be toward the west, where I observe subsidence. As the salt glacier spreads further out, the glacier will be stretched further and the surface will subside relative to its surrounding. The southwestern lobe of Daxiagu is subsiding on average, but does not appear in the time-lapse data in any one time-step. However, I find no statistical correlation to suggest climatic conditions control the surface motion patterns measured. Furthermore, this observation is not likely to be climatically driven because I do not see it in incremental displacement maps. The active shortening accommodated across the Kuqa fold-thrust belt appears to be have a greater influence on the exhumation rates and subsequent surface displacement patterns.

### 3.5.2 Awate namakier

The subsidence measured at eastern Awate namakier (Figure 3.8B) branch is concentrated at the center of the structure. The broad, long-term deformation pattern of centralized subsidence is indicative of a mature namakier that is experiencing a higher rate of dissolution/erosion that exceeds the rate salt is feed into the structure. However, salt mining operations purposely introduce water into the southwestern boundary of eastern Awate namakier branch. After the water has dissolved halite from the namakier, it is collected in large bins. These mining operations have the potential to influence the observed long-term subsidence by locally increasing salt dissolution.

Incremental displacement maps do not entirely correspond with observations from the average displacement velocity map revealing different deformation patterns at different temporal scales. Unlike the long-term displacement pattern, four intervals of incremental surface uplift at eastern Awate namakier occur between January and March (colder/drier months) confirming that new material (salt) is being fed into the namakier. I observe uplift when our temperature-kinematic salt models predict Awate would experience overall surface subsidence during colder periods in response to thermal contraction. Calculated correlation coefficients between incremental displacements and temperature variations show no statistical correlation. Temperature variations do not appear to control periods of wide spread uplift and subsidence. The intervals of uplift do, however, support the dry-inflation model. The dry-inflation kinematic salt model predicts a namakier would dome inflation during dry periods because the carapace inhibits surface uplift. At Awate namakier I observe uplift above our a central location (dome) during periods of low rainfall implying that the carapace restricts lateral spreading and prefers dome inflation during dry periods. Furthermore, periods of increased rainfall do not correspond to increased surface salt motion.

The average, long-term (~7.3 years) uplift signal measured at the river channel between the east and west segments is not notably observed in the incremental displacement maps. If river deposition were responsible for the rise of the river channel surface between the Awate namakier branches, the area of uplift would not be as localized as observed. Instead, the rise would continue as the river does, toward the south. It is more likely that the concentrated uplift observed at the river channel is due the rise of salt from the source layer through the stem of the diapir that feeds Awate namakier. In the case that

the river cuts off the salt feeder that sources Awate, the observed uplift could be the result of accumulating strain in the overburden of a partially buried, active salt feeder. However, the estimated long-term rate of uplift here is not likely to persist for time scales of >100 years because that would significantly perturb the long-term equilibrium topography by developing a hill in the very place there is a river. It is possible to perturb the equilibrium topography if the diapir is new or suddenly changing character, but it is not new because the namakier is well established. Thus, I interpret the equilibrium to be controlled by the regular frequency of large flooding events allowing this area to neither rise nor fall with respect to regional baseline for longer periods than ~7 years. A study of climatic conditions from 1951 to 2009 in Xinjiang, China reveals that the average precipitation has increased by 15 mm/yr since 1990 (Kong and Pang, 2012). To our knowledge, a detailed study of this particular river does not exist. However, work done on the proximal Tailan River, west of Awate, found that glacial melt-water accounts for 60% of its 7.5 x $10^8$ $m^3$ annual river discharge (Zhao et al., 2015). The combination of increased rainfall and possible glacial melt-water, due to the 1˚C raise in average annual temperature, would facilitate flash-floods every 10 to 100 years that removes a lot of material through erosion, maintaining a topographic equilibrium (Kong and Pang, 2012).

### 3.5.3 Quele namakier

Quele namakier (Figure 3.8C) is the exhumed portion of a significant salt thrust and its surface kinematic patterns vary from typical salt fountains. Because it is a line-source structure, I do not expect to see radial flow comparable to a point-sourced structure. Unlike a salt fountain, if the exhumation rate of Quele namakier increases the surface is not likely to uplift significantly because it is confined by its overburden, the hanging wall of the

Quele salt thrust. Instead I would see increased subsidence due to amplified southward spreading. Decreased exhumation would result in stagnant to minimal lateral spreading.

Overall subsidence is observed across Quele namakier but one area of the structure has experienced a notably higher rate of subsidence. At Quele there is a distinct split in kinematics between the region sampled by "Q1", and the area just over 2 km east labeled "Q2" that shows up both in the average velocity maps (Figure 3.5), and in many individual incremental displacement time steps (Figure 3.6). The other active salt surface structures at Kuqa fold-thrust belt are point-source structures making along-strike variability significant here. Climatic variations are unlikely to be responsible because I see no statistical relationship between surface motion and climatic variations (temperature and moisture). Furthermore, even if our sampling rate is not sufficient to see a climatic correlation, there is no reason climate conditions would exclusively and consistently affect only one spot along a relatively smooth hill-front. However, the area of concentrated subsidence does correlate to local structural features (Figure 3.8E). A large siliciclastic rock body borders the eastern extent of the area of subsidence. A sizable left-lateral tear fault in the hanging wall of the Quele salt thrust also occurs in the vicinity. The siliciclastic rock body here may form a structural barrier between the area of subsidence and the rest of the namakier meaning the deformation observed in this localized area is decoupled from deformation observed along-strike.

## 3.6 Conclusions

In this study I present quantitative estimates of sub-aerial salt displacement rates of surface salt bodies in Kuqa fold-thrust belt of northwest China. Iranian surface salt structures, our predominant analog, have demonstrated a strong dependence of surface salt

motion on climatic condition. I predicted similar relationships for Kuqa fold-thrust belt subaerial salt bodies but discovered climatic conditions do not control surface kinematics as it does in Iran despite similar climates. The kinematic analysis I conducted is a progressive step toward understanding the dynamics of the system. Our work compliments the field study (Li et al, 2014) that details the geometric properties of namakiers in western Kuqa fold-thrust belt with active surface kinematic measurements of Bozidun, Daxiagu, Awate, and Quele namakiers. I measure the dominant vertical displacement and identify asymmetric deformation patterns of uplift and subsidence at Daxiagu and Awate, likely controlled by local tectonics and topography. At Quele namakier I identify areas of concentrated subsidence that are more responsive to structural barriers than climatic conditions. A maximum InSAR temporal resolution of ~36 days render difficult any seasonality of surface salt deformation. Across Kuqa fold-thrust belt, I discovered that subaerial salt motion is decoupled from climatic conditions. If seasonality of subaerial salt deformation at Kuqa fold-thrust belt occurs on temporal ranges less than 36 days, shorter sampling rates are required. The potential of time delays in the salts' response to surface conditions could explain the limited correlation between surface displacement and climatic conditions. The sparse temporal sampling of this Envisat dataset is significantly limited when compared to the daily sampling rate of temperature and rainfall from space-borne satellites or ground-based weather stations. Additionally, the restricted spatial rainfall resolution of ~4 km estimates from space-borne satellites may also preclude correlation with meter-scale InSAR sampling resolution. Looking forward, the association of the European Space Agency's Sentinel 1A and 1B at the end of 2016 could provide improved

temporal coverage and better quantify the temporal fluctuations that may reveal the climatic dependence I expect.

# CHAPTER 4
# ANTHROPOGENIC DEFORMATION ACROSS DAWANQI OIL FIELD IN NORTHWESTERN CHINA

## 4.1 Introduction

Extraction of subsurface hydrocarbons started in the early 19th century and is projected to continue for decades to come (Lamb, 2010). As the world population continues to grow and developing countries advance, the global demand for hydrocarbons will remain high and I will be forced to explore in new places that may include populated regions. Hydrocarbon exploration involves many risks throughout the life cycle of any given field, from personal safety to environmental protection. One particularly alarming risk is ground displacement caused by reservoir fluid extraction or injection. Unnaturally rapid rates of subsidence and/or uplift are critical to understand because of the extreme hazard potential that can lead to infrastructure damage and increased flood potential (Fielding et al., 1998).

Ground leveling surveys have been used to detect surface motion around oil fields. More recently, interferometry of synthetic aperture radar has been used to measure anthropogenically-influenced deformation (e.g., Rutqvist et al., 2010). Surface subsidence resulting from hydrocarbon extraction was first identified almost a century ago in the Goose Creek oil field in Baytown, Texas (Pratt and Johnson, 1926). Since then the occurrence of anthropogenically-induced deformation has been observed across the globe, and it is now well known that fluid extraction may lead to land subsidence (i.e., Galloway et al. 1998; Saif et al., 2006; Teatini et al., 2011). Conversely, the occurrence of surface uplift caused by fluid (water or gas) injection has only recently been noted (Teatini et al., 2011; Ji et al., 2016). Even more unusual is the occurrence of significant subsidence

immediately adjacent to notable surface uplift, as observed at the Dawanqi oil field in the Kuqa fold-thrust belt of northwestern China.

The Dawanqi oil field has been in production since 1997 and continues today. The oil field exhibits signs of anthropogenically-influenced deformation evidenced by surface displacements measured with interferometry of synthetic aperture radar (InSAR). Because there is no evidence that enhanced-oil-recovery injection is in practice here, the juxtaposition of subsidence and uplift in the area may be explained by a combination of fault slip and reservoir volume change. However, if hydrocarbon production is limited enough to avoid sufficient volume loss that would cause surface subsidence then the observed deformation may only be tectonically related.

Continued improvements in synthetic aperture radar interferometry (InSAR) and radar data availability have made it possible and cost efficient to monitor surface motion over large spatial and temporal scales. Using this technology to record, analyze and ultimately understand how the shallow crust responds to subsurface fluid extraction and fluid injection is critical as I continue to explore the sustainability of reservoirs subjected to carbon sequestration, nuclear waste disposal, and water injection. Here I provide a case study of anthropogenically-induced uplift and subsidence in the Dawanqi old field of the Kuqa fold-thrust belt of NW China, constrained by InSAR measurements.

## 4.2 Background

### 4.2.1 Geologic setting

The Dawanqi oil field is centrally located in western Kuqa foreland fold-thrust belt that is situated immediately south of the Tian Shan and north of the Tarim basin (Figure 4.1). The Kuqa fold-thrust belt is an active system that accommodates north-south

shortening across a ~400 km long, ~20-65 km wide region (e.g., Allen et al., 1991; Zhong and Xia, 1998; Yang et al., 2010). Compressional salt tectonics across Kuqa fold-thrust belt are responsible for structural traps that have collected volumes of oil and gas, presently being extracted. The deformational style in western Kuqa is controlled by the presence and varying thickness of salt (e.g. Tang et al., 2004; Chen et al., 2004).

The majority of the hydrocarbon traps contained within Kuqa are gas fields with oil fields accounting for a smaller percentage. Hydrocarbon reservoirs have been charged from subsalt Triassic-Jurassic coal and lacustrine mudstones type III source rocks (Hendrix et al., 1992; Chen et al., 2004; Zhao et al., 2005). Potential reservoirs exist in faulted and folded interbedded clastics and carbonates within the salt sequence. However, the larger gas fields have been discovered within subsalt structures (Chen et al., 2004). Migration of hydrocarbons along permeable layers in the subsalt and suprasalt sequences that were juxtaposed by faults allowed suprasalt reservoirs to form as well (Tang et al., 2004). The salt-cored Dawanqi anticline in western Kuqa contains a proven reservoir that is one of few reservoirs contained within the suprasalt sequence (Tang et al., 2004). Fault block traps and lithostratigraphic traps control the geometry of the Dawanqi oil reservoir. Across Kuqa, oil and gas fields are sourced from type III source rocks. The oil reservoir drilled in Dawanqi is made up of the Neogene Kangcun Formation and Quaternary sandstone at a depth between 200-600m with a thickness of 0.5-9m (Yuan Neng - PetroChina, personal communication) is made up of the Neogene Kangcun Formation and Quaternary sandstone at a depth between 200-600m with a thickness of 0.5-9m (Yuan Neng - PetroChina, personal communication).

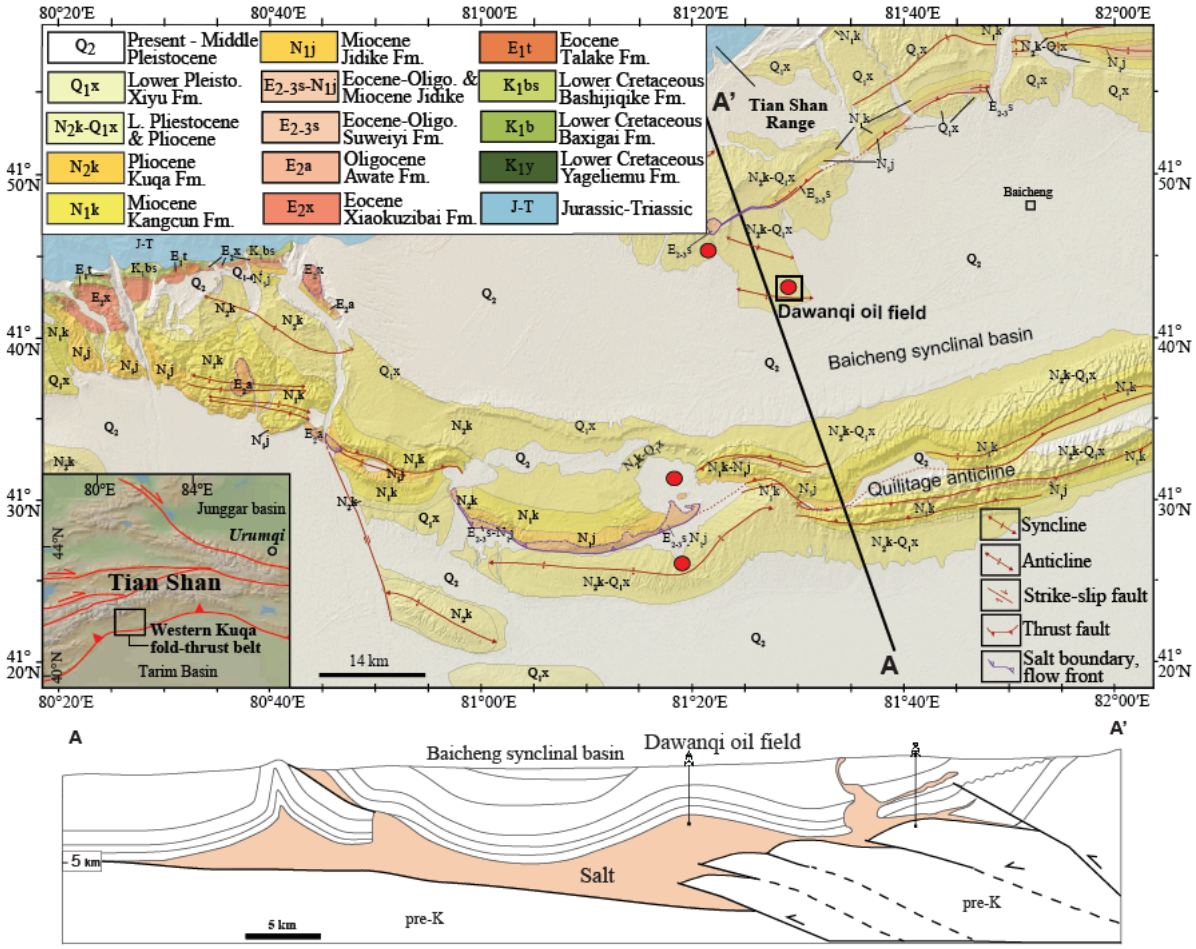


Figure 4.1 Geologic map adapted from Li et al., 2014 of the western Kuqa fold-thrust belt. Blues and greens correspond to Mesozoic Tian Shan bedrock. Yellows and oranges correspond to Cenozoic basin deposits. The cross-section profile, also adapted from Li et al., 2104, runs from the southern Tian Shan front, across the Dawanqi oil field and Baicheng minibasin, and through the North and South Qiulitage anticline.

### 4.2.2 Deformation influenced by fluid extraction/injection

Areas in which fluid is injected or withdrawn experience different mechanical processes that result in uplift and subsidence, respectively. Pore pressure decreases when fluid is removed from the formation of interest causing an increase in the effective stress (Terzaghi, 1925). The spatial distribution, magnitude and rate of subsidence depends on factors such as the amount of fluid withdrawn, the pore pressure decrease, depth, volume,

and permeability of the formation, as well as the mechanical properties of the reservoir and overburden (Teatini et al., 2011). Hydrocarbon extraction leads to bowl-shaped subsidence that is greatest at the center of the field because a production well disturbs the natural fluid flow of the system and produces a cone of depression in the fluid head of the pumped formation that extends laterally and vertically

(Gambolati et al., 2005).

In contrast, when fluid is injected the pore pressure increases thereby decreasing the effective stress (Terzaghi, 1925). Deformation of the injected formation is driven by the in situ pore pressure and temperature variations while the amount of surface motion above the reservoir is controlled by the depth, thickness, volume, compressibility and the thermal expansion coefficient of the formation (Teatini et al., 2011). Hydrocarbon extraction has been aided by fluid injection since the 1940s and is extensively used in hydrocarbon production however much of the deformation resulting from it has gone unnoticed until recently (Teatini et al., 2011; Ji et al., 2016). In most cases, the apparent environmental and infrastructural hazards were insignificant to warrant large enough leveling surveys to monitor surface uplifts (Teatini et al., 2011). However, over the last 2 decades, significant improvements in synthetic aperture radar interferometry (InSAR) and radar data availability have made it possible to monitor surface motion over large spatial and increasing temporal scales.

## 4.3 Interferometry of Synthetic Aperture Radar (InSAR)

### 4.3.1 InSAR processing

InSAR is a remote sensing technique that uses radar imagery to provide spatially dense measurements of surface displacements in the satellite line of sight (LOS) with

millimeter to centimeter accuracy (e.g., Zebker et al., 1994; Massonnet and Feigl, 1998; Barnhart and Lohman, 2012). I use Envisat Advanced Synthetic Aperture Radar (ASAR) C-band radar images acquired along Track 291 (descending; North to South) between September 2003 and October 2010. Individual interferograms were processed and inverted with an adapted version of the Caltech/JPL Repeat Orbit Interferometry Package (ROI_PAC, Rosen et al, 2004) that utilizes the New Small Baseline Algorithm Subset (NSBAS) chain, as described in detailed by Doin et al. (2011) and Jolivet et al. (2013). Digital Elevation Model (DEM) error corrections (Ducret et al., 2013), stratified tropospheric delay corrections (based on the ERA-Interim global atmospheric model, Doin et al., 2009; Jolivet et al., 2011), flattening and filtering were completed prior to phase unwrapping. The phase unwrapping was done iteratively, using interferogram coherence to determine the optimal unwrapping path (Grandin et al., 2012). The time displacement history is then inverted pixel-by-pixel, and a linear rate map was generated in radar coordinates then georeferenced (e.g., Berardino et al., 2002; Schmidt and Bürgmann, 2003; Doin et al., 2011; Barnhart and Lohman, 2012). The final displacement maps were resampled to 30 m spatial resolution.

The average velocity (mm to cm/yr) maps are displayed in line of sight (LOS) with positive (red) and negative (blue) values corresponding to movement toward and away from the sensor (Figure 4.2). Because our radar dataset is dominantly sensitive to vertical motion I interpreted positive and negative measurements to indicate uplift and subsidence, respectively. Cumulative and annual average displacement maps are with respect to a local reference point, labeled “Ref” in Figure 4.2. I isolate local displacements by subtracting the displacements observed at the reference point from the immediate area (Dawanqi oil field).

This helps minimizing the effect of spatially coherent noise and focus on the areas of deformation associated with the oil field.

### 4.3.2 InSAR observations

The cumulative deformation revealed by InSAR (Figure 4.2A) over the Dawanqi oil field ranges between 5 to -5 cm over ~7.3 year sampling period. Spatially, the uplift signal is bulbous-shaped, decreasing radially from the center and extending further toward the north. The area of subsidence forms a more elongated shape in the E-W direction asymmetrical. Time series analysis of two locations at Dawanqi oil field acceleration in uplift and subsidence at D1 and D2, respectively, occurred after mid-2005.

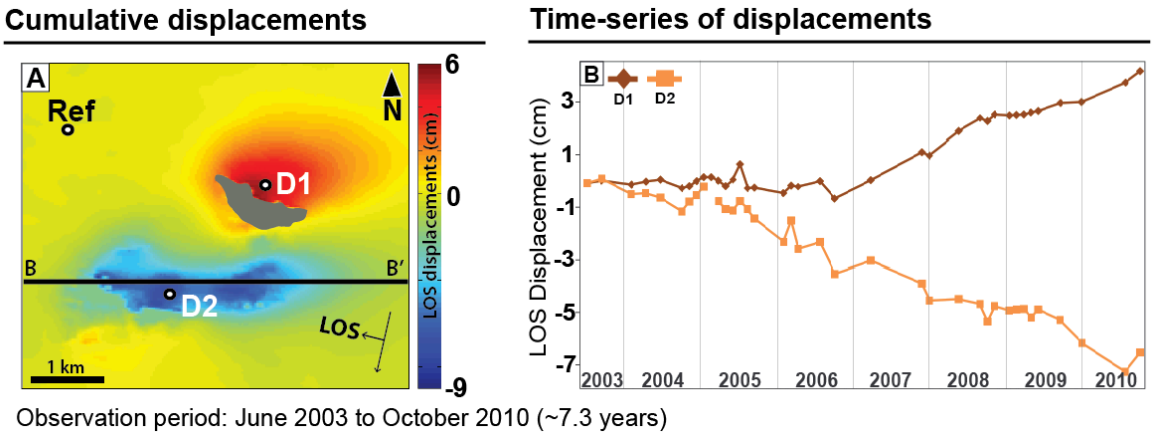


Figure 4.2 InSAR results displayed in cumulative displacements (A) and time series (B) of select areas. The cumulative displacement map is saturated to the color scale -5 to 5 cm, with a temporal coverage from 2003 to 2010. The satellite flight path is descending (SW direction) and the satellite Line of Sight (LOS) is perpendicular to the flight path. Positive (cool colors) and negative (warm colors) LOS velocity values correspond to motions toward and away from the satellite, respectively. The gray area represents a region with poor coherence. The time series profiles track the temporal LOS displacement evolution of specific points on the surface (D1 and D2).

## 4.4 Surface displacement models

### 4.4.1 Fault slip model parameters and results

**S**urface displacements associated with simple fault slip were modeled to access the potential that deformation observed at Dawanqi oil field is the result of an active fault (Okada, 1985; Beauducel, 1997). I modeled displacements at the surface of an elastic half-space, due to a dislocation defined by rake and slip on a 5x3 km rectangular fault. The fault is defined by length, width, depth, strike, and dip, with a centroid located at (0,0, -depth). The kilometer length unit is used for all aforementioned variables. The fault parameters applied follows Aki and Richards, 1980, where reverse and normal faults have a rake of 90˚ up or down, respectively, striking N80˚W and dipping NE70˚.

North-dipping reverse faults and south-dipping normal faults produced surface uplift comparable to our InSAR observations of uplift toward the north and subsidence toward the south (Figure 4.4). Various depths of the fault produced varying surface displacement geometries and 3 km depth was determined to produce a displacement pattern most comparable to our InSAR results (Figure 4.5), testing fault slip amounts between 10 and 30 cm on 5 cm increments. Fault slip between 20-30 cm along the north-dipping reverse fault produces vertical surface displacement in the hanging wall comparable to our InSAR results. Similarly, fault slip across the south-dipping normal fault ranging between 20-30cm produces vertical surface displacement patterns in the hanging wall that comparable to the subsidence I have calculated using InSAR. However, I found no single model that can accomplish both surface uplift to the north and subsidence to the south at the same quantities I observe.

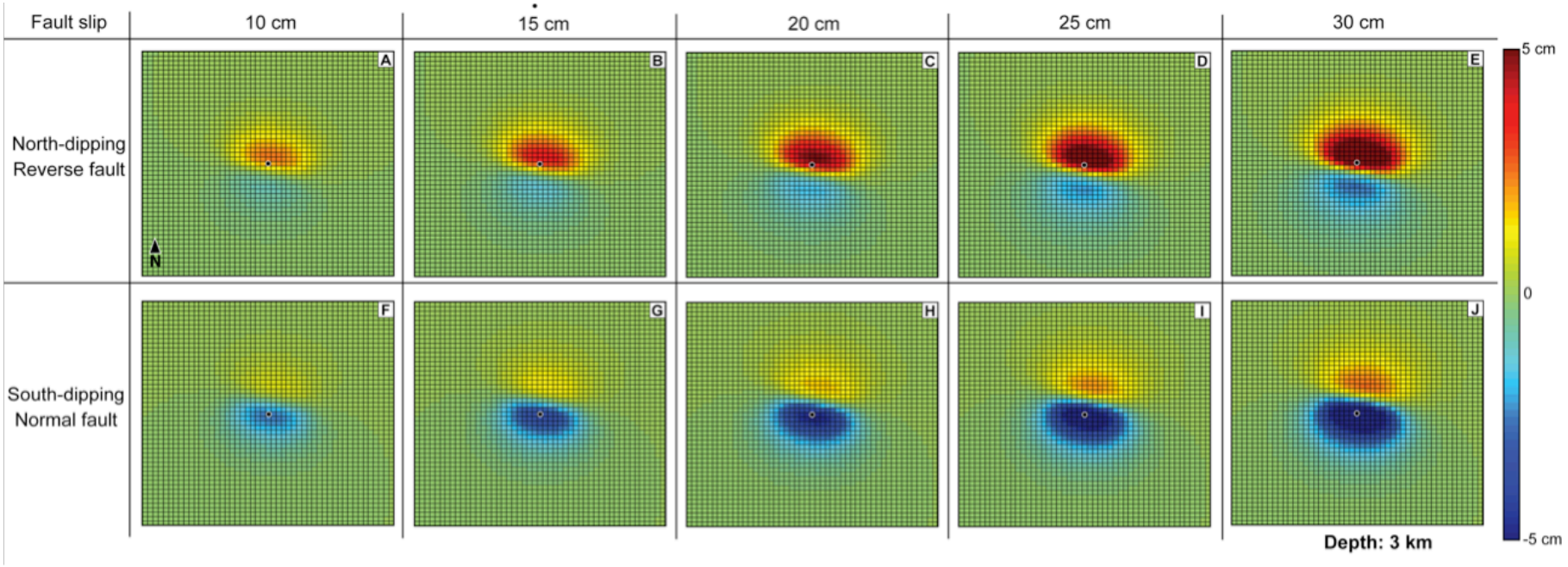


Figure 4.3 Modeled vertical component of surface displacement associated with varying fault slip. The black-filled circle in each map represents the fault centroid located at 3 km depth, striking N80˚W and dipping 70˚NE. The maps are saturated to the color scale -5 to 5 cm. Like the InSAR map, cool and warm colors correspond to subsidence and uplift, respectively. (A-E) The top row shows surface displacement due to slip along a north-dipping reverse fault. (F-J) The top row shows surface displacement due to slip along a south-dipping normal fault.

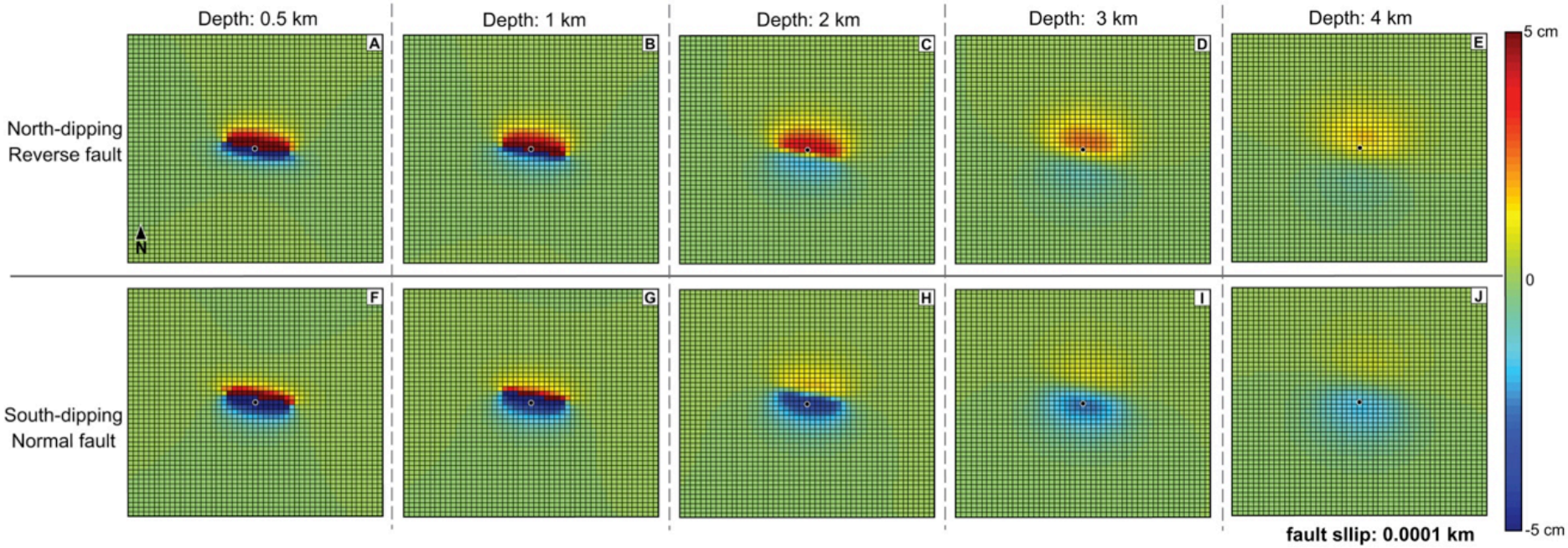


Figure 4.4 Modeled vertical component of surface displacement associated with fault slip of 10 cm and varying fault type, dip direction and depth. The black-filled circle in each map represents the fault centroid located at varying depths (0.5 to 4 km), striking N80˚W and dipping 70˚NE (A-E) or 70˚NE (F-J). The maps are saturated to the color scale -5 to 5 cm. Like the InSAR map, cool and warm colors correspond to subsidence and uplift, respectively. (A-E) The top row shows surface displacement due to slip along a north-dipping reverse fault. (F-J) The top row shows surface displacement due to slip along a south-dipping normal fault.

### 4.4.2 Anthropogenically induced subsidence model parameters and results

I modeled two-dimensional surface displacement induced by reservoir volume change along a profile using work done by Segall, 1989 (Equation 7b), reviewed in detail therein.

Equation 4.1: $$U_y(x=0,y,t) = \frac{2(1+v_u)BT\Delta m(t)}{6\pi\rho_o} * log\left[\frac{1+\xi_+^2}{1-\xi_-^2}\right]$$

$$where \;\; \xi_+ = \frac{y+a}{D} \;\; and \;\; \xi_- = \frac{y-a}{D}$$

The vertical surface displacement $U_y$ is a function of Poisson's ratio ($v_u$), reservoir thickness ($T$) and depth ($D$), fluid mass volume change $\Delta m(t)$, Skempton's coefficient (B), fluid density ($\rho_o$) and the assumption that $\Delta m$ is uniform over the interval $-a < y < a$ (where $y$ is the center of dilatation.

A simple profile was modeled instead of a grid because of our limited access to reservoir details. For comparison purposes, I plot the model results at a length scale equivalent to the InSAR profiles where each point, or pixel, along the profile (x axis) covers 30 m. The vertical surface displacement is a function of reservoir thickness and depth, fluid mass volume change, fluid density and the assumption that fluid mass volume change is uniform over a 30 m interval from the center of dilatation. The constants include the reservoir thickness of 9 m and depth of 400 m, the fluid density value of 0.88 g/cc and undrained Poisson's ratio of 0.33. The only input I vary, to match the InSAR results, is the fluid mass volume change. Three locations that correspond to areas of peak subsidence measure by InSAR, are tested as the center of dilatation (y = 37, y = 66, and y = 100).

The amount of reservoir volume loss necessary to achieve the InSAR derived cumulative displacement estimates varies across the Dawanqi oil field (Figure 4.3). When I

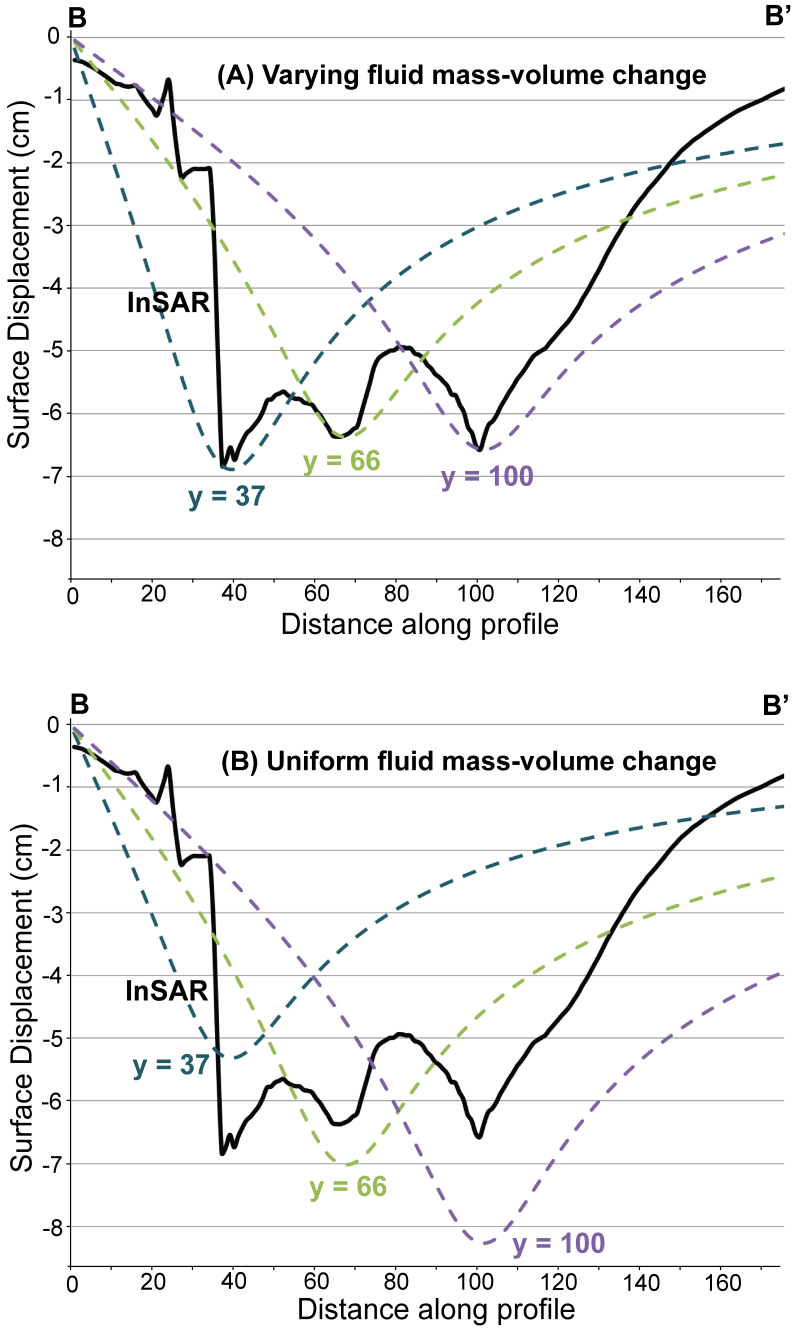


Figure 4.5 Surface displacements in response to various fluid mass volume change values at three locations: y = 37 (blue), y = 66 (green), and y = 100 (purple). Surface subsidence measured by InSAR, during a 7.3 years period, along profile line B-B'. The distance along profile is represented by points on that x-axis that correspond to 30 m pixel size. The surface displacement is displayed from 0 to -8.5cm. (A) Surface subsidence in response to varying fluid mass volume change values are used at each of the three locations (-41.8 kg /$m^3$ at y = 37, -29.3 kg/$m^3$ at y = 66, and -25.7 kg/$m^3$ at y = 100). (B) Surface subsidence in response to a constant fluid mass volume change value of -32.3 kg/$m^3$ at each of the three locations.

set the center of dilatation (y) to 37, where InSAR subsidence is greatest along the E-W profile (6.8 cm), I found that a fluid mass volume change of -41.8 kg /$m^3$ is necessary to fit the surface displacement results at that location. The second peak in surface subsidence occurs at y = 66, where a fluid mass volume change of -29.3 kg/$m^3$ is required to achieve ~6.4 cm of subsidence. Lastly, the third peak in subsidence occurs at y = 100, where a mass volume change of -25.7 kg/$m^3$ is necessary to achieve the ~6.6 cm of subsidence measured by InSAR. When the average fluid mass volume change of -32.3 kg/$m^3$ is applied to the three test locations, I found no reasonable match for any of the locations (Figure 4.3).

## 4.5 Discussion

Using InSAR I estimate the surface displacement over the Dawanqi oil field in the Kuqa fold-thrust belt. While several works have documented surface subsidence in response to hydrocarbon extraction (e.g., Fielding et al., 1998; Saif et al., 2006), few have observed subsidence juxtaposed with uplift as I have (e.g., Teatini et al., 2011). Although the Dawanqi oil field is situated over a salt-cored anticline, the observed deformation is not considered a result of salt motion because the thickness of the suprasalt section (2-5 km) is much greater than the depth of drilling (200-600 m) to accommodate such confined, localized surface displacement patterns. I considered the impact of hydrocarbon extraction as a cause of surface displacement in the area as well as local fault strain accumulation. The fault displacement model results illustrate that a 3 km deep north-dipping reverse fault or south-dipping normal fault can generate a displacement pattern similar to our InSAR observations. However, no single model can accommodate the magnitude of both uplift and subsidence.

The displacements detected at Dawanqi oil field are interpreted to be the result of rapid compaction due to hydrocarbon extraction. The three areas of concentrated subsidence correspond to locations of apparent hydrocarbon production (observed via Google Earth). The models reveal that the fluid mass volume change must laterally range from -25.7 to -41.8 $kg/m^3$ to accommodate the observed surface displacements. Although the accuracy of these models are limited by the lack of production information, this type of analysis is important to perform as it sheds light on the range of volume changes that lead to notable surface displacements. Monitoring surface displacement and modeling how it relates to fluid production must become a routine part of the production process foremost because of the potential safety hazard. Furthermore, reservoir compaction and the loss of reservoir volume can significantly hinder hydrocarbon production efficiency.

Reservoir volume loss due to fluid extraction can be offset by fluid injection. However, reservoir pore-pressure increase resulting from fluid injection used to enhance productivity can also lead to hazardous surface displacement (uplift). Confirmation of the use of fluid injection could not be verified here because such details like onset, locations, rates, durations and the type of fluid in use, if any, are considered proprietary. Evidence of fluid injection could also not be observed via satellite imagery (Google Earth). Therefore, I interpret the observed uplift at Dawanqi oil field to be related to strain accumulation along a fault.

Faults slip when the total stress (the sum of the ambient and induced stresses) overcomes the frictional resistance. Favored slip planes therefore depend on the orientation and magnitude of the ambient stress. A north-dipping reverse fault is likely to occur in this area given the regional tectonic regime. The Dawanqi oil field is centered in the Baicheng

mini basin, which is part of the Kuqa-fold-thrust belt system that is actively accommodating N-S compression between the Tarim Basin and the Tian Shan. Furthermore, our models show that a north-dipping reverse fault can generate a vertical displacement pattern similar in spatial distribution and magnitude as our InSAR observations.

Therefore I interpret the subsidence to be directly anthropogenically-induced and the surface uplift to be the result of strain accumulation across a north-dipping reverse fault. The time series shows that the rate and acceleration of subsidence mirror that of the uplift. If the uplift is not the result of fluid injection, which has not been confirmed or denied to exist here, then it is likely the case that as the subsidence started and continues, a pre-existing fault was reactivated. If the subsidence was occurring on the footwall of a local fault then it may have initiated the uplift on the hanging-wall. Because there is no evidence of earthquakes in the vicinity, I can assume that the displacements observed are aseismic and do not correspond to any recent fault ruptures. However, continued strain accumulation should inevitably trigger local seismic events.

## 4.6 Conclusions

In this study I present quantitative estimates of surface displacement over the Dawanqi oil field in the Kuqa fold-thrust belt. Surface displacements resulting from fault slip and reservoir volume loss were modeled. Hydrocarbon extraction is interpreted to be the catalyst for the localized, aseismic surface displacements observed here. The observed subsidence is interpreted to be anthropogenically-induced and the neighboring surface uplift is interpreted to be the result of strain accumulation across a north-dipping reverse fault. Monitoring surface displacement associated with hydrocarbon production is critical

because of the significant safety hazard potential of rapid surface deformation. Economically, monitoring surface displacement at producing fields can potentially prevent or subdue the irreversible reservoir volume loss that can impede hydrocarbon production.

# CHAPTER 5
# SUMMARY AND CONCLUSIONS

This dissertation consists of three principal projects (Chapters 3, 4, and 5) that study active tectonics and have the common goal of gaining a deeper understanding a variety of neotectonic kinematics at varying spatial scales. The large scale Tian Shan project aimed to characterize the vertical component of deformation in this region that had not been previously done (Chapter 3). The subaerial salt project analyzed a unique type of intracontinental deformation and kinematically characterized recently recognized salt bodies in the region (Chapter 4). The Dawanqi oil-field project analyzed an increasingly common form of neotectonic deformation, anthropogenic deformation (Chapter 5). The following sections include a summarization of the main conclusions of each project.

## 5.1 Current intracontinental deformation distribution

This work represents the first InSAR analysis to characterize the kinematic distribution of vertical displacements across from the Tian Shan range to the Dzungarian Alatau range. The results are interpreted through the lens of neotectonic, intracontinental studies of the Tibetan Plateau. I interpret the Tian Shan to accommodate little to none of the shortening originating from the ongoing Indo-Asia collision. The widespread area over which the Kuqa fold-thrust belt absorbs compression suggests a distributed form of deformation is predominant in the area. Similarly, the widespread area of surface displacements north of the large strike slip fault, bounding Dzungarian Alatau, to the north suggests that the diffuse deformation model more adequately describes the deformation pattern here. The lack of coherence between the Tian Shan and the Borohoro Range limit more thorough interpretations as to the overall dominant deformation style. Improved

temporal coverage and continued advances in InSAR processing promise it is only a matter of time before these details become clearer.

### 5.2 Active surface salt deformation not climate controlled

In this study, the quantitative estimates of sub-aerial salt displacement rates of surface salt bodies in Kuqa fold-thrust belt of northwest China are presented. Our work compliments the field study (Li et al, 2014) that details the geometric properties of namakiers in western Kuqa fold-thrust belt with active surface kinematic measurements of Bozidun, Daxiagu, Awate, and Quele namakiers. I measured the dominant vertical displacement and identify asymmetric deformation patterns of uplift and subsidence at Daxiagu and Awate, likely controlled by local tectonics and topography. At Quele namakier I identified areas of concentrated subsidence that are more responsive to structural barriers than climatic conditions. Contradicting expectations, I discovered that subaerial salt motion is decoupled from climatic conditions across Kuqa fold-thrust belt.

### 5.3 Direct and indirect anthropogenic deformation

In this study I present quantitative estimates of surface displacement over the Dawanqi oil field in the Kuqa fold-thrust belt. Surface displacements resulting from fault slip and reservoir volume loss were modeled. Hydrocarbon extraction is interpreted to be the catalyst for the localized, aseismic surface displacements observed here. The observed subsidence is interpreted to be anthropogenically-induced and the neighboring surface uplift is interpreted to be the result of strain accumulation across a north-dipping reverse fault. Monitoring surface displacement associated with hydrocarbon production is critical because of the significant safety hazard potential of rapid surface deformation. From an

economic, monitoring surface displacement at producing fields can potentially prevent or subdue the irreversible reservoir volume loss that can impede hydrocarbon production.

## REFERENCES


Aftabi, P., Roustaie, M., Alsop, G. I., and Talbot, C. J., 2010, InSAR mapping and modelling of an active Iranian salt extrusion: Journal of Geological Society – London, v. 167. P. 155-170.

Aki, K., and Richards, P. G., 1980, Quantitative seismology, Freemann and Co. New York.

Allen, M. B., Windley, B. F., Chi, Z., Zhong-Yan, Z., and Guang-Rei, W., 1991, Basin evolution within and adjacent to the Tien Shan Range, NW China: Journal of the Geological Society, v. 148(2), 369-378.

Allen, M.B., Windley, B.F. and Zhang, C., 1994. Cenozoic tectonics in the Urumgi-Korla region of the Chinese Tien Shan. Geologische Rundschau, v. 83(2), p. 406-416.

Avouac, J. P., Tapponnier, P., Bai, M., You, H., and Wang, G., 1993, Active thrusting and folding along the northern Tien Shan and Late Cenozoic rotation of the Tarim relative to Dzungaria and Kazakhstan, Journal of Geophysial Research, v. 98(B4), p. 6755–6804.

Baikpour, S., Zulauf, G., Dehghani, M., and Bahroudi, A., 2010, InSAR maps and time series observations of surface displacements of rock salt extruded near Garmsar, northern Iran: Journal of the Geological Society, London, v. 167, p. 171-181.

Barnhart, W.D., and Lohman, R.B., 2012, Regional trends in active diapirism revealed by mountain range-scale InSAR time series: Geophysical Research Letters, v.39, p. 1-5.

Beauducel F., 1997, OKADA85: Institut de Physique du Globe de Paris. Updated: 2014-05-24.

Berardino, P., Fornaro, G. and Lanari, R., 2002, A new algorithm for surface deformation monitoring based on small baseline differential SAR interferograms: IEEE Transactions on Geoscience and Remote Sensing, v. 40(11), p. 2375-2383.

Bürgmann, R., Rosen, P.A., and Fielding, E. J., 2000, Synthetic aperture radar interferometry to measure Earth's surface topography and its deformation: Annual Review of Earth and Planetary Sciences v. 28.1 p. 169-209.

Callot, J.-P., Trocme, V., Letouzey, J., Albouy, E., Jahani, S., and Sherkati, S., 2012, Pre-existing salt structures and the folding of the Zagros Mountains: Journal of the Geological Society, London, Special Publications, v. 363, p. 545-561.

Canerot, J., Hudec, M. R., and Rockenbauch, K., 2005, Mesozoic diapirism in the Pyrenean orogen: Salt tectonics on a transform plate boundary: AAPG Bulletin, v. 89(2), p. 211-229.

Chen, S., Tang, L., Jin, Z., Jia, C., and Pi, X., 2004, Thrust and fold tectonics and the role of evaporites in deformation in the Western Kuqa Foreland of Tarim Basin, Northwest China: Marine and Petroleum Geology, v. 21, p. 1027–1042.

Daëron, M., Avouac, J.-P., and J. Charreau, J., 2007, Modeling the shortening history of a fault tip fold using structural and geomorphic records of deformation: Journal of Geophysical Research, v. 112.

Desbois, G., Závada, P., Schléder, Z., and Urai, J. L., 2010, Deformation and recrystallization mechanisms in actively extruding salt fountain: Microstructural evidence for a switch in deformation mechanisms with increased availability of meteoric water and decreased grain size (Qum Kuh, central Iran): Journal of Structural Geology, v. 32.

Doin, M. P., Lasserre, C., Peltzer, G., Cavalié, O., and Doubre, C., 2009, Corrections of stratified tropospheric delays in SAR interferometry: Validation with global atmospheric models. Journal of Applied Geophysics, 69(1), 35-50.

Doin, M-P, Lodge, F., Guillaso, S., Jolivet, R., Lasserre, C., Ducret, G., Grandin, R., Pathier, E., and Pinel, V., 2011, Presentation of the small baseline NSBAS processing chain on a case example: the Etna deformation monitoring from 2003 to 2010 using Envisat Data Proceedings from Fringe 2011 Workshop, Frascati, Italy, 19-23 September 2011(ESA SP-697, January 2012).

Ducret, G., Doin, M. P., Grandin, R., Lasserre, C., and Guillaso, S., 2014, DEM corrections before unwrapping in a small baseline strategy for InSAR time series analysis. Geoscience and Remote Sensing Letters, IEEE, 11(3), 696-700.

England, P. and Houseman, G., 1986. Finite strain calculations of continental deformation: 2. Comparison with the India‐Asia collision zone: Journal of Geophysical Research - Solid Earth, v.91(B3), p.3664-3676.

ESA Earth Online, 2000-2016, Envisat - Operations: https://earth.esa.int/web/guest/missions/esa-operational-eo-missions/envisat. Accessed: 01/2016.

Ferretti, A., Monti-Guarnieri, A., Prati, C., Rocca, F., 2007, InSAR Prinicples: Guidelines for SAR Interferometry Processing and Interpretation. Ed. Karen Fletcher, ESA Publications, Noordwikj, Netherlands.

Fielding, E., 2012, ROI_Pac Internals - Under the Hood: InSAR Short Course UNAVCO, Boulder, CO.

Fielding, E.J., Blom, R.G., Goldstein, R.M., 1998, Rapid subsidence over oil fields measured by SAR interferometry: Geophysical Research Letters, v. 25(17), p.

3215-3218.

Galloway, D.L., Hudnut, K.W., Ingebritsen, S. E., Phillips, S. P., Peltzer, G., Roges, F., and Rosen, P.A., 1998, Detection of aquifer system compaction and land subsidence using interferometric synthetic aperture radar, Antelope Valley, Mojave Desert, California: Water Resources Research, v. 34 (10), p. 2573-2585.

Gambolati, G., Teatini, P., Ferronato, M., 2005, Anthropogenic land subsidence. In Anderson, M.G. (Ed.), The Encyclopedia of Hydrological Sciences. John Wiley and Sons, London, p. 2443-2460.

Grandin, R., Doin, M. P., Bollinger, L., Pinel-Puysségur, B., Ducret, G., Jolivet, R., and Sapkota, S. N., 2012, Long-term growth of the Himalaya inferred from interseismic InSAR measurement. Geology, 40(12), 1059-1062.

Guillaso, S., Doin, M-P, Lasserre, C., Cavalié, O., Jianbao, S., and Peltzer, G., 2011, InSAR measurement of interseismic strain in areas of low coherence: Example across the Haiyuan fault (Gansu, China) using a local InSAR adaptive range filter: Poster

Hendrix M. S., Graham, S. A., Carroll A. R., Sobel, E.R., McKnight, C. L., Schulein, B. J., and Wang, Z., 1992, Sedimentary record and climatic implications of recurrent deformation in the Tian Shan: Evidence from Mesozoic strata of the north Tarim, south Junggar, and Turpan basins, northwest China: Geological Society of America Bulletin, v. 104 (1), p. 53-79.

Hooper, A., Zebker, H., Segall, P. and Kampes, B., 2004. A new method for measuring deformation on volcanoes and other natural terrains using InSAR persistent scatterers: Geophysical research letters, v. 31(23).

Hudec, M. R., and Jackson, M. P. A., 2006, Advance of allochthonous salt sheets in passive margins and orogens: American Association of Petroleum Geologists Bulletin, v. 90(10) p. 1535–1564

Hudec M. R., and Jackson, M. P.A., 2007, Terra infirma: Understading salt tectonics: Earth-Science Reviews, v. 82, p. 1-28.

Huffman, G., 2011, Global Change Master Directory - Daily TRMM and Others Rainfall Estimate:http://gcmd.gsfc.nasa.gov/KeywordSearch/Metadata.do?Portal=GCMD&MetadataType=0&MetadataView=Full&KeywordPath=&EntryId=GES_DISC_TRMM_3B42_daily_V7, Accessed: 07/2015.

Jackson, M.P.A., 1985. Natural Strain in Diapiric and Glacial Rocksalt, with Emphasis on Oakwood Dome, East Texas. Bureau of Economic Geology, The University of Texas at Austin, Texas.

Jackson, M. P. A., and Talbot, C. J., 1986, External shapes, strain rates, and dynamics of salt structures: Geological Society of America Bulletin, v. 97, p. 305-323.

Ji, L., Zhang, Y., Wang, Q., Xin, Y. and Li, J., 2016. Detecting land uplift associated with enhanced oil recovery using InSAR in the Karamay oil field, Xinjiang, China: International Journal of Remote Sensing, v. 37(7), p.1527-1540.

Jia, D., Lu, H., Cai, D., Wu, S., Shi,Y., and Chen, C., 1998, Structural Features of Northern Tarim Basin: Implications for Regional Tectonics and Petroleum Traps: AAPG Bulletin, v. 82 (1), p. 147-159.

Jolivet, M., Dominguez, S., Charreau, J., Chen, Y., Li, Y., and Wang, Qingchen, 2010, Mesozoic and Cenozoic Tectonic History of the Central Chinese Tian Shan: Reactivated Tectonic Structures and Active Deformation: Tectonics, v. 29(6). p. 1–30.

Jolivet, R., Grandin, R., Lasserre, C., Doin,M.-P., and Peltzer,G., 2011, Systematic InSAR tropospheric phase delay corrections from global meteorological reanalysis data: Geophysical Research Letters, v. 38.

Jolivet, R., Lasserre, C., Doin, M. P., Peltzer, G., Avouac, J. P., Sun, J., and Dailu, R., 2013, Spatio-temporal evolution of aseismic slip along the Haiyuan fault, China: Implications for fault frictional properties. Earth and Planetary Science Letters, 377, 23-33.

Kehle, R.O., 1988, The origin of salt structures. In: Schreiber, B.C. (Ed.), Evaporites and Hydrocarbons. Columbia University Press, New York, pp. 345–404.

Kent, P. E., 1979, The emergent Hormuz salt plugs of southern Iran: Journal of Petroleum Geology, v.2: p.117–144.

Kong, Y., and Pang, Z., 2012, Evaluating the sensitivity of glacier rivers to climate change based on hydrograph separation of discharge: Journal of Hydrology, in press.

Kurlansky, M., 2011, *Salt*. Random House Publisher.

Lamb, Robert, April 2010. "When will we run out of oil, and what happens then?" HowStuffWorks.com.<http://science.howstuffworks.com/environmental/energy/run-out-of-oil.htm> 06 January 2016.

Lanari, R., Lundgren, P., Manzo, M., and Casu, F., 2004, Satellite radar interferometry time series analysis of surface deformation for Los Angeles, California: Geophysical Research Letters, v. 31.

Li, S., Wang, X., and Suppe, J., 2012, Compressional salt tectonics and synkinematic strata of the western Kuqa basin, southern Tian Shan, China: Basin Research, v. 23, p. 1-

23.

Li, J., Webb, A. A. G., Mao, X., Eckhoff, I., Colón,C., Zhang, K., Wang, H., Li, A., He, D., 2014, Active surface salt structures of the western Kuqa fold-thrust belt, Northwestern China: Geosphere, v. 10 (6).

Massonnet, D., and Feigl, K. L., 1998 Radar interferometry and its application to changes in the Earth's surface: Reviews of Geophysics, v. 36(4), p. 441-500.

Meade, B.J., 2007. Present-day kinematics at the India-Asia collision zone: Geology, v. 35(1), p.81-84.

Merriam, M. F., Smoluchowski, R., and Wiegand, D. A., 1962, High-temperature thermal expansion of rocksalt: American Physical Society, v. 125.

Molnar, P., and Tapponnier, P., 1975, Cenozoic Tectonics of Asia: Effects of a Continental Collision: Science, v. 189(4201), p. 419–426.

Okada Y., 1985, Surface deformation due to shear and tensile faults in a half-space, Bulletin Seismological Society of America, v. 75(4), p. 1135-1154.

Peltzer, G. and Tapponnier, P., 1988. Formation and evolution of strike-slip faults, rifts, and basins during the India-Asia collision: An experimental approach: Journal of Geophysical Research - Solid Earth, v.93(B12), p.15085-15117.

Pratt, W.E., and Johnson, D.W., 1926, Local Subsidence of the Goose Creek Oil Field: Journal of Geology, v. 34(7), p. 577-590.

Rutqvist, J., Vasco, D. W., Myer, L., 2010, Coupled reservoir-geomechanical analysis of CO2 injection and ground deformations at In Salah, Algeria: International Journal of Greenhouse Gas Control, v. 4(2), p. 225-230.

Saif, D., Al-Dousari, A., Al-Ghadban, A., and Aritoshi, M., 2006, Use of interferometric techniques for detecting subsidence in the oil fields of Kuwait using Synthetic Aperture Radar Data: Journal of Petroleum Science & Engineering, v. 50, p. 1-10.

Schmidt, D. A., and Bürgmann, R., 2003, Time-dependent land uplift and subsidence in the Santa Clara valley, California, from a large interferometric synthetic aperture radar data set: Journal of Geophysical Research: Solid Earth (1978–2012).

Segall, P., 1989, Earthquakes triggered by fluid extraction: Geological Society of America, v. 17, p. 942-946.

Talbot, C. J., and Aftabi, P., 2004, Geology and models of salt extrusion at Qum Kuh, central Iran: Journal of Geological Society – London, v. 161. p. 321-334.

Talbot, C. J., and Jackson, M. P. A., 1987, Internal kinematics of salt diapirs: Bulletin of American Association of Petroleum Geologists, v. 71(9). p. 1068-1093.

Talbot, C. J., and Pohjola, V., 2009, Subaerial salt extrusions in Iran as analogues of ice sheets, streams and glaciers: Earth Science Reviews, v. 97(1-4), p. 155-183.

Talbot, C. J., and Rogers, E. A., 1980, Seasonal movements in a salt glacier in Iran. Science, v. 208(4442), p. 395-397.

Tang, L.-J., Jia, C.-Z., Jin, Z.-J., Chen, S.-P., Pi, X.-J., and Xie, H.-W., 2004, Salt tectonic evolution and hydrocarbon accumulation of Kuqa fold belt, Tarim Basin, NW China: Journal of Petroleum Science and Engineering, v. 41, p. 97-108.

Tapponnier, P. and Molnar, P., 1976. Slip-line field theory and large-scale continental tectonics: Nature, v. 264(5584), p.319-324.

Tapponnier, P., Peltzer, G., Le Dain, A.Y., Armijo, R. and Cobbold, P., 1982. Propagating extrusion tectonics in Asia: New insights from simple experiments with plasticine: Geology, v.10(12), p.611-616.

Teatini, P.,Gambolati, G., Ferronato, M., Settari, A., Walters, D., 2011, Land uplift due to subsurface fluid injection: Journal of Geodynamics, v. 51, p. 1-16.

Terzaghi, C., 1925, Principles of Soil Mechanics: Engineering News-Record, v. 95 p. 19-27.

Thatcher, W., 2007. Microplate model for the present-day deformation of Tibet: Journal of Geophysical Research: Solid Earth, v.112(B1).

Thoms, R.L. and Gehle, R.M., 2000. A brief history of salt cavern use. In The 8th World Salt Symposium: Elsevier. v. 2, p. 207-214.

Trusheim, F., 1960, Mechanism of salt migration in northern Germany: Bulletin of the American Association of Petroleum Geologists, v.A(9) p. 1519-1540.

Tutiempo Network, S.L., "Climate KUQA - Climate Data 1956 – 2015." *TuTiempo.net.* November 2015 (updated). Accessed: December 2014. URL: en.tutiempo.net/climate/ws-516440.html.

Urai, J. L., C. J. Spiers, H. J. Zwart, and G. S. Lister, 1986, Weakening of rock salt by water during long-term creep: Nature, v. 324, p. 554-557.

Walker, C. W., 1973, Nature and Origin of Caprock Overlying Gulf Coast Salt Domes: Fourth International Symposium on Salt–Northern Ohio Geological Society. p. 169-195.

Wang, X., Suppe, J., Guan, S., Hubert-Ferrari, A., Gonzalez-Mieres, R., and Jia, C., 2011, Cenozoic structure and tectonic evolution of the Kuqa fold belt, southern Tianshan, China, in K. McClay, J. H. Shaw, and J. Suppe, eds., Thrust fault-related folding: AAPG Memoir 94, p. 215-243.

Wang, Q., Zhang, P.Z., Freymueller, J.T., Bilham, R., Larson, K.M., Lai, X., You, X.Z., Niu, Z.J., Wu, J.C., Li, Y.X., Liu, J.N., Yang, Z.Q., and Chen, Q.Z., 2001, Present-day crustal deformation in China constrained by global positioning system measurements: Science, v. 294, p. 574–577.

Weijermars, R., Jackson, M.P.A., and Vendeville, B., 1993, Rheological and tectonic modeling of salt provinces: Tectonophysics, p. 143–174.

Weinberg, R. F., 1993, The upward transport of inclusions in Newtonian and power-law salt diapirs: Tectonophysics, v. 228. p. 141-150.

Weinberger, R., Lyakhovsky, V., Baer, G., and Begin, Z. B., 2006, Mechanical modeling and InSAR measurements of Mount Sedom uplift, Dead Sea basin: Implications for effective viscosity of rock salt: Geochemistry, Geophysics, Geosystems, v. 7(5).

Wenkert, D., 1979, The flow of salt glaciers: Geophysical Research Letters, v. 6(6).

Windley, B.F., Allen, M. B., Zhang, C., Zhao, Z-Y, and Wang, G-R., 1990, Paleozoic accretion and Cenozoic Redeformation of the Chinese Tien Shan Range, Central Asia: Geology, v. 18(2), p. 128–131.

Wright, T.J., Parsons, B., England, P.C. and Fielding, E.J., 2004. InSAR observations of low slip rates on the major faults of western Tibet: Science, v. 305(5681), p. 236-239.

Wu, Z., Yin, H., Wang, X., Zhao, B., and Jia, D., 2013, Characteristics and deformation mechanism of salt-related structures in the western Kuqa depression, Tarim basin: Insights from scaled sandbox modeling: Tectonophysics, v. 613-614, p. 81-96.

Yang, S., Li, J., and Wang, Q., 2008, The deformation pattern and fault rate in the Tianshan Mountains inferred from GPS observations: Science in China Series D: Earth Sciences, v. 51(8), p. 1064-1080.

Yin, A. and Taylor, M.H., 2011. Mechanics of V-shaped conjugate strike-slip faults and the corresponding continuum mode of continental deformation: Geological Society of America Bulletin, v. 123(9-10), p.1798-1821.

Zebker, H. A., Rosen, P. A., Goldstein, R. M., Gabriel, A., and Werner, C., 1994, On the derivation of coseismic displacement fields using differential radar interferometry: the Landers earthquake: Journal of Geophysical Research, v. 99(B10), p. 19,617-19,634.

Zhang, P.Z., Shen, Z., Wang, M., Gan, W.J., Burgmann, R., and Molnar, P., 2004, Continuous deformation of the Tibetan Plateau from global positioning system data: Geology, v. 32, p. 809–812.

Zhong, D., and Xia, W. S., 1998a, The investigation report of Mesozoic–Cenozoic strata, structure, sedimentary faces, and petroleum potential of Kuche foreland basin outcrop area (with 1:100,000 Kuche foreland basin geologic map): Research report of Tarim Oilfield Company, Xinjiang, p. 462.

Zubovich, A. V., Wang, X. Q., Scherba, Y. G., Schelochkov, G. G., Reilinger, R., Reigber, C., and Beisenbaev, R. T., 2010, GPS velocity field for the Tien Shan and surrounding regions: Tectonics, v. 29(6).

# APPENDIX A
# INTERFEROMETRIC SYNTHETIC APERTURE RADAR PROCESSING

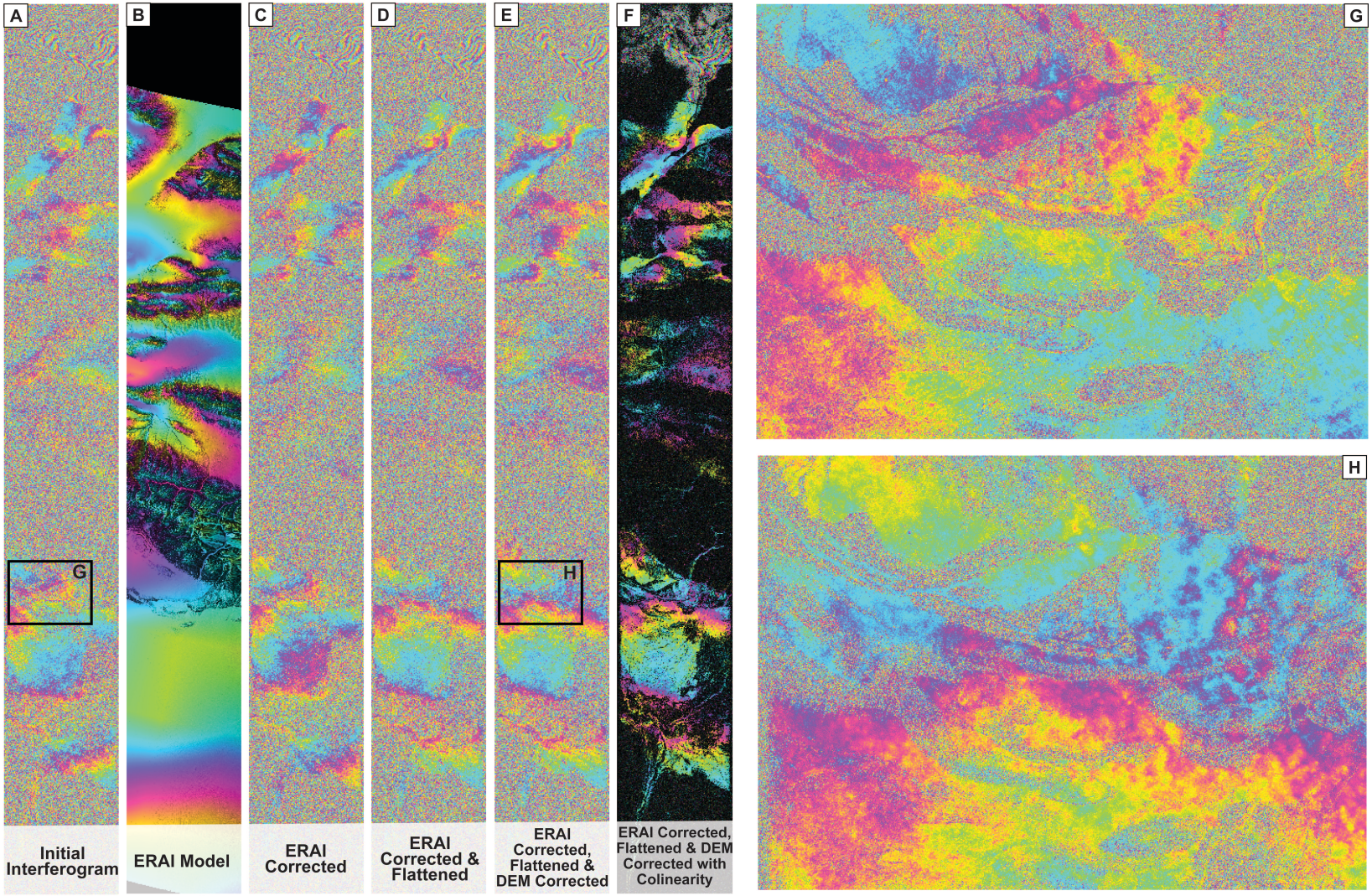

Track 291 - Specifications of each interferogram

| Date 1 | Date 2 | Bt (year) | Bp start (m) | Bp end (m) | Bp mean (m) |
|---|---|---|---|---|---|
| 20030623 | 20030901 | 0.1898 | -494.5 | -423.11 | -458.8 |
| 20030623 | 20040119 | 0.5725 | 9.54 | 213.02 | 111.28 |
| 20030623 | 20050207 | 1.623 | 166.27 | 268.93 | 217.6 |
| 20030623 | 20050523 | 1.9167 | -206.3 | -111.34 | -158.82 |
| 20030901 | 20040607 | 0.7665 | -109.61 | -146.93 | -128.27 |
| 20030901 | 20041025 | 1.149 | -87.34 | -192.76 | -140.05 |
| 20030901 | 20041129 | 1.2434 | 45.78 | 93.14 | 69.46 |
| 20030901 | 20050103 | 1.3389 | -119.23 | 19.43 | -49.9 |
| 20030901 | 20050418 | 1.6299 | 72.52 | 7.64 | 40.08 |
| 20030901 | 20050801 | 1.9167 | 110.41 | 178.48 | 144.44 |
| 20031110 | 20050207 | 1.2418 | -520.93 | -505.85 | -513.39 |
| 20031110 | 20060123 | 2.2021 | 85.31 | 127.65 | 106.48 |
| 20031110 | 20060403 | 2.3975 | -26.67 | -38.86 | -32.77 |
| 20031110 | 20060925 | 2.8743 | -44.38 | -85.02 | -64.7 |
| 20040119 | 20050207 | 1.0505 | 156.73 | 55.91 | 106.32 |
| 20040119 | 20050523 | 1.3442 | -215.84 | -324.36 | -270.1 |
| 20040119 | 20060227 | 2.1052 | -105.12 | -133.64 | -119.38 |
| 20040329 | 20040920 | 0.4753 | 277.68 | 387.13 | 332.41 |
| 20040329 | 20050905 | 1.4343 | 189.67 | 264.77 | 227.22 |
| 20040329 | 20060717 | 2.3005 | 181.45 | 100.37 | 140.91 |
| 20040607 | 20041025 | 0.3826 | 22.27 | -45.84 | -11.78 |
| 20040607 | 20041129 | 0.4769 | 155.39 | 240.07 | 197.73 |
| 20040607 | 20050103 | 0.5724 | -9.62 | 166.36 | 78.37 |
| 20040607 | 20050314 | 0.7692 | -183.67 | -28.96 | -106.31 |
| 20040607 | 20050418 | 0.8634 | 182.13 | 154.57 | 168.35 |
| 20040607 | 20050627 | 1.0547 | -193.74 | -160.19 | -176.97 |
| 20040920 | 20050314 | 0.4836 | 169.91 | 169.27 | 169.59 |
| 20040920 | 20050627 | 0.7692 | 159.83 | 38.04 | 98.94 |
| 20040920 | 20050905 | 0.959 | -88.01 | -122.36 | -105.19 |
| 20040920 | 20060717 | 1.8252 | -96.23 | -286.77 | -191.5 |
| 20041025 | 20041129 | 0.0944 | 133.12 | 285.91 | 209.52 |
| 20041025 | 20050103 | 0.1898 | -31.89 | 212.19 | 90.15 |
| 20041025 | 20050314 | 0.3866 | -205.93 | 16.88 | -94.53 |
| 20041025 | 20050418 | 0.4808 | 159.86 | 200.4 | 180.13 |
| 20041025 | 20050627 | 0.6721 | -216.01 | -114.35 | -165.18 |
| 20041025 | 20050801 | 0.7677 | 197.75 | 371.24 | 284.5 |
| 20041129 | 20050103 | 0.0955 | -165.01 | -73.71 | -119.36 |
| 20041129 | 20050418 | 0.3865 | 26.74 | -85.5 | -29.38 |
| 20041129 | 20050523 | 0.4835 | 242.41 | 218.62 | 230.52 |
| 20041129 | 20050801 | 0.6733 | 64.63 | 85.33 | 74.98 |
| 20050103 | 20050314 | 0.1968 | -174.05 | -195.32 | -184.68 |
| 20050103 | 20050418 | 0.291 | 191.75 | -11.79 | 89.98 |
| 20050103 | 20050627 | 0.4823 | -184.13 | -326.55 | -255.34 |
| 20050103 | 20050801 | 0.5779 | 229.64 | 159.04 | 194.34 |
| 20050207 | 20071224 | 2.8798 | 85.06 | 45.74 | 65.4 |
| 20050314 | 20050627 | 0.2855 | -10.08 | -131.23 | -70.65 |
| 20050314 | 20050905 | 0.4753 | -257.92 | -291.63 | -274.78 |

| | | | | | |
|---|---|---|---|---|---|
| 20050314 | 20070319 | 2.0137 | 86.8 | 49.39 | 68.09 |
| 20050418 | 20050523 | 0.097 | 215.68 | 304.12 | 259.9 |
| 20050418 | 20050801 | 0.2869 | 37.89 | 170.83 | 104.36 |
| 20050523 | 20050801 | 0.1898 | -177.79 | -133.29 | -155.54 |
| 20050523 | 20060227 | 0.761 | 110.72 | 190.72 | 150.72 |
| 20050523 | 20080512 | 2.97 | 21.6 | 25.64 | 23.62 |
| 20050627 | 20050905 | 0.1898 | -247.84 | -160.4 | -204.12 |
| 20050627 | 20070319 | 1.7281 | 96.87 | 180.62 | 138.75 |
| 20050801 | 20071119 | 2.2993 | -111.66 | -111.14 | -111.4 |
| 20050905 | 20060717 | 0.8662 | -8.22 | -164.4 | -86.31 |
| 20060123 | 20060403 | 0.1953 | -111.98 | -166.52 | -139.25 |
| 20060123 | 20060925 | 0.6721 | -129.69 | -212.67 | -171.18 |
| 20060227 | 20080512 | 2.209 | -89.12 | -165.09 | -127.1 |
| 20060227 | 20080929 | 2.5887 | 172.26 | 63 | 117.63 |
| 20060403 | 20060925 | 0.4768 | -17.72 | -46.16 | -31.94 |
| 20060717 | 20070319 | 0.6721 | 352.94 | 505.43 | 429.18 |
| 20060925 | 20071224 | 1.2473 | -391.48 | -375.09 | -383.29 |
| 20070319 | 20071119 | 0.6667 | 205.23 | 193.83 | 199.53 |
| 20070319 | 20090323 | 2.0109 | -40.96 | -47.06 | -44.01 |
| 20070319 | 20090914 | 2.4863 | -8.81 | -1.87 | -5.34 |
| 20071119 | 20080512 | 0.4808 | 311.05 | 270.06 | 290.55 |
| 20071119 | 20080825 | 0.7664 | 50.45 | 83.71 | 67.08 |
| 20071119 | 20081103 | 0.9562 | 124.87 | 138.25 | 131.56 |
| 20071224 | 20080929 | 0.7637 | -174.65 | -172.29 | -173.47 |
| 20071224 | 20091228 | 2.011 | -133.39 | -145.79 | -139.59 |
| 20071224 | 20100726 | 2.5889 | -143.58 | -131.21 | -137.4 |
| 20080512 | 20080825 | 0.2855 | -260.59 | -186.35 | -223.47 |
| 20080512 | 20080929 | 0.3798 | 261.38 | 228.09 | 244.74 |
| 20080512 | 20090216 | 0.7609 | -33.67 | -61.86 | -47.76 |
| 20080512 | 20090427 | 0.9576 | 23.76 | -9.72 | 7.02 |
| 20080825 | 20081103 | 0.1898 | 74.42 | 54.54 | 64.48 |
| 20080825 | 20090112 | 0.3811 | 103.62 | 59.81 | 81.71 |
| 20080825 | 20090323 | 0.5778 | -296.64 | -324.61 | -310.63 |
| 20080825 | 20101004 | 2.1091 | -199.75 | -192.38 | -196.07 |
| 20080929 | 20090427 | 0.5779 | -237.63 | -237.81 | -237.72 |
| 20080929 | 20091228 | 1.2473 | 41.27 | 26.5 | 33.88 |
| 20080929 | 20100726 | 1.8252 | 31.07 | 41.08 | 36.08 |
| 20081103 | 20090112 | 0.1913 | 29.2 | 5.27 | 17.23 |
| 20081103 | 20090601 | 0.5778 | 38.76 | -33.24 | 2.76 |
| 20090112 | 20090216 | 0.0942 | 123.31 | 64.69 | 94 |
| 20090112 | 20090601 | 0.3865 | 9.56 | -38.51 | -14.48 |
| 20090216 | 20090427 | 0.1968 | 57.42 | 52.13 | 54.78 |
| 20090323 | 20090427 | 0.0944 | 580.99 | 501.23 | 541.11 |
| 20090323 | 20090914 | 0.4755 | 32.16 | 45.19 | 38.67 |
| 20090323 | 20101004 | 1.5314 | 96.89 | 132.23 | 114.56 |
| 20090427 | 20100726 | 1.2473 | 268.7 | 278.89 | 273.8 |
| 20090601 | 20101004 | 1.3416 | -312.93 | -213.68 | -263.3 |
| 20090914 | 20101004 | 1.0559 | 64.73 | 87.04 | 75.89 |
| 20091228 | 20100726 | 0.5779 | -10.19 | 14.58 | 2.19 |

# APPENDIX B
# CLIMATIC CORRELATION ANALYSIS

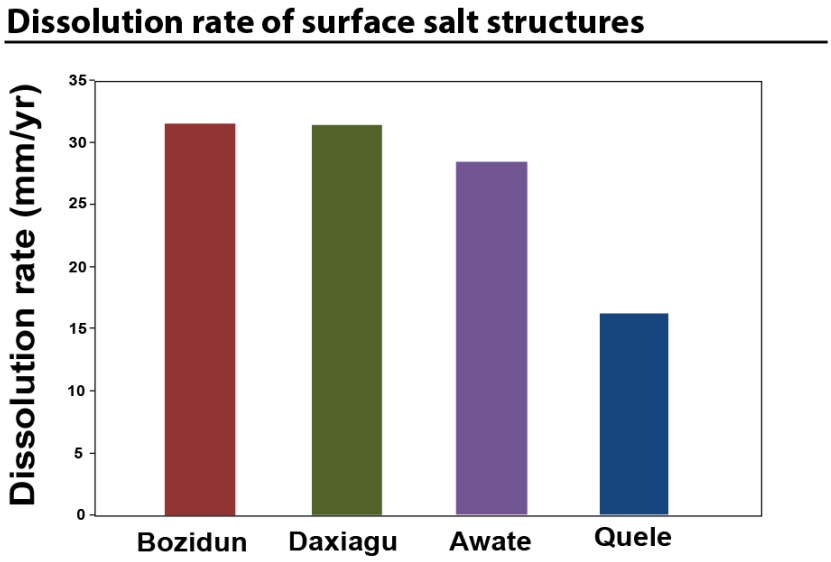


Figure B1 I also perform a first order approximation of salt dissolution rate, using local rainfall measurements and the physical properties of sodium chloride (NaCl) including a density of 2.165 g/cm$^3$, molar mass of 58.44 g/mol and water solubility of 316 g/L (5.4 mol/L) at 25°C (Seidell, 1965; Alkattan et al., 1996). I find that dissolution estimates are much greater than observed subsidence, suggesting local evaporation and in-situ salt precipitation.

| | | | | TRMM | Differential | | TRMM | Differential | | TRMM | Differential | | TRMM | Differential | | | |
|---|---|---|---|---|---|---|---|---|---|---|---|---|---|---|---|---|---|
| | | | | Rain (mm) | displ. (cm) | | Rain (mm) | displ. (cm) | | Rain (mm) | displ. (cm) | | Rain (mm) | displ. (cm) | | | |
| Inc. | Date 1 | Date 2 | Days | Bozidun | B1 | B2 | Daxiagu | D1 | D2 | Quele | Q1 | Q2 | Awate | A1 | A2 | A3 | A4 |
| 1 | 20030623 | 20030901 | 71 | 108.47 | 0.08 | -0.15 | 108.47 | -0.02 | 0.29 | 38.74 | 0.07 | 0.73 | 94.03 | 0.27 | 0.19 | 0.08 | -0.23 |
| 2 | 20030901 | 20040119 | 141 | 43.41 | -0.92 | -0.25 | 43.41 | 0.05 | -0.59 | 36.12 | -0.61 | -1.31 | 38.84 | -0.20 | 0.13 | -0.74 | -0.03 |
| 3 | 20040119 | 20040329 | 71 | 13.53 | 1.15 | 0.17 | 13.53 | 0.53 | 0.56 | 11.20 | -0.30 | 0.72 | 14.14 | -0.23 | -0.08 | 2.63 | -0.10 |
| 4 | 20040329 | 20040607 | 71 | 13.79 | -0.30 | 0.34 | 13.79 | -0.15 | -0.68 | 15.23 | 0.13 | -0.64 | 13.59 | -0.13 | 0.25 | -0.55 | -0.51 |
| 5 | 20040607 | 20040920 | 106 | 91.48 | 0.56 | -0.09 | 91.48 | 0.31 | 0.24 | 47.66 | -0.17 | 0.30 | 88.95 | 0.10 | 0.18 | -0.41 | 0.12 |
| 6 | 20040920 | 20041025 | 36 | 3.96 | -0.50 | -0.06 | 3.96 | 0.10 | -0.15 | 3.86 | -0.16 | -0.07 | 6.26 | -0.17 | -0.10 | -0.41 | -0.25 |
| 7 | 20041025 | 20041129 | 36 | 0.00 | 0.22 | 0.34 | 0.00 | -0.10 | -0.20 | 0.00 | 0.24 | -0.05 | 0.00 | 0.02 | 0.11 | -0.10 | -0.03 |
| 8 | 20041129 | 20050103 | 36 | 29.69 | 1.14 | 0.69 | 29.69 | -0.12 | 0.22 | 13.91 | 0.30 | 0.26 | 18.84 | 0.13 | -0.04 | 0.21 | 0.51 |
| 9 | 20050103 | 20050207 | 36 | 8.11 | -3.40 | -1.21 | 8.11 | 0.10 | -0.50 | 6.73 | -0.67 | -1.31 | 6.63 | -0.26 | 0.08 | -3.28 | -0.63 |
| 10 | 20050207 | 20050314 | 36 | 16.49 | 2.02 | 0.27 | 16.49 | -0.33 | -0.26 | 14.45 | 0.13 | 0.95 | 17.74 | -0.41 | -0.01 | 2.35 | -0.12 |
| 11 | 20050314 | 20050418 | 36 | 8.35 | -0.05 | 0.02 | 8.35 | 0.17 | 0.07 | 1.03 | 0.21 | 0.01 | 4.61 | 0.17 | 0.00 | 0.11 | 0.08 |
| 12 | 20050418 | 20050523 | 36 | 42.57 | -0.05 | 0.10 | 42.57 | -0.32 | -0.64 | 24.52 | 0.07 | -0.10 | 40.39 | 0.29 | 0.10 | -0.51 | -0.48 |
| 13 | 20050523 | 20050627 | 36 | 25.10 | 1.22 | 0.84 | 25.10 | 0.07 | 0.29 | 14.07 | -0.38 | 0.27 | 32.16 | -0.75 | -0.17 | 0.04 | 0.22 |
| 14 | 20050627 | 20050801 | 36 | 36.84 | -0.89 | -0.83 | 36.84 | 1.12 | 0.27 | 16.29 | 0.25 | -0.61 | 31.81 | 0.21 | 0.33 | 0.47 | 0.17 |
| 15 | 20050801 | 20050905 | 36 | 34.87 | 0.07 | -0.19 | 34.87 | 0.50 | 0.96 | 21.90 | -0.18 | 0.77 | 31.77 | 0.84 | 0.14 | 0.19 | 0.54 |
| 16 | 20050905 | 20060123 | 141 | 36.99 | -0.77 | -0.33 | 36.99 | -2.04 | -2.61 | 35.05 | 0.94 | 0.09 | 30.94 | -2.57 | -0.24 | -1.11 | -0.88 |
| 17 | 20060123 | 20060227 | 36 | 9.49 | -0.50 | 0.75 | 9.49 | 3.51 | 1.07 | 5.47 | -1.08 | -0.99 | 10.79 | 1.65 | 0.26 | -0.37 | 0.19 |
| 18 | 20060227 | 20060403 | 36 | 5.06 | 0.68 | -0.60 | 5.06 | -2.15 | 0.00 | 1.19 | -0.18 | -0.06 | 3.25 | 0.14 | 0.06 | 0.12 | -0.52 |
| 19 | 20060403 | 20060717 | 106 | 96.97 | 0.95 | 1.08 | 96.97 | 0.25 | 0.41 | 33.18 | -0.67 | 0.61 | 84.82 | 0.11 | -0.20 | -0.65 | 0.58 |
| 20 | 20060717 | 20060925 | 71 | 50.43 | -0.85 | -0.66 | 50.43 | -0.86 | -1.57 | 16.75 | -0.15 | -0.68 | 35.65 | -0.35 | 0.21 | 0.45 | 0.04 |
| 21 | 20060925 | 20070319 | 176 | 21.59 | 0.42 | -0.06 | 21.59 | 2.02 | 1.75 | 16.44 | -0.11 | 0.09 | 20.69 | 0.26 | -0.13 | 0.18 | 0.20 |
| 22 | 20070319 | 20071119 | 246 | 138.21 | -0.21 | 0.28 | 138.21 | 0.18 | -0.73 | 46.58 | -0.30 | 0.21 | 134.44 | 0.13 | 0.39 | -0.83 | 0.04 |
| 23 | 20071119 | 20071224 | 36 | 11.85 | -0.19 | -0.16 | 11.85 | -1.10 | -1.02 | 4.77 | -0.38 | -0.33 | 10.30 | -0.32 | 0.17 | -2.07 | -0.15 |
| 24 | 20071224 | 20080512 | 141 | 29.62 | -0.03 | 0.38 | 29.62 | 1.24 | 0.73 | 18.60 | 0.15 | 0.32 | 27.13 | 0.23 | 0.03 | 1.58 | 0.03 |
| 25 | 20080512 | 20080825 | 106 | 102.90 | -0.15 | -0.22 | 102.90 | 0.52 | -0.04 | 52.29 | -0.58 | 0.18 | 91.10 | 0.25 | 0.25 | -0.23 | 0.00 |
| 26 | 20080825 | 20080929 | 36 | 16.75 | -0.43 | -0.29 | 16.75 | -0.37 | -0.19 | 9.74 | 0.57 | -0.22 | 11.69 | -0.29 | 0.04 | -1.15 | -0.14 |
| 27 | 20080929 | 20081103 | 36 | 12.96 | 0.42 | 0.27 | 12.96 | 0.51 | 0.26 | 21.63 | -0.11 | -0.01 | 8.82 | -0.15 | -0.36 | 0.41 | -0.24 |
| 28 | 20081103 | 20090112 | 71 | 15.15 | -0.06 | -0.11 | 15.15 | 0.53 | 0.41 | 6.91 | 0.28 | 0.42 | 12.07 | 0.39 | 0.23 | 0.43 | 0.43 |
| 29 | 20090112 | 20090216 | 36 | 12.48 | -0.16 | 0.04 | 12.48 | -0.57 | -0.82 | 9.68 | -0.43 | -0.50 | 11.62 | -0.43 | 0.08 | -0.64 | -0.43 |
| 30 | 20090216 | 20090323 | 36 | 9.57 | 0.29 | -0.09 | 9.57 | 0.49 | 0.43 | 5.60 | -0.18 | -0.14 | 8.36 | 0.00 | -0.02 | 0.12 | 0.05 |
| 31 | 20090323 | 20090427 | 36 | 2.79 | -0.43 | 0.01 | 2.79 | -0.04 | -0.13 | 5.10 | -0.27 | -0.34 | 0.69 | 0.30 | 0.30 | -0.02 | 0.02 |
| 32 | 20090427 | 20090601 | 36 | 11.36 | 0.54 | 0.22 | 11.36 | 0.24 | 0.07 | 5.24 | 1.11 | 0.66 | 13.43 | -0.17 | -0.48 | -0.24 | 0.11 |
| 33 | 20090601 | 20090914 | 106 | 73.16 | -0.33 | 0.07 | 73.16 | -0.07 | -0.14 | 35.42 | -0.09 | -0.10 | 64.88 | 0.01 | 0.22 | -0.04 | - |
| 34 | 20090914 | 20091228 | 106 | 26.12 | - | -0.09 | 26.12 | -1.38 | -1.16 | 18.84 | -0.20 | -0.65 | 28.38 | 0.05 | 0.35 | 0.29 | - |
| 35 | 20091228 | 20100726 | 211 | 177.07 | - | 0.46 | 177.07 | 0.26 | -0.47 | 75.99 | -1.21 | 0.10 | 161.10 | -0.60 | 0.31 | -0.61 | -0.16 |
| 36 | 20100726 | 20101004 | 71 | 61.31 | 0.26 | -0.72 | 61.31 | 1.87 | 0.69 | 35.17 | 0.12 | 0.42 | 59.75 | 0.58 | -0.12 | 0.05 | 0.27 |

Figure B2 Table summarizing the total TRMM daily rainfall measurements and the estimated incremental displacements from the various points across Daxiagu, Bozidun, Awate, and Quele namakiers.

Figure B3 The residuals of a dataset are the observed values minus the predicted (or average) values. Residuals highlight the data points' deviation from the linear average, which may be used to test the correlation between rainfall and surface salt displacement response. Residuals of the time series displacement (left axis) values are plotted for various points across Bozidun, Daxiagu, Awate, and Quele namakiers. The TRMM daily rainfall estimates are plotted (right axis) for comparison. When I calculate the residuals of the time series displacements at the four Kuqa fold-thrust belt namakiers and compare to TRMM rainfall I find no correlation greater than 0.1.

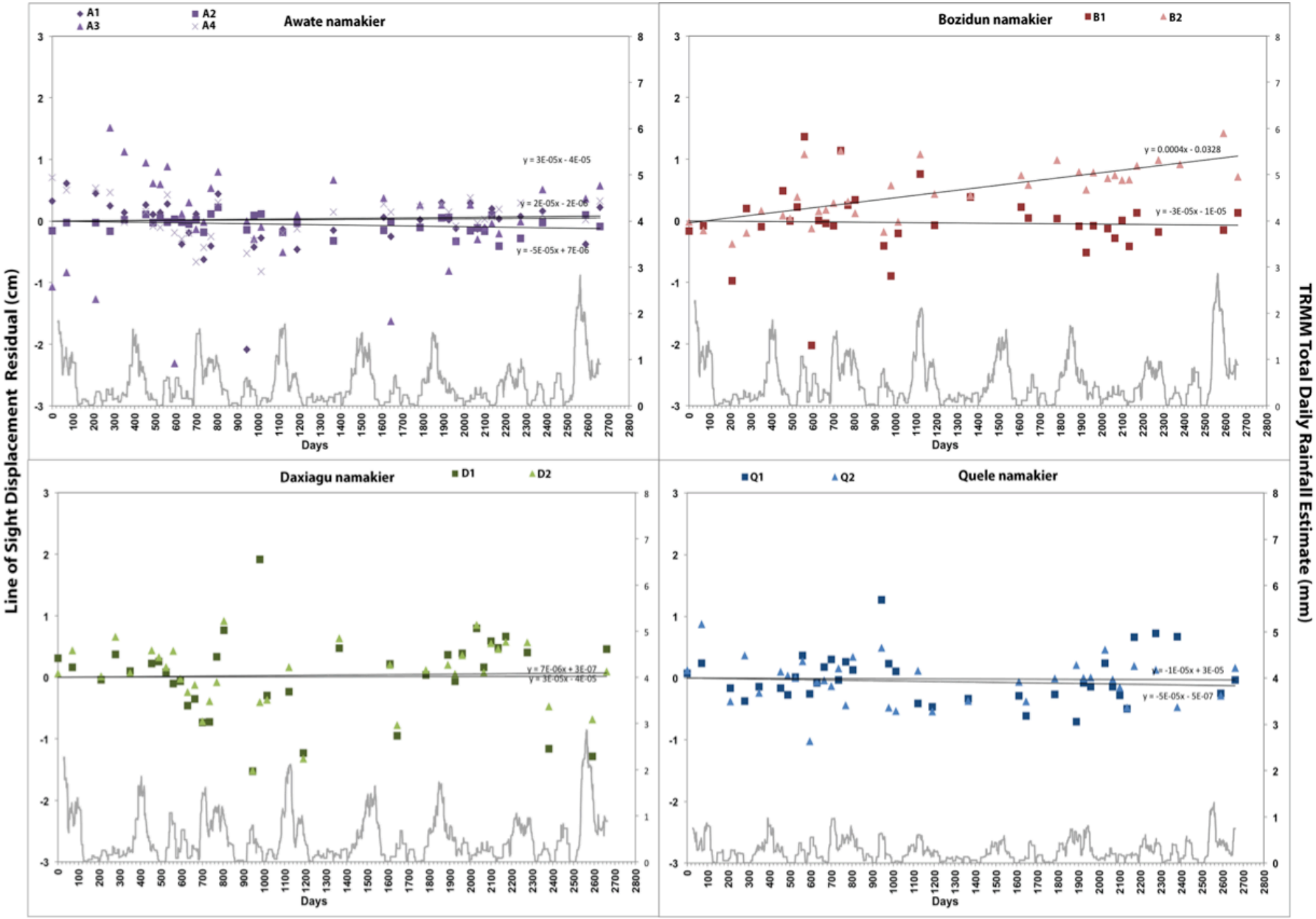
Awate namakier
A1
A2
A3
A4
y = 3E-05x - 4E-05
y = 2E-05x - 2E-06
y = -5E-05x + 7E-06
Bozidun namakier
B1
B2
y = 0.0004x - 0.0328
y = -3E-05x - 1E-05
Daxiagu namakier
D1
D2
y = 7E-06x + 3E-07
y = 3E-05x - 4E-05
Quele namakier
Q1
Q2
y = -1E-05x + 3E-05
y = -5E-05x - 5E-07
Days
Line of Sight Displacement Residual (cm)
TRMM Total Daily Rainfall Estimate (mm)

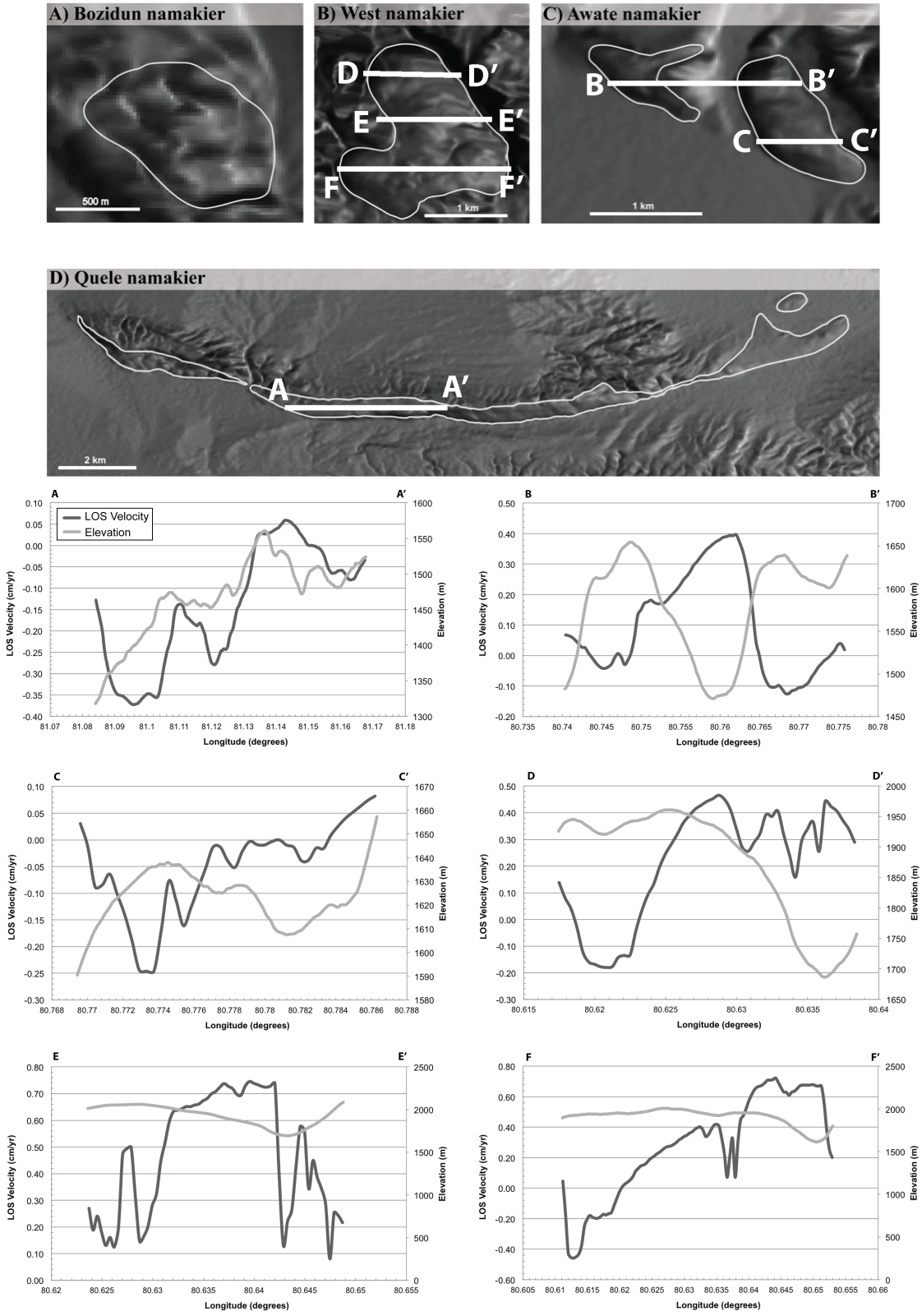


Figure B4 Profiles of InSAR displacements and topography are compared to verify the effect of topography was adequately removed from the displacement signal.

# VITA

Cindy M. Colón was born in 1989 in Elizabeth, New Jersey where she grew up and went to school until 2005. In 2007, Cindy graduated from Freehold Township High School. Cindy enrolled at Rutgers University – Newark Campus in 2007 with the intention of completing a double major in Finance and Accounting. That soon changed after she took her first geology class with Dr. Alexander Gates. Soon after Dr. Gates became an invaluable mentor to Cindy and advised her on academic and career opportunities in geosciences. Cindy graduated Summa Cum Laude from the Rutgers University Honors College in 2011. After realizing that environmental consulting firms dominated her job prospects, Cindy decided to continue onto graduate school in hopes of landing an oil and gas job. She applied to graduate schools along the "oil patch" with the intention of completing a Master's Degree but after being accepted into the GeoDE Ph.D. program at Louisiana State University she was very happy to stay in school a bit longer. She enrolled at Louisiana State University in the fall of 2011. During her Ph.D. study Cindy had three oil/gas internships (one with ExxonMobil and two with BHP Billiton) and discovered she really enjoys industry work. After completion of her Ph.D. program, she will begin work at the Anadarko Oil Corporation in The Woodlands, Texas.